Automatic reduction of large x-ray fluorescence data-sets applied to XAS and mapping experiments

UNIVERSITÄT PADERBORN
Die Universität der Informationsgesellschaft

Ligia Andrea Martín Montoya
Fakultät für Naturwissenschaften
Universität Paderborn

A thesis submitted for the degree of
Doktor der Naturwissenschaften
2016 September

---

1. Reviewer: Prof. Dr. Jörg Lindner

2. Reviewer: Prof. Dr. Gerald Henkel

3. Reviewer: Prof. Dr. Matthias Bauer

Abstract

In this thesis two automatic methods for the reduction of large fluorescence data sets are presented.

The first method is proposed in the framework of BioXAS experiments. The challenge of this experiment is to deal with samples in ultra dilute concentrations where the signal-to-background ratio is low. The experiment is performed in fluorescence mode x-ray absorption spectroscopy with a 100 pixel high-purity Ge detector. The first step consists on reducing 100 fluorescence spectra into one. In this step, outliers are identified by means of the shot noise. Furthermore, a fitting routine which model includes Gaussian functions for the fluorescence lines and exponentially modified Gaussian (EMG) functions for the scattering lines (with long tails at lower energies) is proposed to extract the line of interest from the fluorescence spectrum. Additionally, the fitting model has an EMG function for each scattering line (elastic and inelastic) at incident energies where they start to be discerned. At these energies, the data reduction is done per detector column to include the angular dependence of scattering.

In the second part of this thesis, an automatic method for texts separation on palimpsests is presented. Scanning x-ray fluorescence is performed on the parchment, where a spectrum per scanned point is collected. Within this method, each spectrum is treated as a vector forming a basis which is to be transformed so that the basis vectors are the spectra of each ink. Principal Component Analysis is employed as an initial guess of the seek basis. This basis is further transformed by means of an optimization routine that maximizes the contrast and minimizes the non-negative entries in the spectra. The method is tested on original and self made palimpsests.

Zusammenfassung

Diese Doktorarbeit stellt zwei automatische Methoden vor, um große Datenmengen in Röntgenfluoreszenzexperimenten zu reduzieren.

Die erste Methode wird für BioXAS-Experimente genutzt. Die Herausforderung dieser Experimente besteht darin, dass sehr niedrige Konzentrationen des zu untersuchenden Elements vorliegen, wodurch das Signal-zu-Untergrund Verhältnis niedrig ist. Die Röntgenabsorptionsspektroskopie-Experimente werden im Fluorezenz-Modus mit einem 100 Pixel Ge Detektor durchgeführt. Im erstem Schritt reduziert die Methode die 100 Fluoreszenz Spektren zu einem Spektrum. In diesem Schritt werden die Ausreißer anhand des Schrotrauschens identifiziert. Im nächsten Schritt wird ein Modell bestehend aus Gaussfunktionen für die Fluoreszenz-Linien und einer exponentiell modifizierten Gaussfunktion (EMG) für die Streu-Linien (mit langen Schwänzen bei in niedrigen Energien) vorgestellt. Mit diesem Modell kann die Intensität der Fluoreszenzlinie bestimmt werden, die untersucht werden soll. Außerdem beinhaltet das Modell zwei EMG für jede Streu-Linie (elastisch und inelastisch) bei höher einfallenden Energien, bei denen diese vom Detektor getrennt werden. Bei diesen Energien wird die Datenreduktion spaltenweise wegen der Winkelabhängigkeit der Streuung durchgeführt.

Die zweite automatische Methode wird für die Trennung unterschiedlicher Texte in Palimpsests eingesetzt. Dazu wird mittels Rasterfluoreszenspektroskopie ein Pergament untersucht, wobei ein Fluoreszenz-Spektrum an jedem Punkt gemessen wird. In dieser Methode wird jedes Spektrum wie ein Vektor behandelt. Deren Basis soll so transformiert werden, dass die Basis Vektoren zu den Spektren jeder Tinte werden. Hauptkomponentenanalyse wird zur Bestimmung einer ersten Vermutung genutzt. Diese Basis wird mit einer optimierenden Routine transformiert, die den Kontrast maximiert und die nicht-negativen Beträge reduziert. Die Methode wird an selbst gemachten Pergamenten getestet und an Originalen angewendet.

To my dad Alvaro, for the constant inspiration towards science.

Acknowledgements

Firstly, I would like to express my sincere gratitude to Prof. Jörg Lindner for the supervision and interest on my research. His guidance helped me in all the time of research and writing of this thesis. I would also like to thank Prof. Gerald Henkel for giving me the opportunity to work on the BioXAS project at P64, where I could develop as a scientist in a international and multidisciplinary team.

My sincere thanks to my “hands-on” supervisor Wolfgang Caliebe, his scientific and technical input on this research is innumerous. Also for the patience explaining me every detail. His passion to science and instrumentation is an inspiration to me. Furthermore, I would like to acknowledge Martin Tolkiehn for the supervision of my thesis. Specially for all the interesting discussions related with the method for text separation of palimpsests. His contributions were a key step to develop this method.

Additionally, I would like to acknowledge Wolfgang Caliebe, Martin Tolkiehn, Vadim Murzin, Maria Naumova and Leif Glaser for the contributions and help during beamtimes. Also to Uta Rütt, Jörg Strempfer and Edmund Welter for allowing us to perform experiments at the beamlines P09 and P65. Special thanks to Daniel Deckers and Leif Glaser for all the contributions regarding the historical palimpsests.

I thank my chemist colleagues Maria Naumova and Vadim Murzin for all the help to understand the chemistry behind the experiments and for the help with the samples preparation. Moreover, thanks to Vadim Murzin for the quick implementation of the reading electronics for the 100 pixel HPGe detector that made it possible to perform the experiments for my thesis.

For the proofreading of this thesis, I want to thank Prof. Lindner, Wolfgang Caliebe, Vadim Murzin, André Rothkirch and Carsten Richter. Their comments and suggestions have substantially enriched this work.

Furthermore, I thank my colleagues and friends Torsten Laurus, Martin Schroer, Sergio Vargas, Carsten Richter, Maria Naumova and Oleg Gorobtsov for the valuable discussions that clarified so many points concerning the topics of this thesis. Also, I would like to thank those friends who supported me at every moment: Luisa, Gisel, Juraj, Camilo, Andrea, Laura, Simone, Silvia, and my friends from university times in Colombia.

Special thanks to my boyfriend, Tobias, who became my second supervisor and helped me through the final process of writing my thesis, his love and support was one of the motivations to pursue this goal.

Last but not the least, I would like to thank my family: my parents and sister for supporting me emotionally at every stage of my PhD work and in this adventure abroad. Thank you for being always spiritually besides me, your love has pushed me forwards during all my life.

Finalmente, quiero agradecer a mi familia: mis padres y hermana por su apoyo emocional en cada etapa de mi doctorado y en esta aventura en el exterior. Gracias papitos y hermanita por siempre estar espiritualmente conmigo, su amor me ha empujado hacia adelante durante toda la vida.

Contents

List of Figures

List of Tables

Abbreviations

100PixHPGe 100 Pixel High-Purity Germanium detector. 2, 3, 34–36, 39, 41, 43, 44, 46, 58, 60, 61, 90, 95–97

ADC Analog-to-Digital Converter. 37

BioXAS Biological X-ray Absorption Spectroscopy. 2, 3, 23, 31, 34, 35, 58, 95, 96

EMG Exponentially Modified Gaussian Function. 55, 56, 61, 95, 96

EXAFS Extended X-ray Absorption Fine Structure. 17, 18, 49

FitSpec Fitted Spectrum. 54, 57–60

FWHM Full Width Half Maximum. 38, 54

HPGe High-Purity Germanium Detector. 48

IUPAC International Union of Pure and Applied Chemistry. 9, 21, 22

L-M Levenberg-Marquardt. 72, 78, 80, 84, 89, 93

MA Moving Average Unit. 37

MAW Moving Average Window. 37, 38, 48

NEXAFS Near Edge X-ray Absorption Fine Structure. 17, 18, 49

NNMF Non Negative Matrix Factorization. 80, 102, 103

PCA Principal Component Analysis. 62, 69–72, 77, 78, 80, 96, 97

PIPS Passivated Implanted Planar Silicon detector. 32, 33

ROI Region of Interest. 54, 56, 57, 59, 96

ROISpec Region of Interest Spectrum. 56–60

SR Synchrotron Radiation. 1, 3, 23, 26, 27, 31, 32, 42

SVD Singular Value Decomposition. 70, 76, 77, 97

system$_1$ $[\mathrm{Cu}_2(\mathrm{NGuaSSGuaN})_2](\mathrm{OTf})_2$. 51–54, 56, 57

XANES X-ray Absorption Near Edge Structure. 17, 18, 49, 57–60, 95, 96

XAS X-ray Absorption Spectroscopy. 1–3, 17, 18, 23, 27, 29, 31–35, 49, 54–56, 58, 59, 62, 95, 96

XRF X-ray Fluorescence. 3, 18, 65, 66, 73, 75, 80, 90, 97

1

Introduction

The discovery of x-rays by the German Physicist Wilhelm Röntgen in 1895 marked the beginning of X-ray Absorption Spectroscopy (XAS) [Rön72, Far95]. While making experiments with electrodes in evacuated tubes he could observe fluorescence on a screen placed near the tube [ANM01]. He was mostly impressed when he saw the bones of a hand placed between the tube and the screen, what we call nowadays "radiography". What Röntgen had observed was the phenomenon of x-ray absorption and subsequent x-ray emission (or fluorescence). The x-ray tube that Röntgen used originally was replaced first by "the Coolidge x-ray tube" [Coo13] and then by "the rotating anode x-ray tube" [Pow38]. The conventional spectrum of an x-ray tube includes a continuous contribution of the *Bremsstrahlung* (due to the deceleration of electrons) [HN04] and intense characteristic fluorescence peaks that come from the excited atoms in the tube. The most intense peak is typically used to create a monochromatic beam. Later on, applications were done in medicine with radiographies [Lin95] and in materials science, where it was shown how x-rays could be diffracted by crystals and thus reveal its structural properties [Bra13].

Maurice De Broglie and Julius Hedwig were the first who measured independently the absorption edges of platinum and tungsten in 1913 [MM]. Only until 1920, Hugo Fricke could observe the oscillations in the absorption spectrum, called *fine structure*, under supervision of Manne Siegbahn, who earned the nobel prize for it [Bun10, MM]. Although absorption of photons by matter can be studied with an x-ray tube, the solid angle of the monochromatic beam that can be used is too small and many photons are lost. Moreover, the normalization is tricky because the signal is not smooth due to additional fluorescence lines that appear as contamination of the anode. The development of XAS was boosted by the emergence of Synchrotron Radiation (SR)

[AKK$^+$06] that produces several orders of magnitude more brilliance (a quantity that allows to compare the quality of x-ray beams from different sources[1][ANM01]) than x-ray tubes and allows continuous tuning of energy. Starting over half a century after Röntgen discovered the x-rays, when the radiation produced by charged particles in synchrotrons became of use for the scientific community. Since then, XAS has been widely applied in materials sciences [KP88] but it has also become an important tool to analyze the biological role of metals and other trace elements [SF08].

XAS is employed to get information about chemical and structural properties of any sample and does not require crystallinity [Bun10]. The technique is element specific; thus, the incident photon's energy should be higher than the binding energy of inner electrons of the species of atoms that one intends to study. It involves measuring the absorption probability related to the ratio of transmitted to incident intensity of x-rays as a function of energy.

Biological X-ray Absorption Spectroscopy (BioXAS) is useful to study activation of small molecules by metalloproteins [DGLH08], dynamics of biological electron transfer [RMKK$^+$05], active site mutagenesis and post-translational modifications [PFG$^+$09], trace element metabolism [WCT$^+$09], metal hyperaccumulation [MLMK$^+$09], and bacterial metal regulators [HWG$^+$03], etc. BioXAS intends to study biological samples that often contain metals in ultra dilute concentration, impeding the measurement of absorption by means of the ratio of intensities before and behind the sample (the so called *transmision mode XAS*). One solution is to alternatively measure fluorescence intensity, which is in good approximation proportional to absorption (the so called *fluorescence mode XAS*) [GHH98, AS09]. Although this method helps to improve the signal-to-noise ratio in XAS spectra, it contains contributions from all kind of fluorescence photons as well as from scattered photons. Therefore, in order to collect the fluorescence signal that exclusively corresponds to the element under study, a detector with good energy resolution is required [vBL16].

This thesis describes the development of automatic analysis procedures for large fluorescence data sets and their application to: (i) BioXAS, and (ii) mapping experiments of *palimpsests* (antique parchments with overlapping texts) [BW93]. The physical processes behind these experiments are governed by the interaction of light and matter, e.g. absorption, emission, and scattering (explained in detail in chapters 2 and 4).

---

[1] These aspects are: number of photons emitted per second, collimation of the beam, source area and spectral distribution

BioXAS is motivated in the framework of the new beamline P64 at PETRA III extension at DESY, Hamburg, where XAS for ultra diluted sample systems is possible (see chapter 3) [MMRC16]. At this beamline a new 100 Pixel High-Purity Germanium detector (100PixHPGe) is being installed, which allows to obtain 100 fluorescence spectra simultaneously, increasing statistics of a single pixel detector by a factor of 10[Cam]. Thus, the detector and its electronics collect 100 fluorescence spectra at a single incident energy which are automatically reduced to one point in the final XAS spectrum. Each data point has a size of about 400 KB resulting in approximately 400 MB of data for a complete XAS scan whereas a typical reduced XAS spectrum is only 10-20 KB big. This is why the data sets have to be automatically reduced taking into account: (i) removal of outliers and (ii) an accurate calculation of integral intensity of the peak of interest (the complete data reduction is explained in chapter 5).

On the other hand, experiments on palimpsests are motivated to visualize hidden texts by means of X-ray Fluorescence (XRF). Palimpsests are antique sheets made of animal skin that contain several superimposed texts, some of them chemically erased. The first experiments with SR on this matter were reported in 2011 when the *Archimedes palimpsest* was investigated with x-rays to visualize a hidden iron gall ink script [Ber11, BK09, ERCBK11, Kno08]. These inks, employed in antique texts, contain several trace elements at different concentrations depending on the ink [DG10]. The palimpsest is scanned using monochromatic x-rays with sufficient energy to excite the atomic species on each point of the palimpsest and fluorescence x-rays are subsequently emitted. Similar to BioXAS this radiation is collected with an energy dispersive detector to be further analyzed. The final data set contains a spectrum per scanned point. In this thesis, antique and self made palimpsests were investigated with XRF. The goal is to process this data set in order to find one image for each single text on the palimpsest. For this purpose, an automatic method that allows visualization of independent texts is presented in chapter 6.

The theoretical background for the central experiments of this thesis (BioXAS and XRF mapping experiments of palimpsests) is the absorption and emission of x-rays, presented in chapter 2. This chapter reviews the key concepts of XAS and XRF. Then, BioXAS at P64 is explained in chapters 3, 4 and 5. Chapter 3 gives a short introduction on SR and describes the setup used for BioXAS at beamline p64 where the 100PixHPGe is the key point. The characteristic emission spectrum collected with the 100PixHPGe is explained in detail in chapter 4. Finally, chapter 5 presents the proposed data reduction for BioXAS at p64 with the 100PixHPGe. On the other hand, XRF mapping experiments on palimpsests are explained in detail in chapter 6, where an automatic algorithm for text separation is also presented. Results are finally summarized in chapter 7 and an outlook of future work is given.

2

Absorption and emission of light

The processes of photoabsorption and photoemission in matter are closely related. Absorption occurs when an incident photon has sufficient energy to excite an electron to an outer shell of the atom or to the continuum [ANM01, Bun10]. In this process, the electron is initially at an energy level E_a, subsequently an incident photon interacts with the electron, transferring it to an upper energy level E_b (see figure 2.1). Conversely, emission happens when an electron is on an upper energy level E_b and there is a vacancy in a lower energy level E_a. In this case, the electron is transferred to the lower level by means of two possible processes: *stimulated* or *spontaneous* emission [Gri05]. Stimulated emission is triggered by an extra photon and releases two identical photons after the electron is transferred from an upper energy level E_b to a lower energy level E_a (see figure 2.1). Either absorption or stimulated emission require that the incident photon energy is higher than or equal to $E_b - E_a$ in order to trigger the process. The working principle of the laser is governed by stimulated emission. In this case, one photon will produce two and then four and so on, creating an amplification chain. On the other hand, spontaneous emission happens when the electron is transferred from an upper energy level E_b to a lower one E_a without an incident photon. One important question is: “ What is triggering the process?”. The answer is that spontaneous emission is in principle a special case of stimulated emission where the external perturbation is the “zero-point” radiation [Gri05].

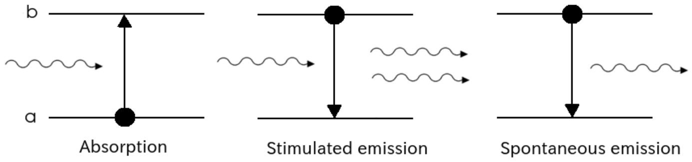

Figure 2.1: Interaction between light and atoms: absorption, stimulated emission, spontaneous emission.

Naturally, after absorption takes place, the atom is left in an excited state that leads to emission processes. There are two dominant mechanisms how the atom can return to the non-excited state, *fluorescence* and *Auger decay* [Jen99]. Fluorescence is an emission of photons with a characteristic energy after the electrons decay from an upper energy level to a lower energy level (see figure 2.2). Such a process occurs without external photons coming into the system; therefore, it is spontaneous emission. The emitted photon energy is $E_\gamma = E_b - E_a$, which is characteristic for the atom. This radiation can be emitted outside of the atom or could excite other electrons of the same atom into the continuum. Such electrons are called *Auger* electrons after one of its discoverers. The energy of the Auger electron E_{e^-} is equal to the difference between the photon energy $E_\gamma = E_b - E_a$ and the energy of the electron E_c before it was expelled from the atom (see figure 2.2) [Tho85].

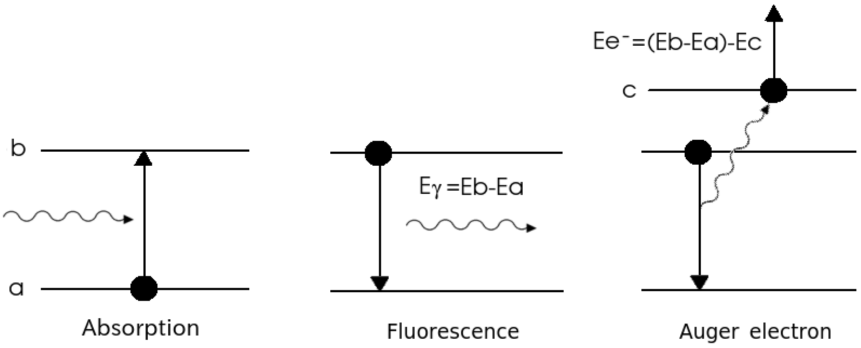

Figure 2.2: Excitation (Absorption) and deexcitation processes (Fluorescence and Auger electrons)

2.1 Electronic configuration

In order to understand processes such as absorption, fluorescence or Auger emission in detail, it is important to first review the electronic structure of atoms. Bohr postulated that every atom has discrete electron energy levels. Those levels have been calculated exactly for the hydrogen atom that serves as a model to understand the rest of the periodic table. In quantum mechanics, the state of each electron is described as a wave function that is the solution of the *Schrödinger equation*. Due to the atomic spherical symmetry, this equation is solved more conveniently in spherical coordinates. The solutions of Schrödinger equation in spherical coordinates for hydrogen indicate that each state is determined by the quantum numbers n (principal quantum number), l (angular quantum number) and m (magnetic quantum number) [Gri05]. The wave functions of the hydrogen atom can be written as:

$$\Psi_{nlm}(r,\theta,\phi) = R_{nl}(r)Y_{lm}(\theta,\phi), \tag{2.1}$$

where the angular part is defined as:

$$Y_{lm}(\theta,\phi) = \Theta_{lm}(\theta)\Phi_m(\phi), \tag{2.2}$$

with

$$\Theta_{lm}(\theta) = (-1)^m\sqrt{\frac{(2l+1)(l-m)!}{2(l+m)}}P_l^m(\cos\theta) = N_{lm}P_l^m(\cos\theta), \tag{2.3}$$

$$\Phi_m(\phi) = \frac{e^{im\phi}}{\sqrt{2\pi}}, \tag{2.4}$$

and P_l^m the associated Legendre polynomials.
The radial part is described as

$$R_{nl}(r) = \sqrt{\left(\frac{2}{na}\right)^3\frac{(n-l-1)!}{2n[(n+l)]!^3}}e^{-r/na}\left(\frac{2r}{na}\right)^l L_{n-l-1}^{2l+1}\left(\frac{2r}{na}\right) \tag{2.5}$$

where L_{n-l-1}^{2l+1} are the generalized Laguerre polynomials and a is the Bohr radius.
The allowed energies are given by:

$$E_n = -\left[\frac{m}{2\hbar^2}\left(\frac{e^2}{4\pi\epsilon_0}\right)^2\right]\frac{1}{n^2} \tag{2.6}$$

The principal quantum number describes the energy level of the atom ("shell") and takes the values:

$$n = 1,2,3\ldots. \tag{2.7}$$

The angular quantum number describes the orbital angular momentum as $L^2 = \hbar^2 l(l+1)$ ("subshell") and takes the values:

$$l = 0, 1, 2 \ldots n-1. \tag{2.8}$$

In chemistry the l values are named as s ($l = 0$), p ($l = 1$), d ($l = 2$) and f ($l = 3$).
The magnetic quantum number describes the projection along a specified axis of the orbital angular momentum as $L_z = \hbar m$ and takes the values:

$$m = -l, \ldots 1, 0, 1 \ldots, l. \tag{2.9}$$

The solutions in equation (2.1) are obtained for a potential that includes only the Coulomb interaction between the electron and the nucleus. However, this is not the whole picture. From the electron's perspective the proton is orbiting around it which sets up a magnetic field $\vec{B}$ in the electron's frame. As a consequence, the magnetic dipole moment of the spinning electron $\vec{\mu}$ tends to be aligned with $\vec{B}$. Thus, the Hamiltonian is described as [Gri05]:

$$H = -\vec{\mu} \cdot \vec{B} \tag{2.10}$$

The electron's angular momentum $\vec{L}$ and $\vec{B}$ point into the same direction. Furthermore, $\vec{\mu}$ has the same direction as the spin angular momentum of the electron $\vec{S}$. Therefore, the Hamiltonian can be written as:

$$H \propto \vec{S} \cdot \vec{L} \tag{2.11}$$

This gives rise to the *spin-orbit* interaction [Sak06]. The most important consequence of the spin-orbit interaction is that the Hamiltonian no longer commutes with the orbital angular momentum $\vec{L}$ nor with the spin angular momentum $\vec{S}$ (so they are no longer separately conserved). This is why new quantum numbers s and j are introduced, where s is the spin projection quantum number that describes the projection of the spin angular momentum as $S_z = \hbar s$ and for electrons is:

$$s = \pm 1/2, \tag{2.12}$$

and where j is the total angular momentum quantum number, represented as:

$$j = |l + s|. \tag{2.13}$$

The spin-orbit interaction leads to a degeneracy in the energy levels of equation (2.6), called *fine structure*. The energy levels of the hydrogen atom after including the spin-orbit interaction depend on the quantum numbers n and j, as:

$$E_{nj} = -\frac{13.6eV}{n^2}\left[1 + \frac{\alpha^2}{n^2}\left(\frac{n}{j+1/2} - \frac{3}{4}\right)\right] \tag{2.14}$$

where α is the fine structure constant. The energy levels depending on n and j are shown in figure 2.3.

As electrons are Fermions, the Pauli exclusion principle establishes that they can be never in the same quantum state; therefore, in any atomic configuration, each electron has to have at least one different quantum number.

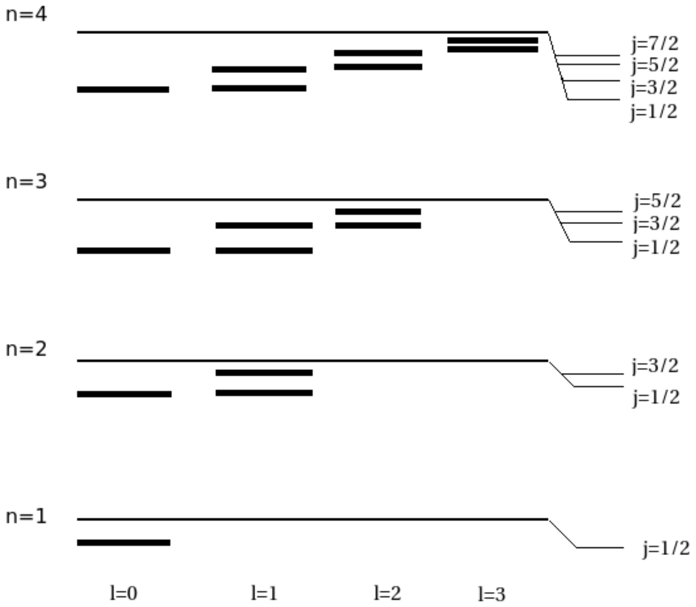

Figure 2.3: Energy levels of hydrogen, including spin-orbital interaction. Each energy level represented with the principal quantum number n is degenerated according to the total angular momentum quantum number j.

The notation in chemistry denotes the electron states ("orbitals") according to the quantum numbers n and l as: 1s, 2s, 2p, 3s, 3p and so on. On the other hand, the International Union of Pure and Applied Chemistry (IUPAC) names the energy levels including the spin-orbit interaction as "Transition Groups". This notation contains the quantum number n as K (n=1), L (n=2), M (n=3), N (n=4), O (n=5)…, and a subindex I ($j = 1/2, l = 0$), II ($j = 1/2, l = 1$), III ($j = 3/2, l = 1$), VI ($j = 3/2, l = 2$), V ($j = 5/2, l = 3$) and so on [Jen99]. Table 2.1 shows the possible electron configurations according to the quantum numbers as well as the orbital names and the transitions groups.

n	l	m	s	Orbital	J	Transition Group
1	0	0	±1/2	1s	1/2	K
2	0	0	±1/2	2s	1/2	L_I
2	1	-1,0,1	±1/2	2p	1/2, 3/2	L_{II}, L_{III}
3	0	0	±1/2	3s	1/2	M_I
3	1	-1,0,1	±1/2	3p	1/2, 3/2	M_{II}, M_{III}
3	2	-2,-1,0,1,2	±1/2	3d	3/2, 5/2	M_{IV}, M_V
4	0	0	±1/2	4s	1/2	N_I
4	1	-1,0,1	±1/2	4p	1/2, 3/2	N_{II}, N_{III}
4	2	-2,-1,0,1,2	±1/2	4d	3/2, 5/2	N_{IV}, N_V
4	3	-3,-2,-1,0,1,2,3	±1/2	4f	5/2, 7/2	N_{VI}, N_{VII}

Table 2.1: Orbitals and transition levels for each quantum number.

2.2 X-ray absorption

X-ray absorption takes place when a photon in the x-ray energy range ($\sim$ 500 eV–500 keV) interacts with a core-electron (electron in an inner shell of the atom) exciting the electron into an unoccupied state or to the continuum, leaving a core-hole (a vacancy in the energy level of the core-electron) (see figure 2.4) [New04]. The excited electron is called *photoelectron* in the frame of the photoelectric effect. A specific electron will be excited into the continuum only if the incident photon has a higher energy than the binding energy of the electron.

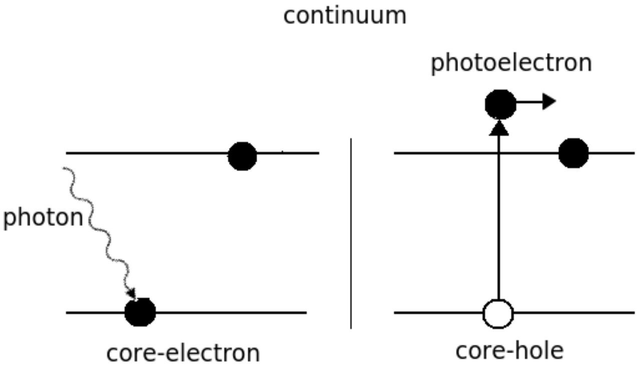

Figure 2.4: Schematic of the absorption process. On the left side the initial state is pictured, where a photon interacts with a core-electron. On the right side is the final state, where the photon has been absorbed leaving a core-hole in the atom and the photoelectron moves in the continuum.

The description of the absorption phenomenon starts with Beer's law, that relates the transmitted x-ray intensity I of a sample of thickness d with the incident intensity I_0, as:

$$I = I_0 e^{-\mu d}, \tag{2.15}$$

where μ is the so called *absorption coefficient* that is related to the absorption cross section σ_a as:

$$\mu = \left(\frac{\rho_m N_A}{M}\right) \sigma_a \tag{2.16}$$

where ρ_m is the mass density, N_A is Avogradro's number and M the molar mass [New04, ANM01, Bun10].
An empiric relation for the absorption coefficient says that:

$$\mu \propto \frac{\rho Z^4}{AE^3} \tag{2.17}$$

where E is the energy of the incident photon, Z the atomic number, A the atomic mass and ρ the sample density.

Equation (2.17) has been widely applied in medicine, specifically for radiographies. The direct dependence of μ with Z^4 provides contrast between different materials such as skin, bone, etc [New04, ANM01]. Furthermore, the inverse dependence of μ with E^3 makes the penetration depth adjustable by means of the energy.

Figure 2.5 shows the relation of the mass absorption coefficient (μ/ρ) for different materials (Pb, Cd, Fe, O) as a function of the incident x-ray energy. The plots show an overall decrease with increasing energy and the difference between different elements can be some orders of magnitude. This plot illustrates equation (2.17) but at the same time shows some not explained sudden increases of absorption or "jumps" at specific energies. These jumps are called *absorption edges* and correspond to the characteristic electron binding energies of the atom. When the energy of the incident light is higher than one of the binding energies of the atom, the incident photon can be absorbed by a core-electron and as a consequence there is a sharp rise in the absorption coefficient. Each absorption edge is described according to the transition group (see table 2.1). For example, if a photon is absorbed by a core-electron of the orbital 1s (transition group K), the absorption edge is called K1s. Figure 2.5 shows the K, L and M absorption edges of Pb. The K edge of Pb is at 88 keV, while the L_I, L_{II} and L_{III} are at the energies of 16, 15 and 13 keV respectively, and the M levels are at 3.9, 3.6, 3.1, 2.6 and 2.5 keV [TV01]. On the other hand, the K 1s and L_I 2s of O are at 0.5 and and 0.04 keV respectively; thus, they are not in the energy range of figure 2.5. The absorption edges are unique for every element in the periodic table. In this sense, x-ray absorption is an element specific technique that gives a finger print of the element under study.

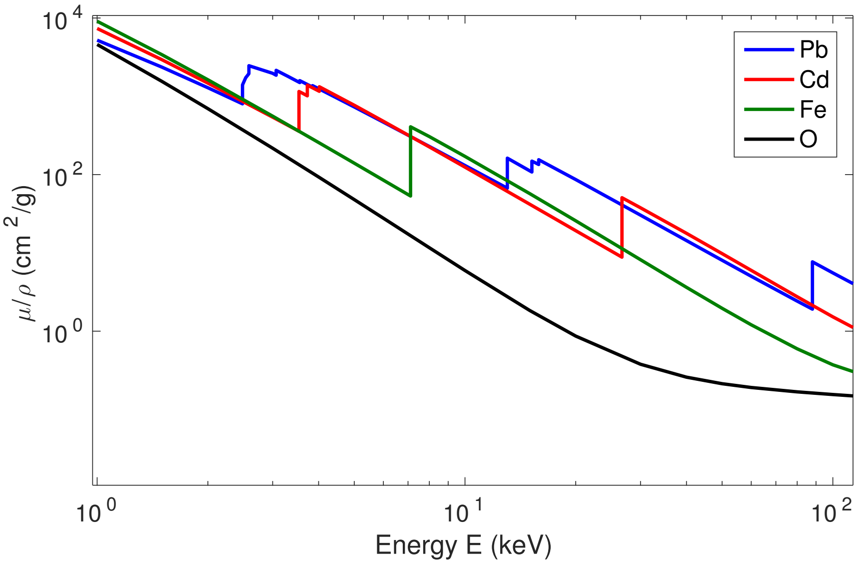

Figure 2.5: Mass absorption coefficient (μ/ρ) for the elements Pb, Cd, Fe and O in terms of the incident energy E. The values are from [NIS].

2.2.1 X-ray absorption in condensed matter

So far absorption has not been investigated upon its dependence with neighboring atoms. If the atom is embedded in matter, the interaction of the photoelectron with other atoms becomes relevant. At the smallest energies for which the photon can be absorbed, the photoelectron will be excited to unoccupied states of the atom. At higher photon energies, the photoelectron is promoted to the continuum [SR14]. The photoelectron propagates outwards, and it is scattered by neighboring atoms. The outgoing and scattered wave functions interfere, forming an oscillating pattern on the absorption coefficient [New04, ANM01, SR14, Bun10]. Figure 2.6 shows these oscillations on the K1s absorption edge of a Cu foil. These oscillations are called *fine structure*[1]. The interference of the outgoing and the scattered photoelectron waves depends on the atomic environment. Therefore, the fine structure is useful to study properties of the atoms surrounding the absorber, like coordination number, distances to neighbors and species, etc.

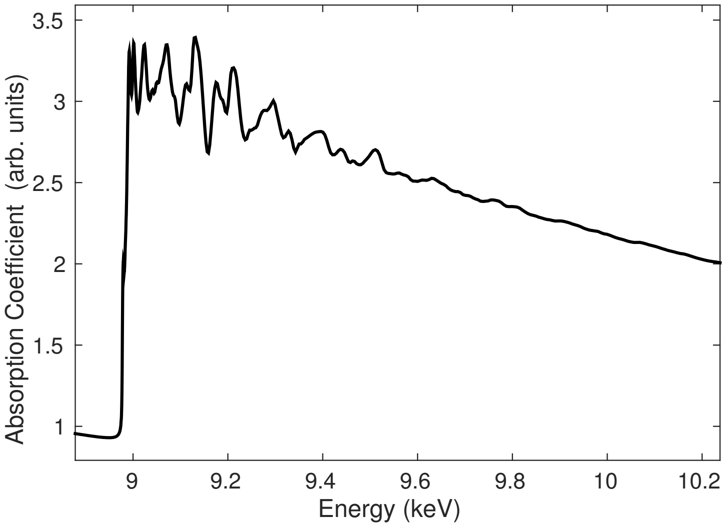

Figure 2.6: The absorption coefficient μ of Cu as a function of the incident energy E. The energy range shows the K1s absorption edge of Cu. The values are from [UWX].

From the quantum mechanical point of view, x-ray absorption is a transition between two quantum states. The initial state $|i\rangle$ has an incident x-ray photon and a core-electron and the final state $|f\rangle$ has a photoelectron and a core-hole. Therefore, the absorption coefficient μ can

---

[1] Note that fine structure here is different than the fine structure described as the degeneracy of the energy levels due to the spin-orbit interaction.

be described with *Fermi's Golden Rule* [Sak06, Gri05, New04, ANM01] as:

$$\mu \propto |\langle f| H |i\rangle|^2 \rho, \tag{2.18}$$

where H represents the interaction Hamiltonian that causes the transition (in this case the electromagnetic field of the incident x-ray photon) and ρ is the density of final states.

The initial state is highly localized because the electrons are tightly bound to the absorbing atom. Hence, it will not be affected by neighboring atoms. On the contrary, the final state includes the photoelectron that is scattered by neighboring atoms. In this sense, the final state $|f\rangle$ can be expanded as a sum of two states:

$$|f\rangle = |f_0\rangle + |\Delta f\rangle, \tag{2.19}$$

where $|f_0\rangle$ is the portion of the bare atom and $|\Delta f\rangle$ includes the effects from neighboring atoms.

Replacing equation (2.19) into (2.18), one gets:

$$\mu \propto |\langle f_0| H |i\rangle + \langle \Delta f| H |i\rangle|^2. \tag{2.20}$$

After expanding equation (2.20) (see Appendix A 8.0.1), μ is written as:

$$\mu \propto |\langle f_0| H |i\rangle|^2 \left[1 + \left(\frac{\langle \Delta f| H |i\rangle \langle f_0| H |i\rangle^*}{|\langle f_0| H |i\rangle|^2} + \text{ C.C.}\right)\right], \tag{2.21}$$

where C.C. is the complex conjugate of $\langle \Delta f| H |i\rangle \langle f_0| H |i\rangle^* / |\langle f_0| H |i\rangle|^2$.

The absorption coefficient can be then written as:

$$\boxed{\mu(E) = \mu_0(E) \left[1 + \chi(E)\right]}, \tag{2.22}$$

where

$$\mu_0(E) = |\langle f_0| H |i\rangle|^2 \tag{2.23}$$

is the absorption coefficient that depends only on the absorbing atom, as if the atom did not have any neighbor, and

$$\chi(E) = \frac{\langle \Delta f| H |i\rangle \langle f_0| H |i\rangle^*}{|\langle f_0| H |i\rangle|^2} + \text{ C.C.} \tag{2.24}$$

is the term that modulates the absorption of an isolated atom, adding effects caused by neighbors (fine structure coefficient).

2.2.2 EXAFS equation

The fine structure coefficient is in principle proportional to the matrix element of the interaction between the initial state and the neighbors:

$$\chi(E) \propto \langle \Delta f | \, H \, | i \rangle \, . \tag{2.25}$$

Evaluating the corresponding integral of the matrix element in equation (2.25) is rather simple [New04, ANM01]. The initial state is, as we have mentioned before, highly localized so it can be expressed as a Dirac delta function $\delta(\vec{r})$. The final state is the wave function of the scattered photoelectron ψ_{scatt}. The interaction hamiltonian is due to the electromagnetic field from the incoming photon, that is proportional to the electromagnetic wave $e^{i\vec{k}\cdot\vec{r}}$ [1]. Thus, the matrix element in equation (2.25) can be written as:

$$\langle \Delta f | \, H \, | i \rangle \propto \int \delta(\vec{r}) e^{i\vec{k}\cdot\vec{r}} \psi_{\text{scatt}}(\vec{r}) d\vec{r} \tag{2.26}$$

By means of the identity:

$$\int f(t)\delta(t-T)dt = f(T) \tag{2.27}$$

equation (2.26) transforms to

$$\int \delta(\vec{r}) e^{i\vec{k}\cdot\vec{r}} \psi_{\text{scatt}}(\vec{r}) d\vec{r} = e^{i\vec{k}\cdot(\vec{r}=0)} \psi_{\text{scatt}}(\vec{r}=0) = \psi_{\text{scatt}}(0) \tag{2.28}$$

thus,

$$\chi(E) \propto \psi_{\text{scatt}}(0) \tag{2.29}$$

Equation (2.29) tells us that the fine structure coefficient $\chi(E)$ is proportional to the scattered photoelectron at the position of the absorbing atom.

In order to determine $\psi_{\text{scatt}}(0)$, it is necessary to understand what happens with the outgoing photoelectron. First, the photoelectron travels a distance R as a spherical wave to the neighboring atom. Then, it is scattered back from the neighboring atom and finally, it returns to the absorbing atom, traveling a distance R as a spherical wave [New04, ANM01].

---

[1] The interaction Hamiltonian H represents the process of changing between two energy, momentum states. The interaction term needed is $\vec{p}\cdot\vec{A}$ that, for the purposes here is reduced to a term proportional to $e^{i\vec{k}\cdot\vec{r}}$.

The scattered photoelectron's wave function ψ_{scatt} is commonly expressed in terms of the photoelectron's wave number k:

$$k = \sqrt{\frac{2m_e}{\hbar^2}(E - E_i)}, \tag{2.30}$$

where E_i is the binding energy of the core-electron, E is the energy of the absorbed x-ray photon and m_e is the electron mass.

Thus, the scattered photoelectron at the absorbing atom is written as:

$$\psi_{\text{scatt}}(k, r = 0) = \underbrace{\frac{e^{ikR}}{R}}_{\text{(a)}} \underbrace{f(k)e^{\delta(k)}}_{\text{(b)}} \underbrace{\frac{e^{ikR}}{R}}_{\text{(c)}}, \tag{2.31}$$

where the term (a) describes the spherical wave of the photoelectron at the neighboring atom, at a distance R from the absorbing atom. The term (b) describes the scattering properties of the neighboring atom, with the scattering length $f(k)$[1] and the phase shift $\delta(k)$ due to the electrostatic potential between the negatively charged electron and the lattice. The term (c) describes the backscattered spherical wave.

Equation (2.31) can be written as a real function:

$$\psi_{\text{scatt}}(k, r = 0) \propto \frac{f(k)}{kR^2} \sin(2kR + \delta(k)) \tag{2.32}$$

A factor k is added in the denominator of equation (2.32) in order to have a dimensionless quantity[2].

The vibration of the neighboring atom is taken into account by multiplying equation (2.32) with the *Debye-Waller* factor $e^{-2(k\sigma)^2}$, where σ^2 is the mean-squared-displacement of the neighboring atom. Moreover, the photoelectron has a finite lifetime. There is a chance that when the photoelectron is backscattered to the absorbing atom, this is no longer in the initial state and the core-hole has been filled. To include this effect, the wave function should be a damped spherical wave, including the factor $e^{-2R/\lambda}$, where λ is the photoelectron's mean free path [New04, ANM01].

---

[1] This terms accounts for the element sensitivity of EXAFS. In general, atoms with more electrons scatter photoelectrons more strongly at higher wavenumbers[KHR08].

[2] The scattering amplitude or length has units of distance. Thus, by adding a k factor (with units m^{-1}) in the denominator a dimensionless quantity is obtained.

The function $\psi_{\text{scatt}}(k, r = 0)$ is then modified for N neighbors, vibrations and finite life time, as:

$$\psi_{\text{scatt}}(k, r = 0) \propto N\frac{f(k)}{kR^2}\sin\left(2kR + \delta(k)\right)e^{-2(k\sigma)^2}e^{-2R/\lambda}. \tag{2.33}$$

Finally summing over the different shells j, the fine structure coefficient is written as:

$$\boxed{\chi(k) \propto \sum_j \frac{N_j f(k)e^{-2(k\sigma_j)^2}e^{-2R_j/\lambda}}{kR_j^2}\sin\left(2kR_j + \delta_j(k)\right)}. \tag{2.34}$$

Equation (2.34) describes the so called Extended X-ray Absorption Fine Structure (EXAFS) and it is called the *EXAFS equation*.

2.2.3 XAS regions

The XAS spectrum has 3 main energy regions that are associated with its phenomenology (figure 2.7). The first region between ±10 eV around the edge is called X-ray Absorption Near Edge Structure (XANES). In this region, electronic transitions between inner shells and unfilled outer shells of the atom are dominant. The next region between 10-50 eV above the edge is called Near Edge X-ray Absorption Fine Structure (NEXAFS). At these energies, the photoelectron goes outside the atom and experiences multiple scattering from neighbors [Stö92]. The final region is from 50-1000 eV and is called EXAFS. In this region, the photoelectron undergoes mainly single scattering. For EXAFS, the picture of the interference between the outgoing and backscattered wave functions is valid.

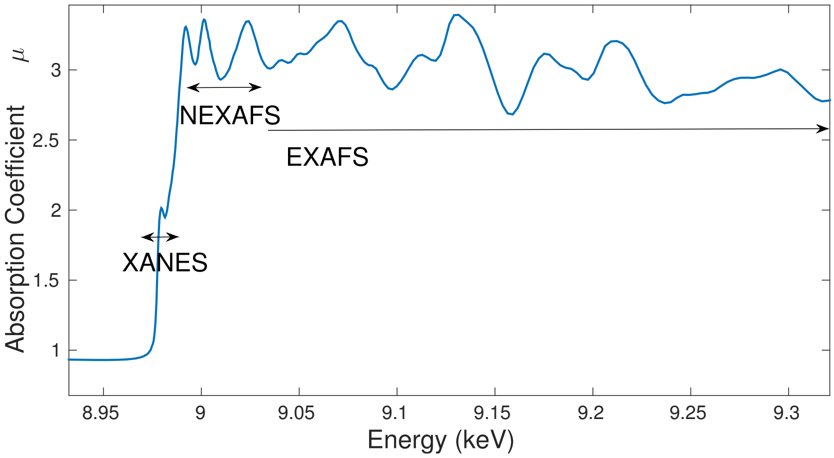

Figure 2.7: XAS regions of a Cu K1s absorption spectrum. The region between ±10 eV around the edge (XANES), between 10-50 eV above the edge (NEXAFS) and between 50-1000 eV above the edge (EXAFS).

Each of these regions provides different information. XANES is relevant to study oxidation state and coordination chemistry of the absorbing atom. NEXAFS is sensitive to the bonding environment of the absorbing atom. Moreover, from EXAFS one can extract distances, coordination number and species of neighbors.

The regions described above are established according to their physical nature. However, the XAS community uses the term XANES to refer to NEXAFS and XANES together.

2.3 X-ray fluorescence

In XRF spectroscopy a core-hole is created e.g. by x-rays, electrons, or other means[1], and the energies of the subsequently emitted photons are analyzed. This photon emission is called fluorescence, and the energies of the fluorescence photon are specific for each element. In this way, fluorescence spectroscopy is used as a fingerprint method to analyze materials. Spontaneous emission follows certain rules derived from quantum mechanics (described in chapter 2.3.1). These rules say that transitions between certain levels are more likely to occur. These transitions and their corresponding energies are tabulated for each element to enable spectroscopic

---

[1] e.g. "K capture decay" where an orbital electron reacts with a proton in the nucleus yielding a neutron that remains in the nucleus and an escaping electron neutrino. The atomic number of the daughter electron is decreased by one while the atomic mass number is unchanged. The capture rate depends on the probability of finding the electron inside the nucleus and is therefore largest for 1s electrons (K capture decay)[GB05].

analysis.

2.3.1 Transition Rules

In this section, three types of interaction between light and atoms where electron transitions between two levels are involved (namely absorption, stimulated and spontaneous emission) will be described. In absorption, the electron goes from a lower level to an upper one and in emission the opposite happens. However, observations showed that not every transition between electronic energy levels in the atom is allowed. On the contrary, some are broadly observed, while some others are almost negligible. In order to understand these observations it is necessary to examine the transition probability between electronic energy levels.
The a and b eigen-states with energies E_a and E_b, respectively, are solutions of the Schrödinger equation for the hydrogen atom. The probability that a transition from state a occurs at time t^1, in state b after the perturbation of an oscillating electric field ^{2} is:

$$P_{a\to b}(t) \cong \frac{\pi e^2}{\epsilon_0 \hbar^2} | \langle \Psi_b | \vec{r} | \Psi_a \rangle |^2 \rho(\omega_0) t, \tag{2.35}$$

where $\omega_0 = (E_b - E_a)/\hbar$, $\rho(\omega_0)$ is the density of states and e is the electron charge [Gri05]. This probability accounts for absorption. The probability of stimulated emission $P_{b\to a}(t)$ is exactly the same. In the case of spontaneous emission (fluorescence), the external electromagnetic radiation responsible to excite the process is the “zero-point” radiation [Gri05].

One important quantity is the transition rate $R \equiv dP/dt$. The transition rate is derived from equation (2.35), and it is a constant quantity in time:

$$R_{a\to b} = \frac{\pi e^2}{\epsilon_0 \hbar^2} | \langle \Psi_b | \vec{r} | \Psi_a \rangle |^2 \rho(\omega_0). \tag{2.36}$$

Thus, the transition rate is reduced to evaluate the matrix elements of $\langle \Psi_a | \vec{r} | \Psi_b \rangle$. In order to evaluate the transition rate of the state a (characterized by the quantum numbers n', m' and l') to the state b (characterized with the quantum numbers n, m and l), one should evaluate the matrix elements of equation (2.36), as:

$$\langle \Psi_{n'l'm'} | \vec{r} | \Psi_{nlm} \rangle = \int\int\int \Psi^*_{n'l'm'} \vec{r} \Psi_{nlm} d\vec{r}, \tag{2.37}$$

---

[1] The perturbation time is very small compared with the mean transition time [Sim].

[2] The time dependent perturbation Hamiltonian is small compared with the time independent Hamiltonian, meaning that the strength of the perturbation is small [Gri05].

where the wave functions Ψ_{nlm} are given by equation (2.1).
Equation (2.37) can be solved easier in spherical coordinates. In such a case, the angular part of the wave functions of the hydrogen atom (equation (2.2)) will give rise to the conditions for the allowed transitions in terms of the quantum numbers l and m (see Appendix B (8.0.2))[Kak15].

The x and y component of the integral over ϕ give rise to the condition $\Delta m = \pm 1$, while the z component establishes that $\Delta m = 0$ are allowed transitions. Summarizing, the selection rule for the quantum number m is:

$$\boxed{\Delta m = 0, \pm 1}. \tag{2.38}$$

On the other hand, the z component of the integral over θ gives rise to the condition for the quantum number l, as:

$$\boxed{\Delta l = \pm 1}. \tag{2.39}$$

Equations (2.38) and (2.39) establish that electronic transitions that satisfy the selection rules are more probable. One example are the spontaneous emissions from $\mathrm{L_{II}}$ and $\mathrm{L_{III}}$ to K (see table 2.1). Another example of transitions with high chance to occur are those from $\mathrm{M_{II}}$ and $\mathrm{M_{III}}$ to K. These transitions are called “normal”. On the other hand, some transitions, e.g. $\mathrm{L_I}$ to K, are very unlikely to happen. Hence, electrons in the $\mathrm{L_I}$ state are trapped because there is not a lower level with $l = 1$. The $\mathrm{L_I}$ state is called metastable state, meaning that its lifetime is much longer than, for instance, the $\mathrm{L_{II}}$ or the $\mathrm{L_{III}}$; nevertheless, metastable states decay eventually. Transitions like $\mathrm{L_I}$-K, $\mathrm{M_{IV}}$-K or $\mathrm{M_V}$-K are called *forbidden transitions* because they do not follow the selection rules of equations (2.38) and (2.39). This name might be misleading since these transitions can actually happen; they are just less probable. Other type of transitions are associated with *satellite lines*, which arise from dual ionization [TDDL11]. The lifetime of an excited state can be long enough so that another electron is ejected from the atom before the vacancy is filled. In this case, the loss of a second electron modifies the energy levels in the atom, and other transitions can occur. Some of the normal, forbidden and satellite transitions are illustrated in figure 2.8 for transitions to the K level (K series).

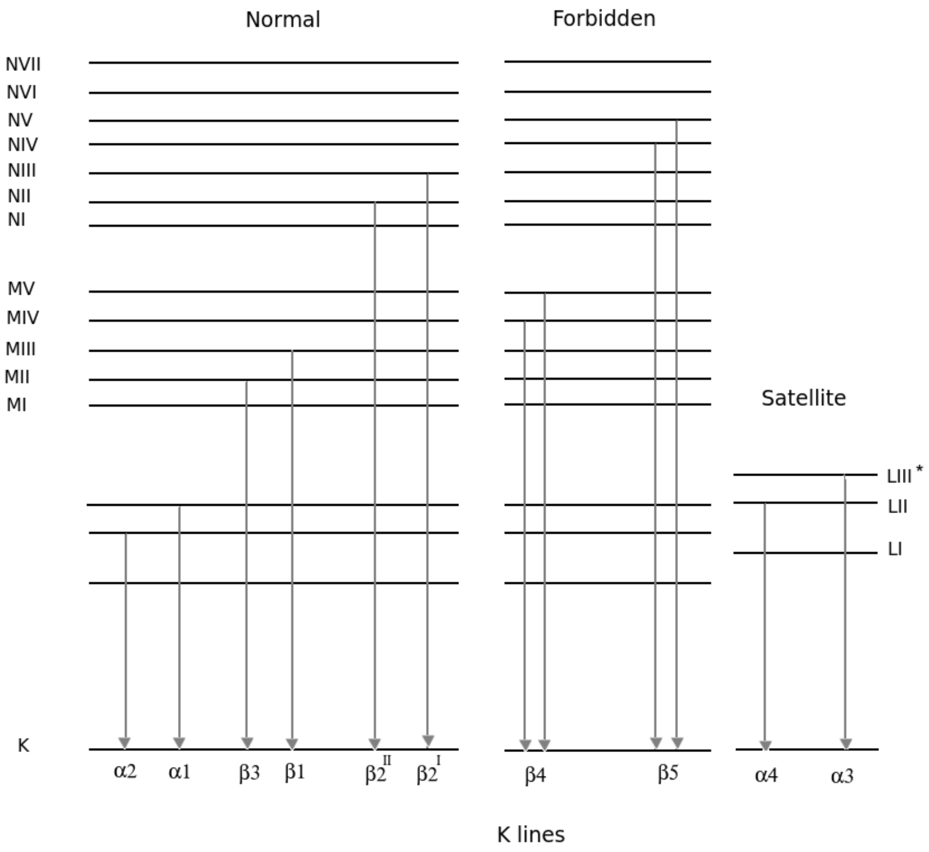

Figure 2.8: Normal, forbidden and satellite lines in the K series.

The transition nomenclature employed in spectroscopy is called *Siegbahn notation* [JMRS91]. The final level of the transition determines the *series* name, e.g. K, L, M, N. Each line in the series is called from stronger to weaker as $\alpha, \beta, \gamma, \delta \ldots$. Table 2.2 shows the relation between the Siegbahn and the IUPAC notations. Here, forbidden and normal transitions are included for the K series.

Siegbahn	IUPAC	Siegbahn	IUPAC	Siegbahn	IUPAC
$\mathrm{K}\alpha_1$	$\mathrm{K\text{-}L_{III}}$	$\mathrm{L}\alpha_1$	$\mathrm{L_{III}\text{-}M_{V}}$	$\mathrm{L}\gamma_1$	$\mathrm{L_{II}\text{-}N_{IV}}$
$\mathrm{K}\alpha_2$	$\mathrm{K\text{-}L_{II}}$	$\mathrm{L}\alpha_2$	$\mathrm{L_{III}\text{-}M_{IV}}$	$\mathrm{L}\gamma_2$	$\mathrm{L_{I}\text{-}N_{II}}$
$\mathrm{K}\beta_1$	$\mathrm{K\text{-}M_{III}}$	$\mathrm{L}\beta_1$	$\mathrm{L_{II}\text{-}M_{IV}}$	$\mathrm{L}\gamma_3$	$\mathrm{L_{I}\text{-}N_{III}}$
$\mathrm{K^{I}}\beta_2$	$\mathrm{K\text{-}N_{III}}$	$\mathrm{L}\beta_2$	$\mathrm{L_{III}\text{-}N_{V}}$	$\mathrm{L}\gamma_4$	$\mathrm{L_{I}\text{-}O_{III}}$
$\mathrm{K^{II}}\beta_2$	$\mathrm{K\text{-}N_{II}}$	$\mathrm{L}\beta_3$	$\mathrm{L_{I}\text{-}M_{III}}$	$\mathrm{L}\gamma'_4$	$\mathrm{L_{I}\text{-}O_{II}}$
$\mathrm{K}\beta_3$	$\mathrm{K\text{-}M_{II}}$	$\mathrm{L}\beta_4$	$\mathrm{L_{I}\text{-}M_{II}}$	$\mathrm{L}\gamma_5$	$\mathrm{L_{II}\text{-}N_{I}}$
$\mathrm{K^{I}}\beta_4$	$\mathrm{K\text{-}N_{V}}$	$\mathrm{L}\beta_5$	$\mathrm{L_{III}\text{-}O_{IV,V}}$	$\mathrm{L}\gamma_6$	$\mathrm{L_{II}\text{-}O_{IV}}$
$\mathrm{K^{II}}\beta_4$	$\mathrm{K\text{-}N_{IV}}$	$\mathrm{L}\beta_6$	$\mathrm{L_{III}\text{-}N_{I}}$	$\mathrm{L}\gamma_8$	$\mathrm{L_{II}\text{-}O_{I}}$
$\mathrm{K}\beta_{4x}$	$\mathrm{K\text{-}N_{IV}}$	$\mathrm{L}\beta_7$	$\mathrm{L_{III}\text{-}O_{I}}$	$\mathrm{L}\gamma'_8$	$\mathrm{L_{II}\text{-}N_{VI,VII}}$
$\mathrm{K^{I}}\beta_5$	$\mathrm{K\text{-}M_{V}}$	$\mathrm{L}\beta'_7$	$\mathrm{L_{III}\text{-}N_{VI,VII}}$	$\mathrm{L}\gamma_\eta$	$\mathrm{L_{II}\text{-}M_{I}}$
$\mathrm{K^{II}}\beta_5$	$\mathrm{K\text{-}M_{IV}}$	$\mathrm{L}\beta_9$	$\mathrm{L_{I}\text{-}M_{V}}$	L_l	$\mathrm{L_{III}\text{-}M_{I}}$
		$\mathrm{L}\beta_{10}$	$\mathrm{L_{I}\text{-}M_{IV}}$	L_s	$\mathrm{L_{III}\text{-}M_{II}}$
		$\mathrm{L}\beta_{15}$	$\mathrm{L_{III}\text{-}N_{IV}}$	L_t	$\mathrm{L_{III}\text{-}M_{III}}$
		$\mathrm{L}\beta_{17}$	$\mathrm{L_{II}\text{-}M_{III}}$	L_u	$\mathrm{L_{III}\text{-}M_{6.7}}$
				L_v	$\mathrm{L_{II}\text{-}M_{6.7}}$

Table 2.2: Some transistions expressed in Siegbahn and IUPAC notations [JMRS91].

3

BioXAS at P64

The characterization of metal centers in biological systems like metalloproteins by means of XAS requires the optimization of the standard experimental setup employed for materials science [AMKM03]. This type of experiments is commonly known as BioXAS. Biological samples present several features that make the XAS detection challenging: (1) low concentrations (in many cases the metal is bound to one or more amino acid chains with a high molecular weight and the protein is diluted in aqueous solution) (2) the amount of sample is limited and (3) radiation damage can alter the final spectrum.

The quality of the XAS signal depends mainly on these factors:

(i) X-ray source

(ii) beamline optics

(iii) sample preparation and environment

(iv) detector.

These features will be explained in detail for BioXAS at beamline P64, PETRA III (DESY) [MMRC16].

3.1 Synchrotron radiation

The term SR has its origins with the particle accelerator called "synchrotron". The synchrotron employs magnetic fields to bend the trajectory of charged particles into a closed path and an electric field to accelerate them. The magnetic field is synchronized with the electric field so that the path of the charged particles is constant in contrast to its predecessor the cyclotron. Nevertheless, the synchrotron radiation that is used for our kind of experiments is not directly produced by standard synchrotrons but by the so called *synchrotron light sources*, that include in the most of the cases a LINAC, a synchrotron (booster) and a storage ring [SRp]. The LINAC is a linear accelerator that is employed to accelerate the particles from zero kinetic energy. The synchrotron booster accelerates them further to a specific kinetic energy. After being pre-accelerated, the particles are magnetically kicked into a storage ring, which is a type of synchrotron that keeps the particles kinetic energy constant.

PETRA III is a synchrotron light source located at DESY, Hamburg. The original storage ring PETRA was an electron-positron collider in the 1980's and then became a pre-accelerator for the proton-electron collider HERA. PETRA III was build as one octant of the 2.3 km circumference storage ring of PETRA [PET]. The pre-accelerator system of PETRA III is composed by LINAC II, PIA and DESY II [LIN, DES] (see figure 3.1). LINAC II is a 70 m linear accelerator that produces electrons and accelerates them to a final energy of 450 MeV. The electrons are transformed into positrons[1] in the middle of LINAC II [DR, HS08]. Moreover, PIA (Positron Intensity Accumulator), a small storage ring of 24 m circumference, stores the particles produced by LINAC II and arranges them into bunches of $2{\cdot}10^{10}$ particles every 320 ms. DESY accelerates the particles to 6 GeV and finally delivers the bunches into PETRA III, where their energy is kept constant.

---

[1] An electron beam hits a tungsten target, producing polarized gamma rays that decay into positron-electron pairs [LIN, DA16]

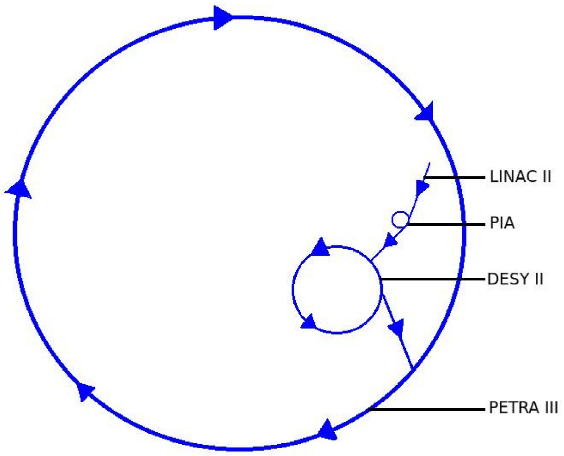

Figure 3.1: Schematics of the synchrotron light source PETRA III at DESY, Hamburg and its pre-accelerator system: LINAC II, PIA and DESY II.

In the storage ring, electrons or positrons are kept circulating at relativistic speeds with a constant energy [ANM01]. The particle in a storage ring is accelerated due to the deflection of its trajectory. When a charged particle is accelerated, a rearrangement of its electric field is required and this field perturbation, traveling away from the charge at the velocity of light, is what we observe as electromagnetic radiation [Wie03]. Particles in the storage ring move at relativistic speeds making the emitted radiation appearing to an external observer (in the laboratory system) as highly collimated in the forward direction within an angle of $1/\gamma$ called *natural opening* [Wie03], where $\gamma \equiv E/mc^2$, E is the particle's energy and m its mass. As mentioned before, the particles in the storage ring are not distributed evenly but in "bunches". Thus, the emitted radiation is produced when these bunches of particles are accelerated, making the light to have a pattern of short pulses, typically of 44 psec [mac].

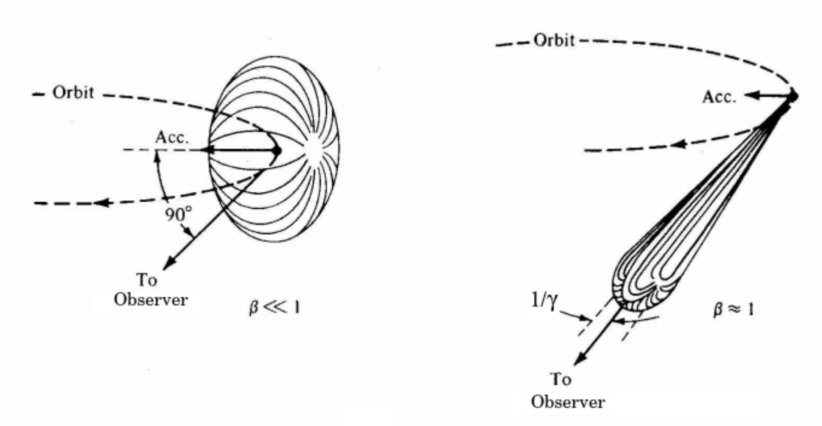

Figure 3.2: Emission pattern of SR, highly collimated towards the observer [TH56].

The particles acceleration is radial and lies in the horizontal plane (plane of the trajectory). Therefore, the electric field is parallel to the particles' orbit seen by an observer in the same plane. This means that the emitted radiation is linearly polarized in the horizontal plane. Above and bellow this plane, a polarization component perpendicular to the orbit is present and the radiation has an elliptical polarization (see figure 3.3) [MB99].

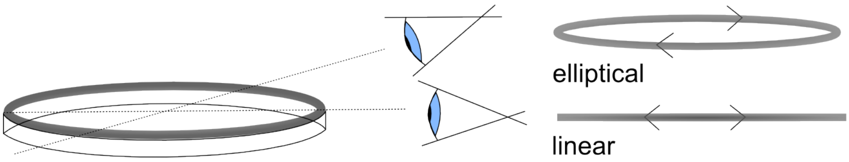

Figure 3.3: Linear and elliptical polarization of SR [SRp].

Brilliance is a parameter that comprises many aspects that are desired in a light source: flux, collimation of the beam, source area, and spectral distribution of the measured intensity. The greater the brilliance, the more photons of a given wavelength and direction are concentrated on a spot per unit of time. It is defined as:

$$\text{brilliance} = \frac{\text{photons}}{\text{second} \cdot \text{mrad}^2 \cdot \text{mm}^2 \cdot 0.1\%\text{BW}}, \tag{3.1}$$

where BW is the abbreviation for bandwidth.

One of the advantages of SR is that it has a broad spectrum and a high brilliance compared to x-ray tubes [ANM01]. The broad spectrum allows tuneability of energy that is a prerequisite for many experiments that require the use of x-rays, e.g. XAS, making the development of SR a key part for the development of such techniques.

The brilliance of PETRA III exceeds 10^{21} ph/s/mrad^2/mm^2/0.1%BW, being the most brilliant storage-ring based x-ray source world wide.

The specific characteristics of the emitted radiation depends on the type of deflection (bending magnets, undulators or wigglers)[Wie03]. For bending magnets, the critical photon energy (close to the maximum energy)[1] is proportional to the magnetic field and to the squared power of the particle's energy and inversely proportional to the third power of the particles mass.

The radiation characteristics of synchrotron light sources can be improved by adding so called *insertion devices*, e.g. undulators and wigglers. An undulator is an array of magnets that alternate the field up and down along the path [ANM01]. At each bend the electrons radiate and this radiation interferes constructively at each period (see figure 3.4). As a consequence, the emitted radiation is quasi-monochromatic and has high intensity proportional to the square of the number of periods of the undulator [Hof04]. The spectral characteristics of an undulator depend on its angular modulation. When the angular modulation is smaller than the natural opening $1/\gamma$ it is called *weak undulator*; on the other hand, if the angular modulation is larger than the natural opening it is called a *strong undulator*. Wigglers have an angular modulation much larger than the natural opening, where the condition of constructive interference is not satisfied.

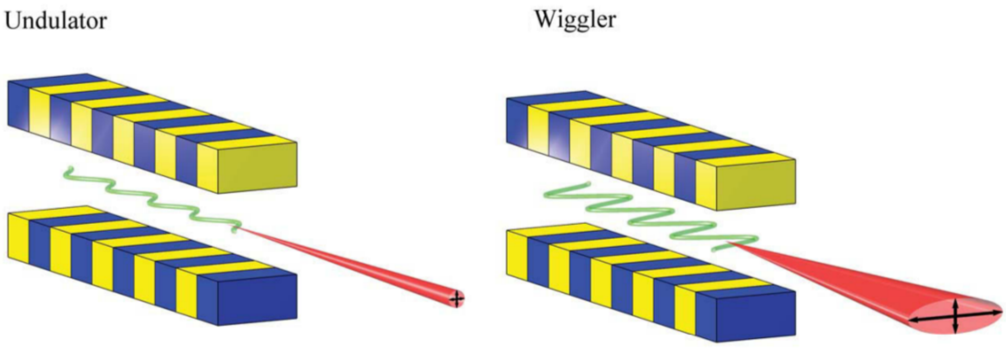

Figure 3.4: Illustration of undulators (on the left) and wigglers (on the right) [ANM01]

---

[1] Below and above the critical energy the total power is the same.

Bending magnets and insertion devices produce the same radiated power when $B = B_u/\sqrt{2}$ (where B_u is the magnetic field of the undulator and B of the bending magnet); however, the intensity of the undulator is concentrated in a narrower spectral range [SDRB14]. This way, undulators produce higher intensity than wigglers and bending magnets but the spectrum is not continuous. Due to interference effects, the undulator spectrum has several peaks called *harmonics*. Figure 3.5 shows the typical spectral distribution for bending magnets, wigglers and undulators [SRp].

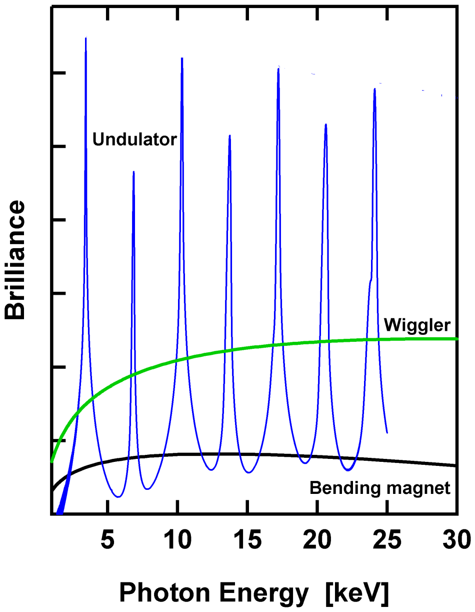

Figure 3.5: Spectral distribution of bending magnets, wigglers and undulators [SRp].

3.2 Beamline

A beamline is a tangential straight path to the storage ring circumference, where the emitted photons travel to an experimental station. PETRA III had originally 14 undulator based beamlines dedicated to different purposes. In February 2014, the *Extension Project* was started, adding 10 new beamlines in two new halls located at the north and at the east of the storage ring (see figure 3.6)[PEX]. Among them is the Time-Resolved- & Bio- X-ray Absorption Spectroscopy beamline P64 located at the Hall North. P64 is an undulator based beamline with 60 periods of 32.9 mm (see figure 3.7), with a calculated maximum flux on the sample of 10^{13} ph/s at 8.9 keV (see figure 3.7). The undulator at P64 is tunable; thus, by varying its gap[1] the energies of the first and higher harmonics are shifted [Iwa96].

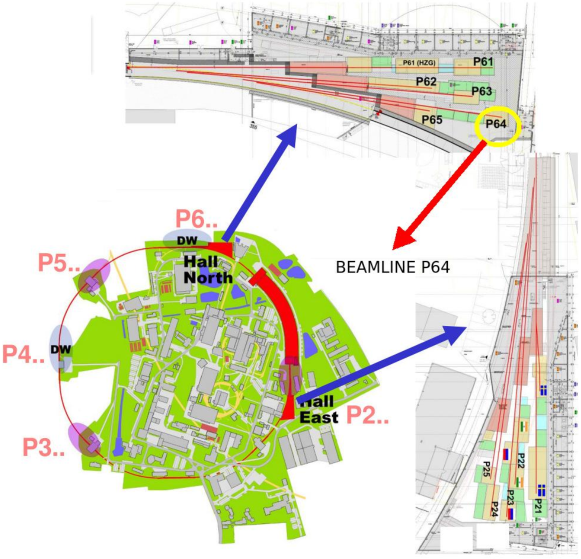

Figure 3.6: Schematics of the PETRA III extension project that includes 10 new beamlines located at the Hall East and Hall North [PEX].

The beamline optics allow to focus and tune the energy of the incoming SR beam. It usually includes a monochromator that selects the energy of the incident photons, using Bragg's law. Moreover, the optics contains mirrors that allow focusing and rejecting higher harmonics produced by the undulator. For XAS the tuneability of energy is the major feature since energy scans should be performed fast and accurately. For this purpose, P64 has a liquid N_2 cooled Double Crystal Monochromator with Si(111) and Si(311) reflections, resulting in a total energy range of 4.5-70 keV with a resolution of $\Delta E/E = 1.4 \cdot 10^{-4}$ and $5 \cdot 10^{-5}$, resp. The energy range is suitable for most of the absorption edges of elements that interact strongly with proteins, e.g. V, Cr, Mn, Fe, Co, Ni, Cu, Zn, Se, Br, Cd and Mo. By varying the undulator gap and moving the monochromator crystals simultaneously, the energy of the beam is selected.
Two mirrors with coatings of Si, Pt and Rh for different energy ranges allow to focus the beam in the vertical and horizontal direction from 2 mm × 1 mm (h×v) to a theoretically calculated size of 150 μm × 50 μm (h×v) as well as to reject higher harmonics.

---

[1] The undulator gap is a parameter that controls the angular modulation

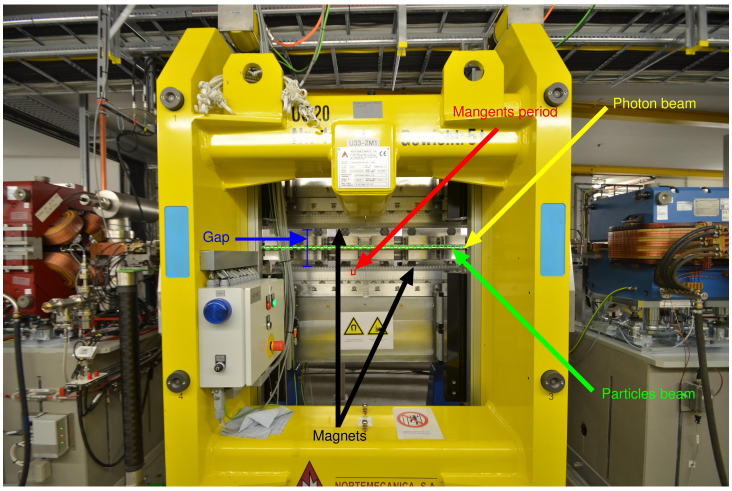

Figure 3.7: P64 undulator, localed in the PETRA III North Hall. On the photo, the photons and particles beams are illustrated (see figure 3.4). The magnetic periodic arrays are also illustrated, as well as their period and the gap between the them (of 21 cm in the photo).

The beamline optics is illustrated in figure 3.8, where the monochromator and mirror chambers are visible.

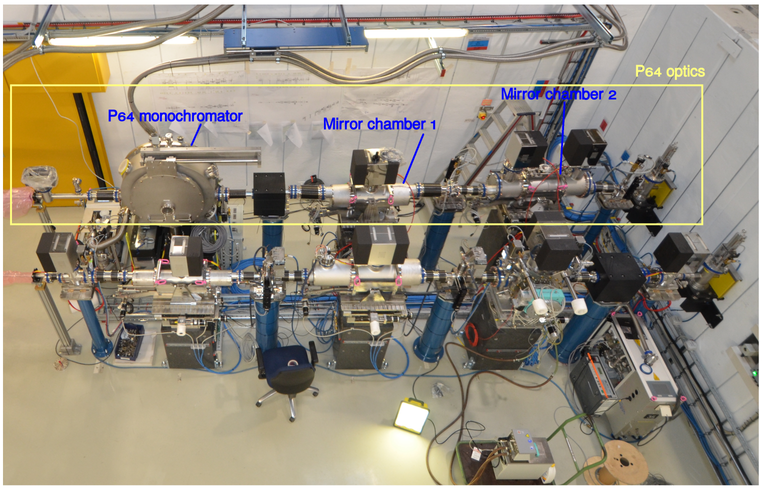

Figure 3.8: Beamline P64 optics hutch. The photo includes the beamline optics of P64 (above, enclosed in the yellow rectangle) and P65 (below). P64 optics include: the liquid nitrogen cooled monochromator, a first mirror chamber for horizontal focusing and a dynamically bent second mirror chamber for vertical focusing.

In BioXAS, the sample volume is a critical point[1]. At a high flux beamline like P64 the quantity of protein required can be lowered. In order to reduce radiation damage, the samples can be cooled to temperatures in the range of 4–290 K with a closed cycle cryostat with sample cell, and He exchange gas and with a motorized sample holder for 5 samples. The He exchange gas ensures that the whole sample is at the same, low temperature, and not just the part of it that is connected to the cold finger of the cryostat.

3.3 Setups

XAS requires a precise measurement of the absorption coefficient μ as a function of the incident x-ray energy E. From equation (2.15), μ is given as:

$$\mu \propto \ln\left[\frac{I}{I_0}\right]. \tag{3.2}$$

Hence, the incident and transmitted intensities are the objective quantities to be measured in a XAS experiment. To measure I_0 and I it is sufficient to use ionization chambers, which are parallel plate capacitors filled with gas. High voltage is used to separate the electrons from the ions which are created within the gas by the incident radiation. The resulting current is proportional to the number of absorbed photons.

Figure 3.9 shows the setup employed for XAS measurements in transmission geometry. The SR source produces a polychromatic beam that passes through a double crystal monochromator which selects the energy of the x-rays. After that, the monochromatic beam goes through a first ionization chamber that measures the incident intensity on the sample. Then, the beam is partially absorbed, partially transmitted through the sample, and a second ionization chamber is placed behind the sample to measure the transmitted x-ray intensity I.

---

[1] The sample holder depends on the type of samples and it is usually brought by the users to the beamline.

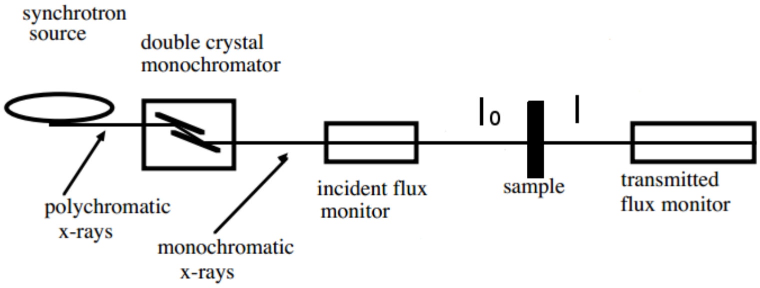

Figure 3.9: Transmission mode XAS setup.

Biological samples contain proteins with metal centers at low concentrations which results in a very small fraction of absorption being caused by the interesting atom and therefore in a very low signal-to-background ratio. Figure 3.10 shows the XAS spectrum of a sample that contains Cu at a concentration of 600 μmol/L measured in transmission mode. In this case, the absorption edge position is not identifiable and the structure of oscillations is not visible.
Since fluorescence is proportional to absorption, it can be used as an indirect measurement of XAS. The fluorescence mode works as follows: a fluorescence detector is added to the transmission setup of figure 3.9. The detector is usually placed in the plane of polarization, 90° to the incident beam in order to minimize scattering effects, making use of the linear polarization of SR. The setup of the fluorescence mode of XAS is illustrated in figure 3.11.

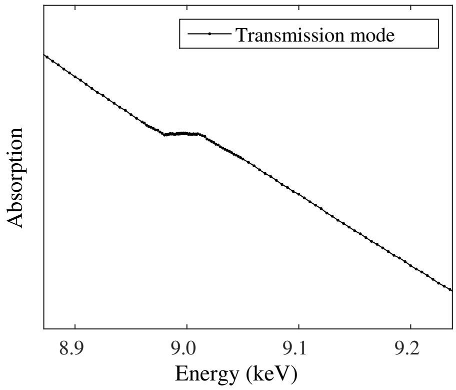

Figure 3.10: Transmission mode XAS spectrum of an ultra diluted sample.

The detector collects the total fluorescence emitted from the sample in a solid angle given by the detector size and distance. Figure 3.12 shows a XAS spectrum of the sample containing Cu at 600 μmol/L, measured with the total fluorescence signal recorded by a Passivated Implanted

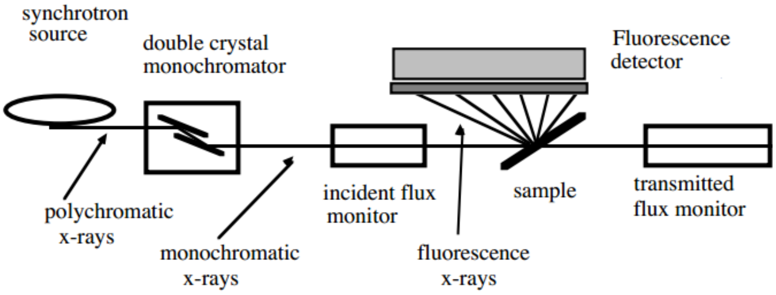

Figure 3.11: Fluorescence mode XAS setup

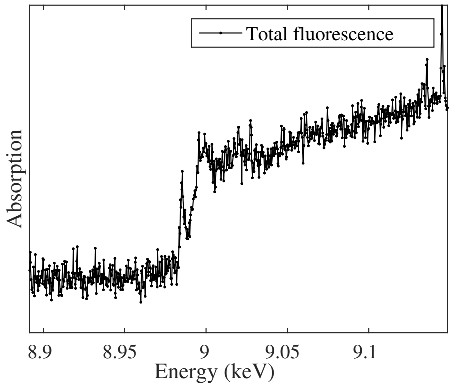

Figure 3.12: Fluorescence mode XAS spectrum of an ultra diluted sample, measured with the PIPS detector (total fluorescence)

Planar Silicon detector (PIPS), which is a large[1] photo-diode detector, measuring all emitted photons as a function of incident x-ray energy [2]. Although it shows the absorption edge position of Cu, it is too noisy to be analyzed. The total fluorescence signal contains different kinds of scattered photons that reach the detector including fluorescence of other elements.

In order to collect only fluorescence photons of the element of interest, an energy dispersive detector based on a semiconductor, such as germanium or silicon has been chosen. With an energy dispersive detector a current proportional to the incoming photon energy is measured, and reduced to a histogram of photon energies (spectrum). This spectrum will contain peaks at the energies of the incoming fluorescence or scattered photons. One point in the XAS spectrum would correspond to the total number of counts within a region of interest (ROI) that contains only the fluorescence peak of the element under study, normalized with the incident intensity I_0.

---

[1] detector's area is 3000 mm^2. [pip]

[2] The experiment was done in continuous mode and the energy step width was ~1 eV.

In order achieve better statistics, a multipixel energy dispersive detector is chosen. The detector and electronics can handle a maximum number of photons per second with reasonable energy resolution, independently on the detector's size. Increasing the number of pixels (each with its own read out electronics) increases the number of photons per second that can be handled.

The complete setup for BioXAS at P64 includes the optical components (monochromator and mirrors) to select the energy and to focus the beam, an ionization chamber to detect the incident intensity on the sample I_0 (for normalization purposes) and a multi-pixel energy dispersive detector, in this case a 100PixHPGe. The schematics of the setup for BioXAS experiments at P64 are shown in figure 3.13. The highly brilliant incident photon beam comes from the undulator and it is monochromatized by a double crystal monochromator. The beam is further focused with mirrors and it is ready to pass through the first ionization chamber (I.C.1), where the incident intensity is recorded. The trajectory follows to further hit the sample, which is positioned at 45° to the incident beam direction, where part of the incident intensity is absorbed. Followed by the sample, a second ionization chamber (I.C.2) is placed to detect the transmitted intensity. After absorption, fluorescence processes will take place and this signal is isotropically emitted from the sample. The 100PixHPGe is placed at 90° to the incident beam in order to collect as much as fluorescence signal as possible and to reduce the scattering signal using the horizontal polarization of the incident beam. The read-out electronics will create histograms of photon energies (spectra) for each pixel. The data are automatically reduced from 100 fluorescence spectra to one point in the XAS spectrum. The incident beam energy is tuned through the energies of the absorption edge of the element under study in order to measure the final XAS spectrum.

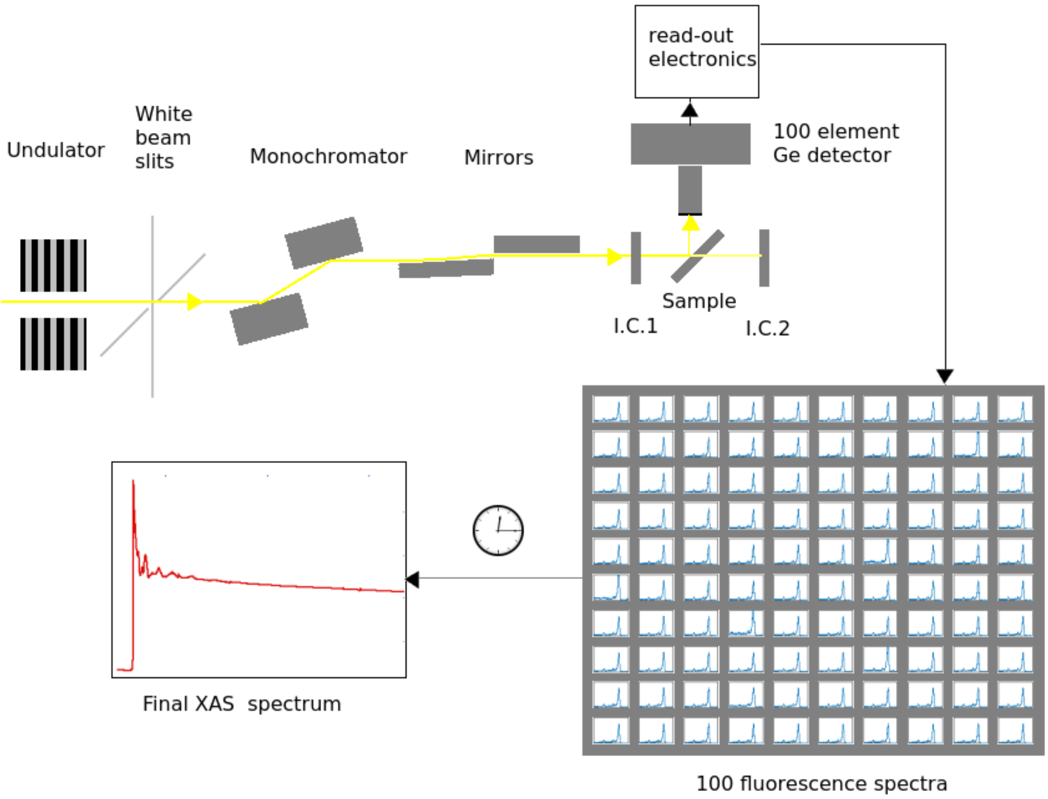

Figure 3.13: Schematics of the setup for BioXAS experiments at P64.

3.4 Detectors and electronics

Due to the relative low absorption dilute systems require XAS in fluorescence mode in order to achieve better signal to noise ratio. For this purpose, a 100PixHPGe is available at beamline P64. This is a state of the art segmented single crystal detector, manufactured by *CANBERRA Industries* (see figure 3.14).

The Ge monolithic crystal is segmented into 100 pixels by means of photolithographic techniques, allowing a packing density (detector area/total area circumscribed by the array) of virtually 100% because there is hardly any dead space between pixels. The Ge crystal has an area of 5×5 cm, with a pixel area of 5×5 mm and 7 mm thickness. The detector can be placed closer to the sample in order to increase the covered solid angle[1].

Figure 3.14: 100PixHPGe and read-out electronics.

The mechanism of charge collection in the 100PixHPGe or in any germanium detector is based on the creation of electron-hole pairs[2]. The incoming photon creates a number of electron-hole pairs proportional to the photon energy and this charge is subsequently collected using an electric field. The energy gap between the valence band and the conduction band for Ge is 0.67 eV. Therefore, in order to avoid electrons to go into the conduction band because of thermal effects, the detector should be cooled to liquid nitrogen temperatures (77 K).

Each pixel is connected to a preamplifier which collects and converts the charge into a voltage signal. The output signal of the preamplifier as a function of time looks like a sequence of steps whose relative heights (voltage) are proportional to the energy of the absorbed photon (figure 3.15).

---

[1] For the 100PixHPGe at 10 cm from the sample, the covered area related with the total area of the sphere is 2% while at a distance of 30 cm is 0.2%.

[2] The working principle is the *Schottky diode*, i.e. a semiconductor diode formed by the junction of a semiconductor with a metal.

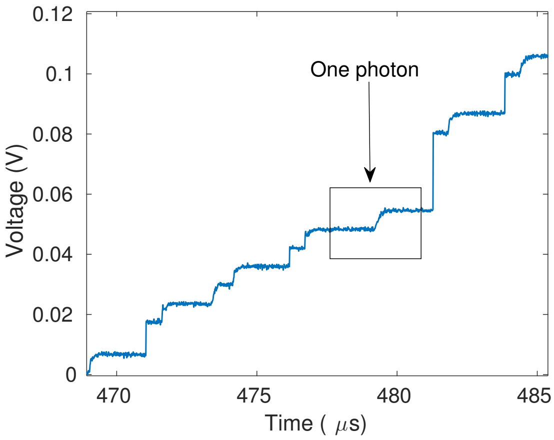

Figure 3.15: Preamplifier output signal as a function of time. Each step represents a photon, and its height (measured in voltage) is proportional to the photon energy.

Every preamplifier is connected to one channel of an “Analog-to-Digital Converter (ADC) module” that process the incoming signal in three stages: shaping it into a trapezoidal shape, determining the height of the trapezoidal shape and histogramming these values. For this purpose, the beamline P64 has 13 boards of the SIS3302 14xx Firmware-Gamma module, with 8 channels each (Struck [Str]), allowing to convert up to 104 signals in parallel at 16 bit dynamic range. The electronic modules are positioned with the detector in the experimental hutch. There, the aluminum case is sufficient to protect them from the radiation.

In order to obtain the trapezoidal shape, the incoming signal is first processed through a Moving Average Window (MAW) illustrated in figure 3.16. This process works as follows:

1. **MA1**: Perform a first Moving Average Unit (MA), that consist on:
    a. Delaying the signal by a parameter called *peaking time*.
    b. Subtracting the delayed signal from the original signal.
    c. Perform a cumulative summation.
2. **MA2**: Delay the first MA by a parameter called *gap time*.
3. Subtract MA1 from MA2, obtaining a trapezoidal shape.

The height of the trapezoidal shape is proportional to the energy of the incoming photon. The result of it for a single photon is shown in figure 3.17.

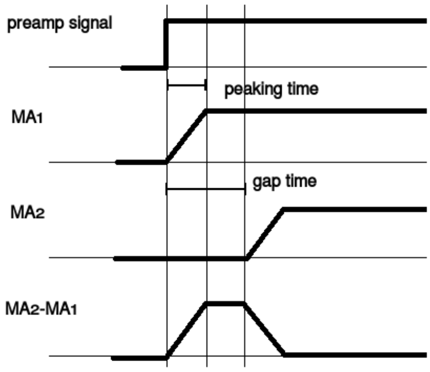

Figure 3.16: Signal schematics of the MAW that process the incoming signal into a trapezoidal shape.

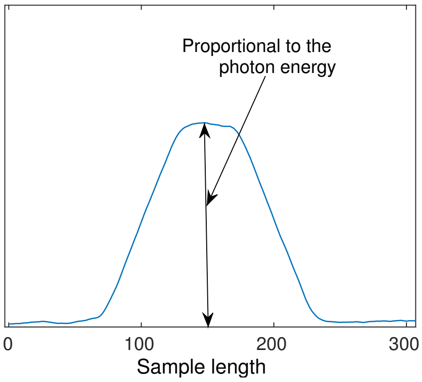

Figure 3.17: Trapezoidal shape of a single photon determined with the MAW.

The determination of the trapezoidal shape height is a key point for the energy resolution of the final spectrum. The flatter the plateau, the more accurate its height can be determined and therefore the energy of the photon. The peaking time and gap time should be long enough for this purpose. However, if they are too long, the maximum counting rate, which can be handled by the electronics, is significantly reduced since two consecutive photons cannot be separated by the electronics anymore and two photons of energies E_1 and E_2 are converted as one with the energy $E_1 + E_2$. A histogram of the height of the trapezoidal shapes is calculated by the ADC modules resulting in a fluorescence spectrum. The detector produces 100 fluorescence spectra at a single incident beam energy and the energy resolution of most of the pixels is below 260 eV Full Width Half Maximum (FWHM) at the Mn Kα line for moderate intensity flux (10^5 counts/s/pixel). Figure 3.18 illustrates the fluorescence spectrum of Mn for the pixel number 1 (see the arrangement of pixels in figure 4.1). For this pixel, the FWHM of the Mn Kα line is 197 eV.

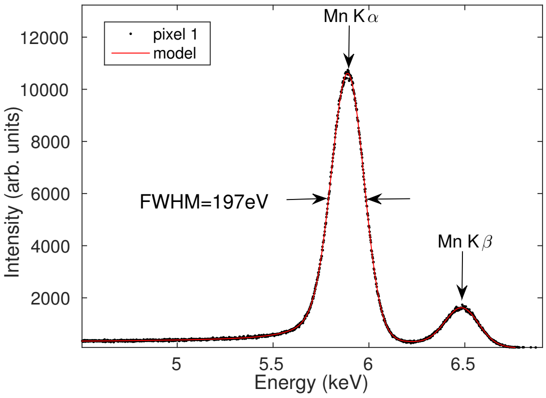

Figure 3.18: Fluorescence spectrum of Mn for the pixel number 1 of the 100PixHPGe (see figure 4.1).

4

Features of the spectra

The spectrum collected by the 100PixHPGe and electronics has some characteristics that are due to the detection system and some that are a response to physical phenomena. The physical aspects are related to the interaction of photons with matter: fluorescence, elastic (coherent) scattering and inelastic (incoherent) scattering. These three effects are represented as three different peaks in the spectrum. On the other hand, some features of the spectra correspond to artifacts created by the detection system (detector and electronics) like incomplete charge collection, escape peaks, and pile-up.[VJA+95].

In this chapter the nature of these features will be explained in order to understand better the emission spectra collected with the 100PixHPGe.

4.1 Coherent and incoherent scattering

Coherent scattering by bound electrons is known as Rayleigh scattering and occurs when the oscillating electric field of the light wave acts on the charged particles within the sample causing them to move at the same frequency. The particles in the sample become radiating dipoles, whose radiation is observed as scattered light with the same incident energy. On the other hand, in the incoherent scattering process by bound electrons, known as atomic Compton, the energy of the scattered photon decreases. The final energy is:

$$E_f = \frac{m_e c^2 E_o}{(1 - \cos\theta) E_o + m_e c^2}, \tag{4.1}$$

where E_f and E_o are the final and initial energy, respectively, θ is the scattering angle [1], m_e is the electron mass, and c is the vacuum speed of light.
The differential scattering cross sections (Rayleigh and atomic Compton) in the case of a polarized beam in the horizontal plane[2] are [Han86]:

$$\begin{aligned} \frac{\mathrm{d}\sigma_R}{\mathrm{d}\Omega} &= r_e^2 \cos^2\theta F(q,Z)^2 \\ \frac{\mathrm{d}\sigma_{aC}}{\mathrm{d}\Omega} &= \frac{r_e^2}{2}\left(\frac{E_f}{E_o}\right)^2 \left[\frac{E_f}{E_o} + \frac{E_o}{E_f} - 2\sin^2\theta\right] S(q,Z), \end{aligned} \tag{4.2}$$

where r_e is the classical electron radius, F is the atomic form factor, S is the incoherent scattering function, Z is the atomic number, and q is the momentum transfer [HVB$^+$75], defined as:

$$q = \frac{4}{\pi\lambda}\sin\frac{\theta}{2}, \tag{4.3}$$

where λ is the photon wavelength.

In order to evaluate the angular dependence, let us consider the case of free electrons where coherent scattering is better described with the Thomson differential cross section ($\mathrm{d}\sigma_T/\mathrm{d}\Omega$) and incoherent scattering with the Klein-Nishina differential scattering cross section: ($\mathrm{d}\sigma_{KN}/\mathrm{d}\Omega$):

$$\begin{aligned} \frac{\mathrm{d}\sigma_T}{\mathrm{d}\Omega} &= r_e^2 \cos^2\theta \\ \frac{\mathrm{d}\sigma_{KN}}{\mathrm{d}\Omega} &= \frac{r_e^2}{2}\left(\frac{E_f}{E_o}\right)^2 \left[\frac{E_f}{E_o} + \frac{E_o}{E_f} - 2\sin^2\theta\right]. \end{aligned} \tag{4.4}$$

In the limit of $E_f = E_o$, they become identical: $\mathrm{d}\sigma_{KN}/\mathrm{d}\Omega = \mathrm{d}\sigma_T/\mathrm{d}\Omega$.
The behavior of equations (4.1) and (4.4) tells us that in the forward direction $\theta = 0°$ (small angle scattering) scattering is mainly coherent, since $E_f \approx E_o$. Furthermore, at $\theta = 90°$ total scattering (Klein-Nishina) has a minimum and coherent scattering is zero. The latter condition is ideal for fluorescence measurements where it is important to minimize the background signal. Nevertheless, the signal is not detected uniquely from one single point because a real detector has some finite dimensions, which makes it impossible to have zero coherent scattering even when the center of the detector is placed exactly at $\theta = 90°$. Thus, placing the detector perpendicularly to the incident beam decreases the coherent scattering intensity but does not eliminate it.

---

[1] θ, as defined here, corresponds to the angle between the photon directions of travel prior to and following a scattering interaction. From the pure geometrical point of view, it is related to the Bragg angle ϕ in x-ray crystallography as $\theta = 2\phi$ [HVB$^+$75].

[2] As it is for SR, see figure 3.3

The position of the incoherent scattering peak for a fixed incident energy depends on the angle θ (see equation (4.1)). For the given setup (see figure 4.1) this leads to a dependency with the detector column. Figure 4.2 shows the effect of the scattering angle on the energy shift at an incident energy of 10.045 keV. The larger the angle, the further away the incoherent peak would be from the coherent one. In terms of the detector arrangement, the pixels 91–100 show a larger separation between the scattering peaks than the pixels 1–10 (see Figure 4.1).

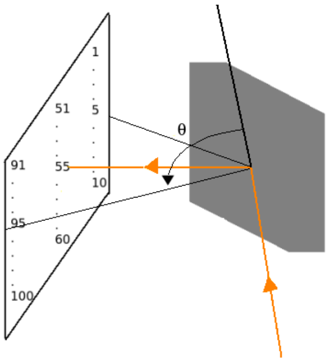

Figure 4.1: Arrangement of pixels in the 100PixHPGe with respect to the sample.

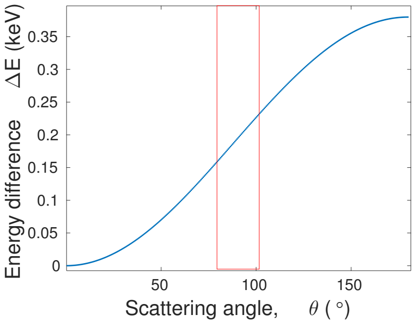

Figure 4.2: Energy difference vs. the scattering angle at an incident energy of 10.045 keV. If the detector is placed at 15 cm from the sample, the angular range is from about 80.5° to 99.5° (shown in a red rectangle).

Figure 4.3 shows a simulation of the scattering peaks for different detector pixels at an incident energy of 10.045 keV and at a distance of 30 cm from the sample (created with the software XMI-MSIM [XMI]). The simulation illustrates the change in the width of the scattering line depending on the detector column. The simulated data are compared to real data obtained with the detector at the beamline P11 (PETRA III, DESY) at the same incident energy and at the same distance from the sample. Figure 4.4 shows that widening of the scattering peak occurs at larger scattering angles. Nevertheless, the simulation does not match the experimental data perfectly, because of a shift of the detector center with respect to the sample center in the experiment.

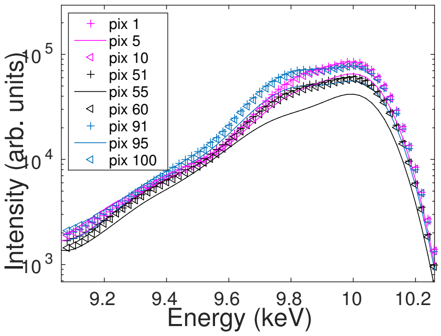

Figure 4.3: XMI-MSIM simulation of the scattering peaks for different detector columns at the incident energy of 10.045 keV

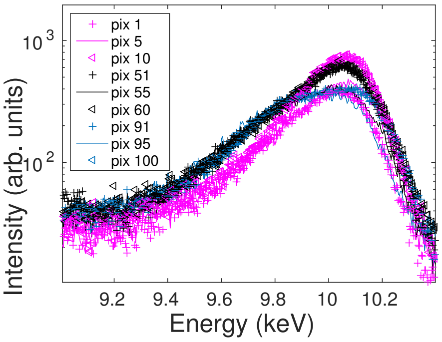

Figure 4.4: Scattering peaks for different detector columns at 10.045 keV. The data were measured with the 100PixH-PGe at P11 (PETRA, DESY).

The scattering line at energies close to 10 keV is only widened depending on the detector's column; however, at higher energies the incoherent peak is resolved from the coherent one. The reason for that is that the final energy depends on the angle as well as on the incident energy (equation (4.1)). Figure 4.5 shows that at energies of 15 keV or above the incoherent and coherent peaks are resolved.

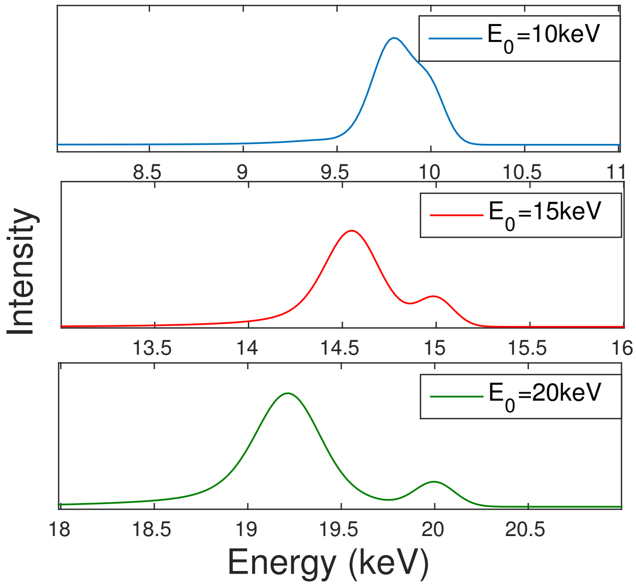

Figure 4.5: Scattering peaks at the incident energies of 10, 15 and 20 keV at the scattering angle of 90°. The incoherent and coherent scattering are resolved for 15 and 20 keV.

4.2 Incomplete charge collection

for photons with a fixed energy the detector produces a statistical distribution of voltages (proportional to the photon energies) with a skewness towards lower voltages. This effect is known as *incomplete charge collection* and it is a consequence of the inherent inefficiency of the charge-collecting system in the detector (no process has an efficiency of 100%) and because the recombination of electron-hole pairs split between two pixels. Its representations in the spectra are long tails at the lower energies of the peaks as shown in figure 4.6.

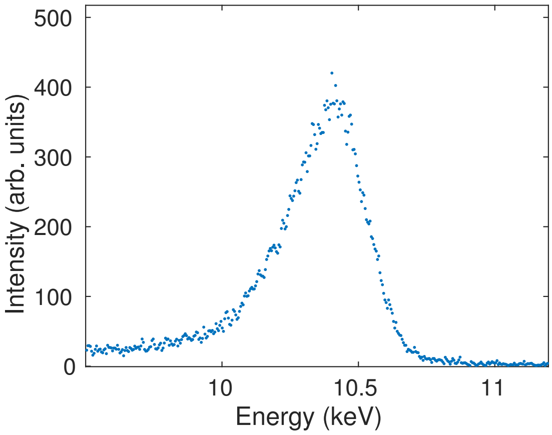

Figure 4.6: Long tail at lower energies of the scattering peak as a consequence of incomplete charge collection.

4.3 Escape peaks

Escape peaks are additional lines in the spectrum that occur when the energy of the photon impinging the detector crystal is larger than the energy of the absorption edge of the detector material. In such a case, the energy of an absorbed photon is partially converted into electron-hole pairs and partially employed to generate fluorescence x-rays. As a consequence, escape peaks are located at the energy difference of any measured interaction (fluorescence, scattering, etc) and the fluorescence energy.

At energies higher than the energy of the absorption edge of germanium (K1s=11.103 keV), two escape peaks occur at the energies:

$$\begin{aligned} E_{esc\alpha} &= E_{ph} - E_{K\alpha} \\ E_{esc\beta} &= E_{ph} - E_{K\beta}, \end{aligned} \tag{4.5}$$

where $E_{esc\alpha}$ and $E_{esc\beta}$ are the energies of the first and second escape peaks, E_{ph} is the energy of the photon hitting the detector, and $E_{K\alpha} = 9.876\,\text{keV}$ and $E_{K\beta} = 10.983\,\text{keV}$ are the $K\alpha$ and $K\beta$ fluorescence energies of germanium respectively.

In order to model the response function of one of the pixels of the 100PixHPGe, the software XMI-MSIM [XMI] has been employed. The simulation accounts for monochromatic 13 keV x-rays polarized in the horizontal plane, impinging on a sample at 45° to the incident x-ray beam. A single pixel Ge detector of dimensions 5 mm×5 mm×7 mm (width×height×thickness)[1] is placed 5 cm from the sample, forming an angle of 45° with the sample and one of 90° with the incident x-ray beam. The sample is chosen to be Cu diluted in H_2O at 0.001%.

Figure 4.7 shows the simulation calculated with XMI-MSIM [XMI]. The response function presents the coherent scattering peak at the incident energy of 13 keV and the incoherent scattering peak at the energy of E_f =12.7 keV. In this case, the simulated pixel has the number 55 which is a central pixel in the detector. The incident energy allows to resolve partially the coherent and incoherent peaks. Fluorescence peaks of Cu (Kα and Kβ) are also present at the corresponding energies of 8.04 keV and 8.90 keV[2]. Furthermore, the incident energy is above the K1s energy of Ge, and 4 escape peaks ($E_o - E_{K\alpha}$, $E_o - E_{K\beta}$, $E_f - E_{K\alpha}$ and $E_f - E_{K\beta}$) are present in the spectrum. The Cu $K\alpha - \beta$ energies are lower than the Ge $K\alpha - \beta$ energies; therefore the response function does not display escape peaks for the Cu fluorescence lines.

---

[1] which correspond to the real dimensions of one of the pixels

[2] Fluorescence from H and O (low energies) has low penetrating power and is completely absorbed because the beam passes through air and Be window. For this reason the spectra does not exhibit the fluorescence peaks of H and O.

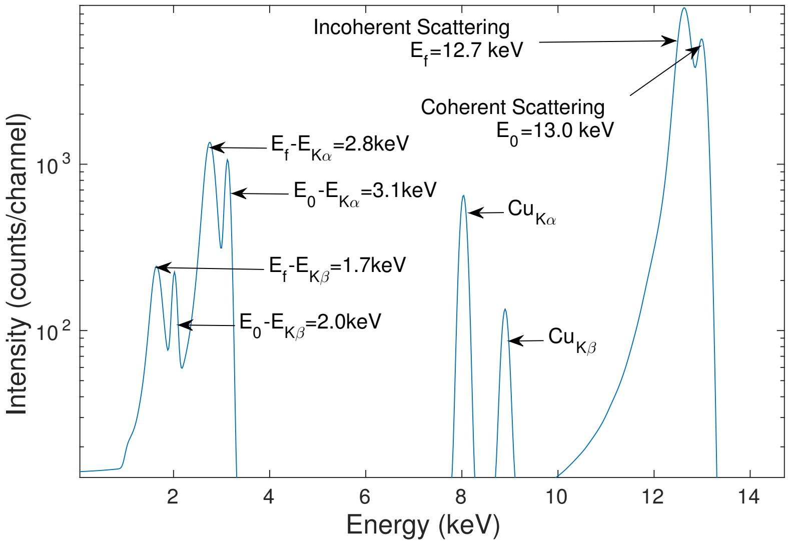

Figure 4.7: Spectrum of a Ge detector simulated with the software XMI MSIM. The spectrum presents the scattering lines (Thomson and Compton), the fluorescence lines of Cu Kα and Kβ, and the escape peaks from the scattering lines. The incident energy on the H_2O, Cu sample is 13 keV.

4.4 Pile-up

When two ore more photons hit the detector within a small time range, the read-out electronics process them as a single photon with an energy equal to the sum of the individual photon energies. This effect is known as pile-up and creates artificial extra peaks in the spectra [Dat75] as seen in figure 4.8 for a Ge spectrum at the incident energy of 30 keV[1][2]. The pile-up peaks show up at the energies corresponding to the sum of two Kα photons, the sum of Kα and Kβ photons and the sum of two Kβ photons. Pile-up is more probable to occur at higher incident fluxes [Dav07]; therefore, the pile-up peak corresponding to the sum of two Kβ photons has a lower probability than the first two mentioned ones, and does not show up in the spectra.

---

[1] Data courtesy of Martin Tolkiehn.

[2] In this case the fluorescence peaks are much stronger than the scattering peaks (that are almost not visible).

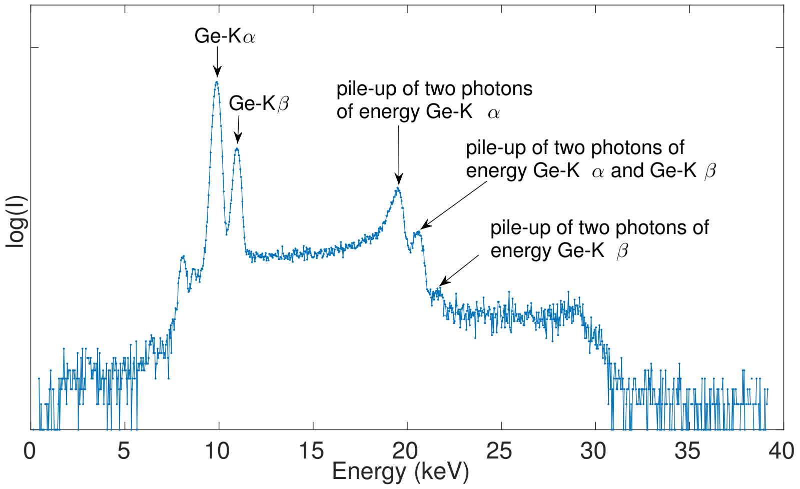

Figure 4.8: Ge wafer spectrum detected with a one pixel High-Purity Germanium Detector (HPGe). The pile-up of Kα +Kα photons as well as of Kα + Kβ is indicated.

Some of the pile-up events can be rejected by selecting suitable parameters on the read-out electronics, so that if two or more events are detected in a certain range of time they are not to be counted. This works with two different MAW (see section 3.4), one dedicated to count photons (also called fast filter) and another one to detect their energy (also called energy filter). For the fast filter the parameters of *peaking time* and *gap time* are selected so that each photon is represented as a peak and can be counted, independently on the plateau of the trapezoidal shape, since this filter is not to calculate energy. Every time two or more photons are counted with the fast filter the event is rejected. Certainly, this method only rejects some events but pile-up would still be present for events that come in a shorter time range.

5

Data reduction for BioXAS experiments at P64

The main goal is to reduce the $[n \times m \times N]$ data set into a final spectrum of length n, where n is the number of incident energies, m is the length of a fluorescence spectrum, and N is the number of detector pixels. In a typical experiment $m = 2048$ (number of spectrum channels) and n depends on the XAS region (see section 2.2.3). Usually, a total XAS spectrum has 500 points, meaning that $n = 500$. For background subtraction, the measurement starts far below the edge and has around 150 points in the XANES region[1] with a $\Delta E \sim 0.25\,\mathrm{eV}$. For the EXAFS region the ΔE is chosen so that Δk is linear (see equation 2.30). This way ΔE in the EXAFS region is in the range between $2\,\mathrm{eV}$ and $10\,\mathrm{eV}$.

The data reduction includes a determination of the final fluorescence spectrum per incident energy, meaning a reduction of $N \rightarrow 1$. It requires a further extraction of the counts in the fluorescence line of interest, meaning a reduction of $m \rightarrow 1$. This will build up the final XAS spectrum of length $[n]$. The last step is the most challenging one in the data reduction process due to the overlap of the fluorescence line of interest with the scattering peaks [MMRC16].

5.1 Data reduction per incident energy

Spectra of different pixels can be compared if an alignment is made based on an energy calibration. This is done with an interpolation that changes the channel axis to a energy axis. This way, the spectra is not only aligned but also calibrated. A reference sample was used for the

---

[1] Here considered as XANES and NEXAFS.

energy calibration of each pixel and used to align the spectra per incident energy automatically.

Reducing N fluorescence spectra at a single incident energy could be done in principle by taking an average. Nevertheless, this approach is not completely accurate since there can be several artifacts coming from some pixels that should not be taken into account e.g. Bragg peaks from small crystalline parts of the sample or sample holder, which hit only a few detector pixels and might hit different pixels at different energies (called *glitch*). In general any feature that is distant from the other observations (outlier) is to be rejected.

In order to reject those pixels and in general pixels with low performance, a comparison at a fixed incident energy between each fluorescence spectrum with the average spectrum over the N pixels is performed. If the difference between them is larger than a certain threshold, the analyzed spectrum is rejected from the final average.

We evaluate the difference between one spectrum S_i and the average spectrum over the N pixels $\hat{S}$, as:

$$\mathrm{Diff}_i = \hat{S} - S_i, \tag{5.1}$$

where $i = 1, 2, \ldots, N$ indicates the pixel number.
For understanding purposes, we can study photons with the same energy interacting with the detector. The standard deviation of the number of interacting photons per pixel is called *photon shot noise* [Jan07]. In the classical limit the shot noise is described by the classical Poisson probability, and it is the squared root of the average value of interacting photons per pixel:

$$\sigma^j_{\mathrm{SHOT}} = \sqrt{\hat{S}^j}, \tag{5.2}$$

where $j = 1, 2, \ldots, m$ is the index of the photon energy.

If we consider now the complete range of fluorescence energies, we require that the difference between each fluorescence spectrum per pixel and the average spectrum should be less than the shot noise, so that $\mathrm{Diff}^j_i \leq \sigma^j_{\mathrm{SHOT}}$ for every $j = 1, 2, \ldots, m$. On the contrary, if $\mathrm{Diff}^j_i > \sigma^j_{\mathrm{SHOT}}$ for any $j = 1, 2, \ldots, m$, there is a feature that is not explained within the Poisson statistics and should not be considered for the final fluorescence spectrum per incident energy.

The method is tested on real data at the incident beam energy of 8.98 keV with the sample [$Cu_2(NGuaSSGuaN)_2](OTf)_2$ ($system_1$)[1] with a low concentration of 600 μmol/L, measured at beamline P11 with beam attenuation of $\sim$ 8000. Figure 5.1 shows a region of the fluorescence spectrum[2](blue) for each detector pixel, compared to the average spectrum (red). When any entry of the difference between the average and the spectrum (green) is larger than the shot noise (magenta), the pixel is rejected (black background). The rejected pixels show broader peaks than the average. This is a sign of lower energy resolution. Furthermore, some pixels were deactivated to avoid of crosstalk effects (grey background).

As an alternative to delete artifacts like glitches or affected read-outs, the median is used in astronomy applications[MTT97]. Figure 5.2 shows the comparison between the average spectrum over the 100 pixels (black), the average corrected with the method explained above (red), where the shot noise was taken as a rejection criterion and finally an spectrum calculated as the median of the 100 spectra (green). The corrected average and the median show a decrease in intensity in the region of overlapping between the scattering peak and the CuKα and at the right side of the scattering peak. The time of calculation of the corrected average is $\sim$ 2 ms while for the median is $\sim$ 4 ms (in C++), meaning that the corrected average is 2 times faster.

---

[1] The sample was prepared by Adam Neuba. The complex cation contains two equivalent copper atoms in mixed nitrogen/sulfur environments and is a close representation of those classes of compounds for which the detector is planned for. Being stable in the air and having high solubility in different organic solvents makes it a very suitable test substance [NHFH12].

[2] Between 7.8 keV and 9.4 keV that encloses the CuKα and the scattering peaks.

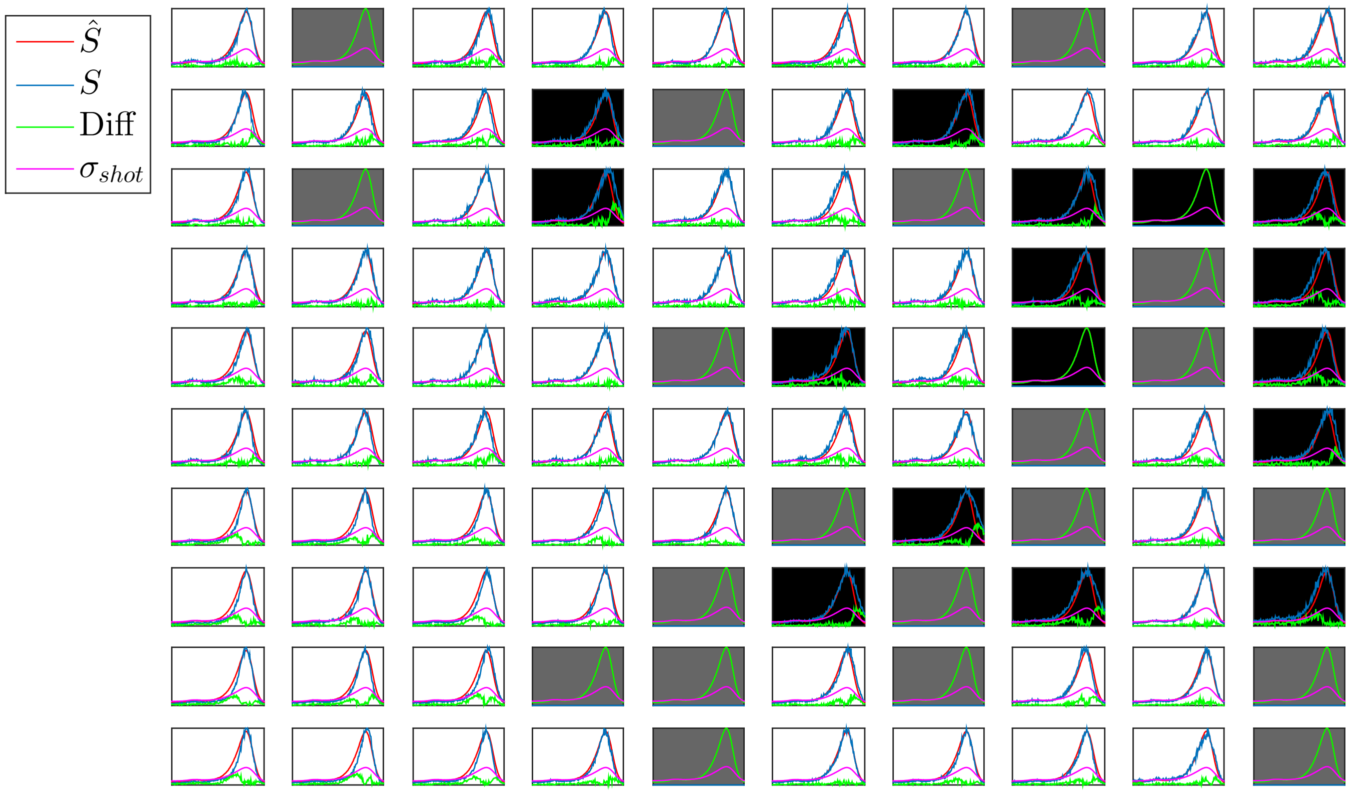

Figure 5.1: Comparison between the fluorescence spectrum of each detector pixel (blue) and the average spectrum (red), for the sample system$_1$ with 600 μmol/L of Cu, and at the incident energy of 8.98 keV. The difference Diff$_i$ is denoted in green and the shot noise σ_{SHOT} in magenta. The background color in black means that the pixel is rejected and in grey that the pixel is deactivated.

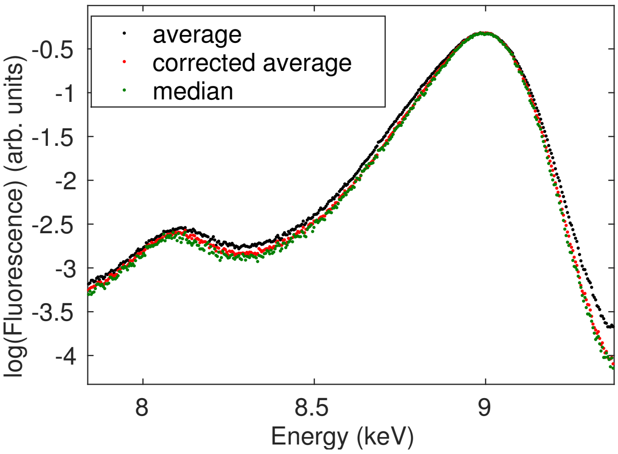

Figure 5.2: Comparison between the average spectrum over the 100 pixels, the corrected average spectrum by means of our method and the median spectrum for the sample system$_1$.

5.2 Integral of the fluorescence line of interest

Fluorescence spectra present two relevant features: (i) At low concentrations the fluorescence line of interest is considerably week compared to the scattering line; e.g. for a concentration of 600 μmol/L of Cu, the total number of counts within the CuKα line is about 8% of the total number. (ii) The scattering line presents an asymmetry due to incomplete charge collection effects, resulting in a long tail at lower energies. As a consequence of (i) and (ii), there is a large overlap of the scattering line and the line of interest at energies close to the absorption edge. This is shown in figure 5.3, which presents a fluorescence spectrum at an energy just above the K absorption edge of Cu.

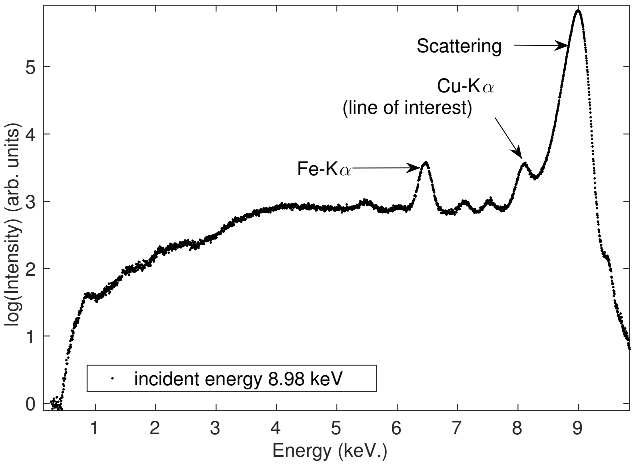

Figure 5.3: Fluorescence spectrum of the sample system$_1$ with 600 μmol/L of Cu, measured at an incident energy of 8.98 keV in beamline P11 with beam attenuation.

The goal is to extract the number of fluorescence counts that corresponds to the line of interest, in this case the CuKα. Nevertheless, the strong overlap of the scattering peak and the line of interest is to be considered in order to avoid as much as possible additional counts from the scattering peak. Therefore, the so called Region of Interest (ROI), where an area within certain limits of energy is extracted from the fluorescence spectra and integrated, would include counts from the the scattering tail near the absorption edge.

5.2.1 Fitting procedure

Aiming to extract the number of counts that come unikely from the line of interest, a fitting routine is proposed, where the integral under the peak of interest is calculated based on fitting parameters. With this method each point on the XAS spectrum corresponds to the area under the peak of interest calculated with the proposed fitting routine. The spectrum calculated by means of the fitting algorithm will be called Fitted Spectrum (FitSpec).
Fluorescence peaks can be fitted as Gaussian functions:

$$G(x) = A\exp\left\{\frac{-(x-\beta)^2}{2\sigma^2}\right\}, \tag{5.3}$$

where A is the amplitude, β is the mean value and σ^2 is the variance.
The integral of the gaussian function is $\sqrt{2\pi}A\sigma$, which gives the total number of counts under each peak. The FWHM of the gaussian ($2\sqrt{2\ln 2}\sigma$) is a constant value because the width of

each peak is determined by the intrinsic line width of the fluorescence lines ($\approx 5-10\,\mathrm{eV}$) and the energy resolution of the detector (for each energy[1]), which are both constant quantities. On the other hand, in XAS experiments the amplitude A of the peak of interest changes in accordance with the incident energy (below the absorption edge it is low, it grows during absorption, and oscillates in the XAFS region), meaning that in an automatic fitting routine A would be the fitting parameter and σ would be calculated according to the detector's resolution.

The background corresponds to extra fluorescence peaks, scattering, pile-up, etc. Fitting the complete spectrum is tricky and would add too many undesired fitting errors. Therefore, it is proposed here to select a region that includes the fluorescence line of interest and the scattering peak(s). By selecting this region, the fit describes the fluorescence line of interest, any extra fluorescence line and the scattering line. Each fluorescence line can be fitted as a Gaussian function, where the only fitting parameter is the amplitude of the line of interest. Furthermore, the scattering line presents a strong asymmetry that precludes to fit it as a Gaussian function. Nevertheless, this asymmetry is well described by means of the Exponentially Modified Gaussian Function (EMG) which is a convolution of a gaussian and an exponential function [NH], written as:

$$\mathrm{EMG}(x) = A_\mathrm{s} \int \exp\left\{ \frac{-(x-\beta_\mathrm{s}-x')^2}{2\sigma_\mathrm{s}^2} \right\} \cdot \exp\left\{ \frac{-x'}{t_0} \right\} dx' \tag{5.4}$$

where A_s is the amplitude, β_s the mean value of the gaussian component, σ_s^2 the variance of the gaussian components and t_0 is the constant of the exponential function. This model allows to fit the strong asymmetry of the scattering line by means of the parameter t_0.

The theoretical justification is that without detection losses the model is gaussian; nevertheless, the incomplete charge collection produces peaks with variable degrees of tailing described by the exponential function [NH]. Equation (5.4) can be transformed into a more handy version for fitting purposes, as:

$$\begin{aligned} \mathrm{EMG}(x) =& A_\mathrm{s} \exp\left[\frac{1}{2}\left(\frac{\sigma_\mathrm{s}}{t_0}\right)^2 + \frac{x-\beta_\mathrm{s}}{t_0} \right] \\ & \cdot \left[\mathrm{erf}\left(\frac{1}{\sqrt{2}} \left[\frac{\beta_\mathrm{s}}{\sigma_\mathrm{s}} + \frac{\sigma_\mathrm{s}}{t_0} \right] \right) + \mathrm{erf}\left(-\frac{x-\beta_\mathrm{s}}{\sqrt{2}\sigma_\mathrm{s}} - \frac{\sigma_\mathrm{s}}{\sqrt{2}t_0} \right) \right], \end{aligned} \tag{5.5}$$

---

[1] It is possible to measure this values previously for the main fluorescence peaks that are to be analyzed.

The final fitting model includes the Gaussian fit of the fluorescence peak of interest, the Gaussian fit of any extra fluorescence peak and the EMG fit of the scattering peak, as:

$$\mathrm{F}(x) = A \exp\left\{\frac{-(x-\beta)^2}{2\sigma^2}\right\} + \sum_i A_i \exp\left\{\frac{-(x-\beta_i)^2}{2\sigma_i^2}\right\} + \mathrm{EMG}(x) \tag{5.6}$$

The sub-index i accounts for any other fluorescence peak in the selected region.

Figure 5.4 shows the region of the peak of interest (CuKα) and the scattering peak, just above the absorption edge of Cu (8.98 keV). In this region, the fitting routine[1] employs a model that includes two gaussians for the CuKα and CuKβ peaks and one EMG for the scattering peak. At higher energies (9.99 keV), the fitting routine includes an extra gaussian, illustrated in figure 5.5, for the ZnKα peak. Zn is an impurity possibly present in the sample holder made of Al (containing all kind of impurities). Since the concentration of Cu is very low, its intensity is comparable to the trace elements in the sample holder. In this sense, low concentrated samples require significant clean environment.

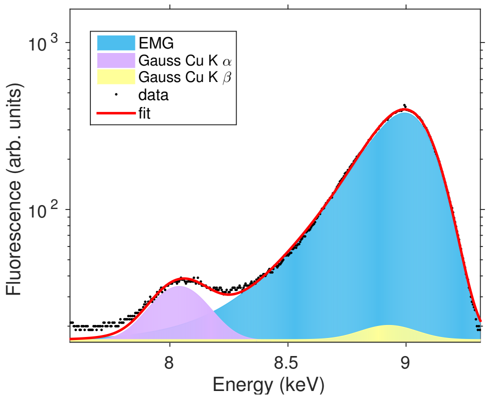

Figure 5.4: Fit of the emission spectrum at the incident energy of 8.98 keV for the sample system$_1$, in the region that encloses the CuKα and the scattering peaks.

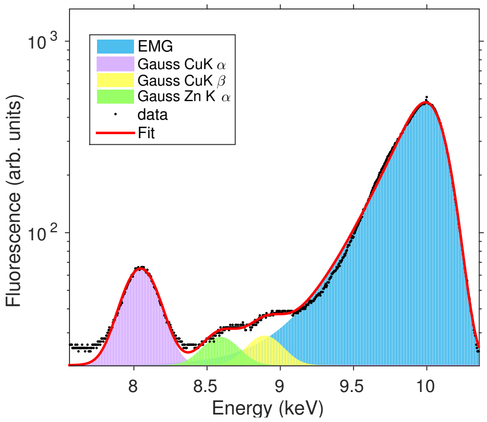

Figure 5.5: Fit of the emission spectrum at the incident energy of 9.99 keV for the sample system$_1$, in the region that encloses the CuKα and the scattering peaks.

Usually each point in the XAS spectrum measured with an energy dispersive detector corresponds to the integral of a ROI that we will call here Region of Interest Spectrum (ROISpec). Although the scattering line does not intersect directly with the CuKα line, it does contribute to the baseline of the CuKα peak. Figure 5.6 shows a contour plot map of incident energy vs.

---

[1] The fitting routine is developed in C/C++, employing the library *levmar* for custom fitting models.

fluorescence energy in the XANES region. There are 3 indicated ROI at 7.7 keV (marked by the black line) and end where the red, green and orange lines are (at 8.4 keV, 8.3 keV and 8.1 keV respectively). Figure 5.7a) shows the XANES ROISpec for each of these three ROI. In principle, the XANES spectra should be flat in the pre-edge region because the incident photon does not have sufficient energy to excite the K1s electron of Cu [TMN11]; nevertheless, the contribution of the scattering lines makes this region looking not flat depending on the selected ROI. On the opposite, the XANES FitSpec is almost flat in the pre-edge region and looks less noisy than any of the XANES ROISpec (see figure 5.7).

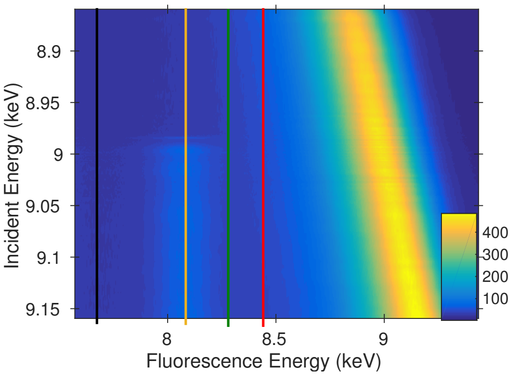

Figure 5.6: Contour plot of incident energy (in the XANES region of Cu) vs fluorescence energy (including only the region between the CuKα and the scattering) of the sample system$_1$. The vertical lines show the different ROI starting at 7.7keV (black) and ending at 8.4 keV (red), 8.3 keV (green) and 8.1 keV (orange).

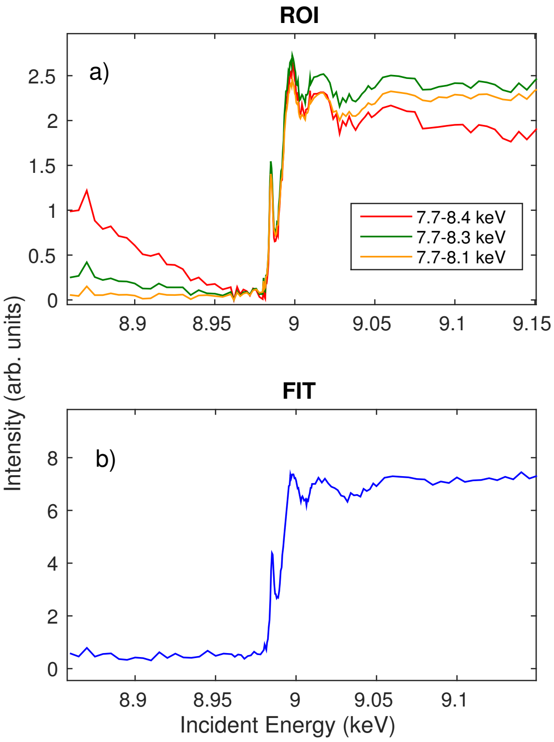

Figure 5.7: a) XANES ROISpec of Cu for each selected ROI (indicated in Figure 5.6). b) XANES FitSpec of Cu. Both for the sample system$_1$

5.3 XAS of ultra dilute samples at P64

In order to test the capabilities of the BioXAS setup at P64, samples of $CuSO_4$ in solution with 280, 2800 and 28000 μmol/L of Cu were employed. We measured XAS in fluorescence mode using the 100PixHPGe, placed 90° to the incident beam and 50 cm from the sample. The scans were done in continuous mode, with a measuring time per point of ~0.5 s, with $\Delta E \sim 1$ eV and in the energy range of 8.8 keV to 9.3 keV. With this experiment the performance of the detector with samples at different concentrations was tested. Moreover, a comparison of the FitSpec (see figure 5.8), with the ROISpec (see figure 5.9) was done.

These measurements allow to get an estimate of the quality of the XANES spectra depending on the concentration of the element of interest. In this case the sample is an ideal one because it does not contain impurities that affect the spectra. Furthermore, from a comparison between the two methods (FitSpec and ROISpec) one notices that for concentrations of 2800 μmol/L or higher both methods are equivalent. Nevertheless, for lower concentrations, e.g. 280 μmol/L, the ROISpec shows a strong contamination of the scattering line, reflected in a negative slope before and after the edge. This is because the position of the scattering line is shifting away from the CuKα with the increment of the incident energy. As a consequence, the FitSpec (without the strong contamination from the scattering line) shows an improvement of the signal-to-background ratio compared to the ROISpec.

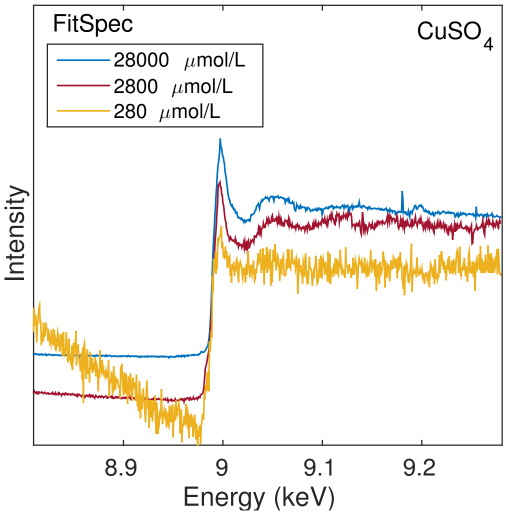

Figure 5.8: XANES FitSpec of Cu. The sample was a solution of $CuOS_4$ with 280, 2800 and 28000 μmol/L of Cu.

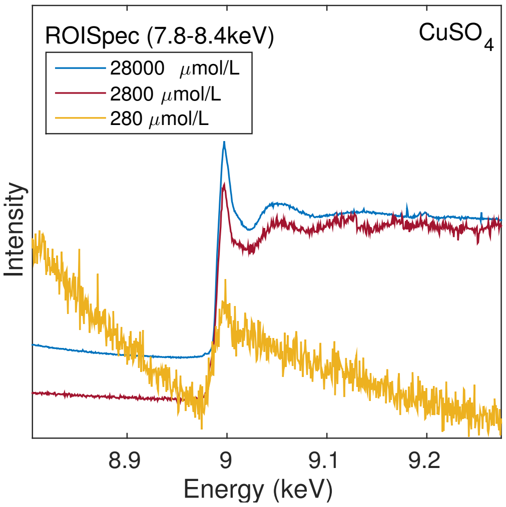

Figure 5.9: XANES ROISpec of Cu for the ROI between 7.8-8.4 keV. The sample was a water solution of $CuSO_4$ with 280, 2800 and 28000 μmol/L of Cu.

The red curves present a step at 9.13 keV and the blue curves present spikes at 9.19 keV and 9.25 keV. This features are also present in standard XAS (in transmission mode for solid samples) and are attributed to the vibrations in the monochromator due to its cooling water system as well as instabilities of the machine.

In order to explore concentrations between 280 and 2800 μmol/L as well as the effect of pollutants in the sample, a solution of $CuOS_4$+$NiCl_2$ with 312 μmol/L of Cu and 336 μmol/L of Ni was employed to measure the K Cu absorption edge. Ni was chosen because the K Ni absorption edge is at a lower energy than the K Cu absorption edge allowing to excite Ni when measuring the absorption of Cu. Moreover, the NiKβ line is between the CuKα and CuKβ. This is a way of testing the method of FitSpec for impurities that are overlapped with the line of interest.

A Z-1 filter of Ni was placed between sample and detector in order to absorb most of the scattering peak, while transmitting most of the Cu Kα [1]. This filter is ideal to improve the signal-to noise ratio for ultra dilute samples, where the ratio between the scattering and the fluorescence line of interest is too high [New04]. The measurements were done in continuous mode, with

---

[1] Ni has an absorption edge at 8.3 keV, between the CuKα (at 8 keV) and the CuKβ (at 8.9 keV). Thus, using Ni as a filter for Cu would result in the absorption of the slightly higher energy 8.9 keV x-rays, while letting the 8 keV rays through without a significant decrease in intensity.

$\sim$0.5 s exposure time per point and were repeated 3 times for better statistics. Figure 5.10 shows the FitSpec and the ROISpec. Results exhibit better quality in terms of signal-to-noise ratio for the FitSpec.

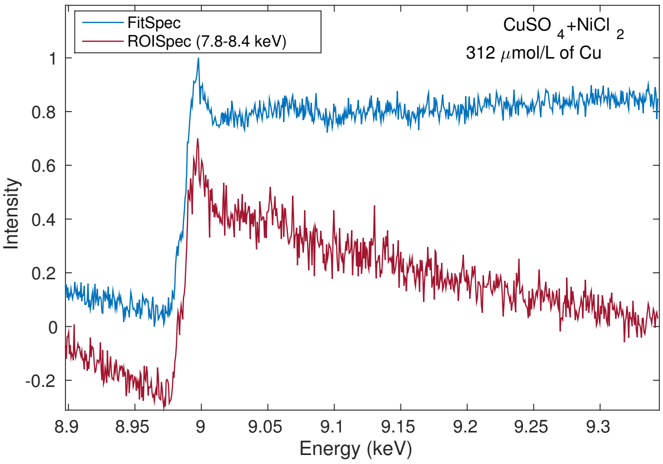

Figure 5.10: XANES ROISpec and FitSpec of Cu. The sample was an aqueous solution of $CuOS_4$+$NiCl_2$ with 312 μmol/L of Cu and 336 μmol/L of Ni.

5.4 Data reduction at higher energies

The data reduction procedure explained above is valid at low absorption energies ($\leq$10 keV) where the scattering lines (coherent and incoherent) are not separated. At these energies the effect of the scattering angle θ, described in equation (4.1), is only broadening the scattering peak slightly depending on the detector column of the pixel (see figures 4.3 and 4.4). On the contrary, for higher absorption energies e.g. Mo (20 keV) the incoherent scattering peak is separated from the coherent one (see figure 4.5). In these cases, special attention should be payed to the angular dependence of the incoherent scattering peak.

To study this behavior, an aluminum sample has been used to measure fluorescence with the 100PixHPGe with an incident energy of 20.15 keV. The detector was placed 50 cm from the sample and at 90° to the incident beam. At this distance the angular difference between the columns at both extremes of the detector is around 5.2°. Figure 5.11 shows the average spectra in the region of the scattering peaks for each column of the detector [3](with the set up

---

[3] column 1 contains pixels 1 to 10, column 2 contains pixels 11 to 20 and so on.

configuration explained in figure 4.1).

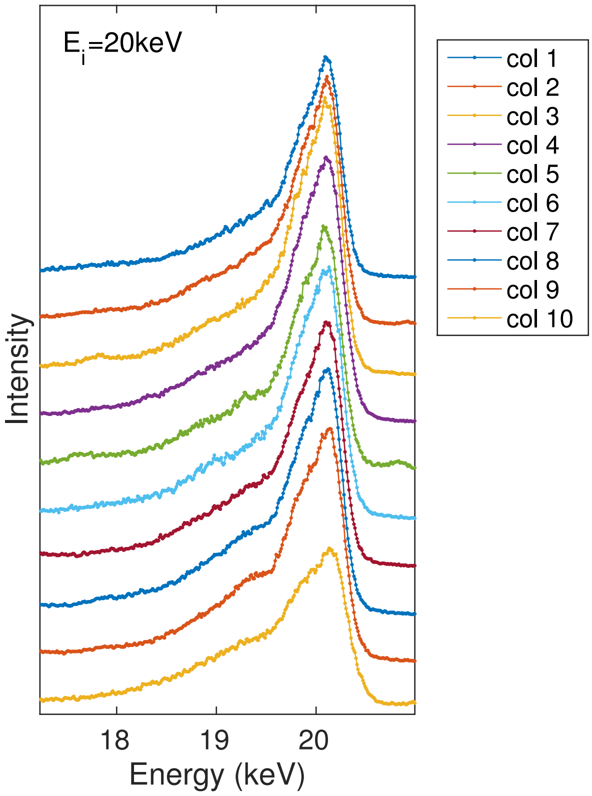

Figure 5.11: Column dependency of the scattering peaks at the incident energy of 20.15 keV in the 100PixHPGe. The curves are vertically shifted for better visualization.

Due to the column dependency on the scattering peaks' shape, it is more accurate to perform the data reduction per column. In this way the mean spectrum is calculated per column and compared to each spectrum on the same column in order to eliminate outliers. Then, the mean spectrum per column is fitted with a model that includes an EMG (see equation 5.5) for each scattering peak (inelastic and elastic):

$$\mathrm{F}(x) = \mathrm{EMG}_{\mathrm{inelastic}}(x) + \mathrm{EMG}_{\mathrm{elastic}}(x) \tag{5.7}$$

Figures 5.12 and 5.13 show the fit of the spectrum in the region of the scattering peaks for the column 1 and 10 respectively.

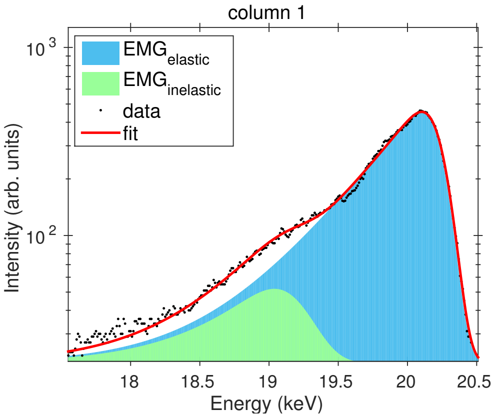

Figure 5.12: Fitted data of an Al sample, for the column 1 at an incident energy of 20 keV.

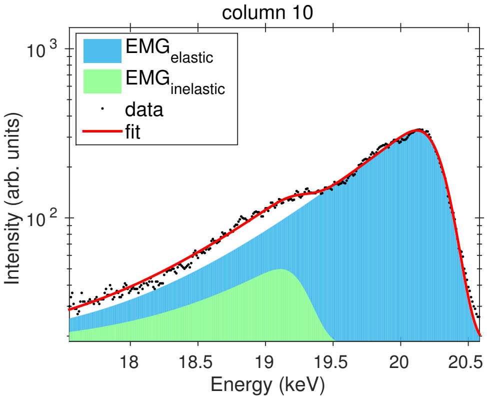

Figure 5.13: Fitted data of an Al sample, for the column 10 at an incident energy of 20 keV.

5.5 De-noised data compression

Ideally a user would like to have access to the raw data to check for possible errors in the reduction procedure. The raw data are a 3D matrix $[\mathbf{X}]_{n\times m\times N}$ that should be stored for each XAS scan. This can constitute a large amount of memory that should be reduced by a lossy method to reduce the noise. Principal Component Analysis (PCA) allows to reduce the original data set with a minimum information loss by retaining only the first most representative principal components of the data.

The data at a fixed incident energy l can be expressed in terms of the first r principal components (for further details on the component selection see chapter 6.3), as:

$$[\mathbf{X}_l]_{N\times m} = [\mathbf{C}]_{N\times r}[\mathbf{P}]_{r\times m}, \tag{5.8}$$

where $[\mathbf{X}_l]$ is the data matrix at an incident energy l, $[\mathbf{P}]$ is the truncated PCA matrix and $[\mathbf{C}]$ is the coefficient matrix.

In order to find the matrix $[\mathbf{C}]$, it is enough to solve a least squares fit by minimizing the residual between the data and the representation in terms of the basis $[\mathbf{P}]$. In this context the coefficient matrix is found to be a linear transformation of the data [RS10] as:

$$[\mathbf{C}] = [\mathbf{X}_l][\mathbf{P}']([\mathbf{P}][\mathbf{P}'])^{-1}, \tag{5.9}$$

with $\mathbf{P}'$ being the transposed of $\mathbf{P}$.
Only the coefficient matrix plus the selected r principal components are to be transferred per incident energy, meaning that the new data set to be transferred is of size $l \times [(N \times r) + (r \times m)]$.

For the data set under consideration this makes a reduction of $\sim 51 \times 10^6$ to $\sim 5 \times 10^6$ data points, with $r = 7$. In this case only $\sim 8\%$ of the original data points should be transferred and saved and the user could still have access to a denoised raw fluorescence (truncated) data set employing equation (5.8) (see Figure 5.14).

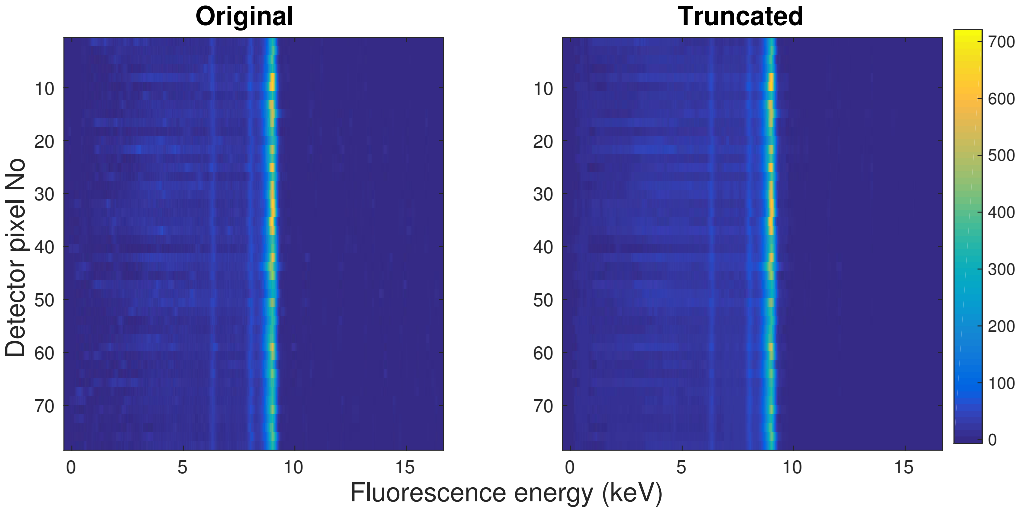

Figure 5.14: Fluorescence spectra of each detector pixel at an incident energy of 9.03 keV. At the left the original image and at the right the truncated data with the first 7 selected principal components.

The difference between the original data and the truncated data expressed in terms of the first 7 components is illustrated in figure 5.15. The difference is slightly bigger than the shot noise[1] (illustrated in figure 5.16) due to extra noise contributions e.g. electronic noise, fano noise and pattern noise.

---

[1] The shot noise is calculated for each point in the spectrum according to equation 5.2.

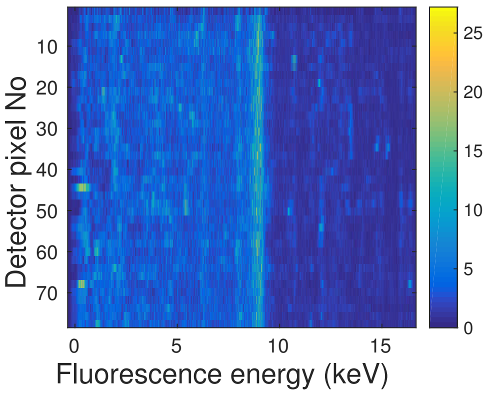

Figure 5.15: Difference between the original and the truncated data

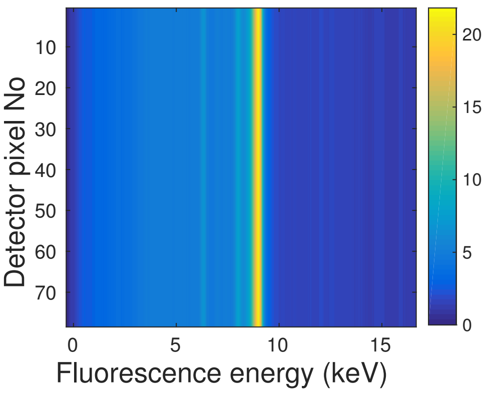

Figure 5.16: Shot noise for each detector pixel.

6

X-ray fluorescence mapping experiments on palimpsests

Palimpsests are manuscript pages that contain one or more than one overwritten text. Usually, they are parchments (material made from animal skin) that due to the high costs and durability were reused several times. The scribes removed mechanically or chemically the ink and wrote on top a new text, repeating this process in some cases several times [BW93].

The palimpsest parchments were often written with iron gall inks. These inks are the most important in the western history, being used by the Romans and widely used after the middle ages [HMKB04]. Typically, iron gall inks are produced with galls, vitriol, gum Arabic as a binding media and an aqueous medium such as wine, beer or vinegar. Vitriol was obtained from different mines and by various techniques. Therefore, the iron sulfate was contaminated to varying extents with many other metals such as Cu, Al, Zn and Mn, which do not contribute to color formation in the ink solution [HMKB04].

The method of mechanical erasing consisted of scraping the parchment until the ink was not visible. This process is very efficient and in most cases the text is unrecoverable. However, when the erasing process was done chemically (e.g. by adding some acid substance) the text became invisible[1] but most of the metals contained in the ink remained on the parchment.

By means of XRF it has become possible to visualize these texts that are invisible to the human eye [Ber11]. When an incident x-ray has the energy of at least the highest binding energy of the elements present in the parchment, excitations of the core electrons take place. These

---

[1] "By removing the gallic acid from the organo-metallic compound responsible for the ink's bluish-black color, the remaining ink was rendered more or less transparent to visible light." [GD14]

excitations are followed by Auger decays or photon emission (e.g. fluorescence), with energies characterizing each of the elements as a finger print. In this way a fluorescence spectrum is built up by histogramming the energy of the emitted photons.

6.1 Experimental setup

The experiment consists on scanning a parchment with x-rays and collecting the fluorescence spectrum at different points on the specimen. For this purpose, the parchment is mounted on a stage that has freedom of movement in the vertical and in the horizontal direction. The stage was fixed while the x-rays impinge on one point of the parchment and the fluorescence signal was collected by a detector that was placed at 90° to the incident beam and at 45° to the stage (see figure 6.1). Then, the stage moved in the horizontal direction, so that a different point of the parchment could be probed by the x-rays. The stage moved in the vertical direction when the information from the complete horizontal line was collected, making a complete scan of the parchment. The length of the stage steps as well as the beam size determine the spatial resolution of the scanned parchment.

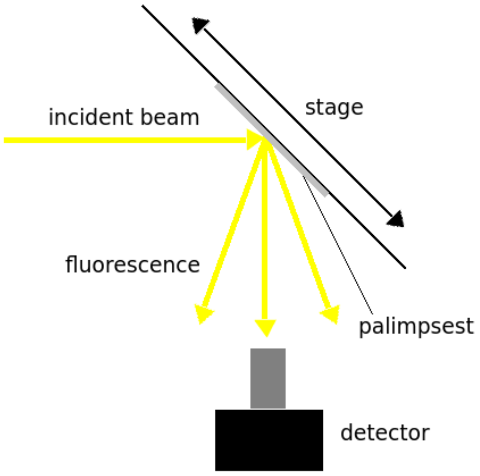

Figure 6.1: Experimental setup of XRF mapping experiments on palimpsests.

The detector collects the fluorescence at each point of the parchment and builds a histogram of photon energies. This histogram is known as the fluorescence spectrum, that gives information about the elemental composition of this segment of parchment. The data set will contain one spectrum per each scanned point on the parchment. If we consider the vertical and the horizontal dimensions of the scan, plus the collected spectra, the final data set is 3D.

6.2 Automatic method of text separation

Here, a method that separates the texts automatically is presented. For this purpose, each spectrum is considered as a vector. The method assumes every spectrum to be a linear combination of spectra of each ink plus a background. This assumption means that the basis vectors correspond to the spectra of inks and background, which we will call the *true basis.* The first goal is to construct a basis that is very similar to the true basis and the final goal is to decompose the data in terms of each of the basis vectors so that the texts are as separated as possible and the readability is increased.

6.2.1 Data representation

The sample parchment is scanned, so that a 3D data arrangement is obtained. There are x rows and y columns that make a total of $n = x \cdot y$ spectra, each of size m.
Intuitively, one can consider each of the fluorescence spectra as a combination of spectra of each ink plus a background [SI89]. Thus, a spectrum, represented as a vector, can be described as a linear combination of several spectra of ink vectors (including a background) as:

$$\vec{X}_i \approx \sum_{j}^{r} \left[c_{ij} \vec{V}_j \right] , \tag{6.1}$$

where
$\vec{X}_i \in \mathbb{R}^m$: spectrum vector i,
$\vec{V}_j \in \mathbb{R}^m$: spectrum of the ink vector j,
c_{ij}: coefficients of the linear combination,
m: the number of channels in the spectrum,
$i \in \mathbb{N}$, $i \leq n$ (index for a spectrum),
$j \in \mathbb{N}$, $j \leq r$ (index for the different inks present and background),
n: the number of spectra,

r: the number of inks plus background.

In this representation $\vec{X}_i \in \mathbb{R}^m$ is the spectrum i of the data set. $\vec{V}_j \in \mathbb{R}^m$ is a spectrum of one ink or the background. The coefficients c_{ij} of the linear combination contain the information about the amount of each ink and background in the spectrum i.
The data can be also expressed as a matrix $\mathbf{X} \in \mathbb{R}^{n\times m}$ with the spectra $\vec{X}_i$ located in its rows, so that the linear combination of spectral ink vectors expressed in equation (6.1) is written in terms of matrix multiplication as,

$$\begin{pmatrix} \vec{X}_1 \\ \vec{X}_2 \\ \vdots \\ \vec{X}_n \end{pmatrix} \approx \begin{pmatrix} c_{1,1} & \cdots & c_{1,r} \\ c_{2,1} & \cdots & c_{2,r} \\ \vdots & \ddots & \vdots \\ c_{n,1} & \cdots & c_{n,r} \end{pmatrix} \begin{pmatrix} \vec{V}_1 \\ \vec{V}_2 \\ \vdots \\ \vec{V}_r \end{pmatrix}$$

$$\mathbf{X} \approx \mathbf{CV}, \tag{6.2}$$

where $\mathbf{C} \in \mathbb{R}^{n\times r}$ is the coefficient matrix and $\mathbf{V} \in \mathbb{R}^{r\times m}$ is the basis matrix with basis vectors $\vec{V}_j$ located in its rows.

6.2.2 Decomposed images

The column vectors $\vec{C}_j \in \mathbb{R}^n$ of the coefficient matrix $\mathbf{C}$ are the decomposition of the data in terms of the basis vectors $\vec{V}_j$. The vectors $\vec{C}_j$ of size n are to be sorted in a 2D arrangement in order to recover the original palimpsest dimensions $x \times y$. Once knowing the ink basis, the vectors $\vec{C}_j$ will allow the visualization of different texts. From now on, we will call the decomposition of the data in terms of the basis vectors $\vec{C}_j$ *the decomposed images.*

Equation (6.1) implies that:

$$\begin{aligned} \vec{X}_1 &= c_{1,1}\vec{V}_1 + c_{1,2}\vec{V}_2 + \ldots c_{1,r}\vec{V}_r \\ \vec{X}_2 &= c_{2,1}\vec{V}_1 + c_{2,2}\vec{V}_2 + \ldots c_{2,r}\vec{V}_r \\ &\vdots \\ \vec{X}_n &= c_{n,1}\vec{V}_1 + c_{n,2}\vec{V}_2 + \ldots c_{n,r}\vec{V}_r \quad . \end{aligned} \tag{6.3}$$

The first equation of (6.3) can be written as:

$$\left[x_1^1 x_1^2 \ldots x_1^m\right] = c_{1,1}\left[v_1^1 v_1^2 \ldots v_1^m\right] + c_{1,2}\left[v_2^1 v_2^2 \ldots v_2^m\right] \ldots + c_{1,r}\left[v_r^1 v_r^2 \ldots v_r^m\right] \tag{6.4}$$

where the notation x_i^l denotes the entry l of the vector $\vec{X}_i$ and v_i^o denotes the entry o of the vector $\vec{V}_i$.

Thus,

$$\begin{aligned}
&x_1^1 = c_{1,1}v_1^1 + c_{1,2}v_2^1 + \dots c_{1,r}v_r^1 \\
&x_1^2 = c_{1,1}v_1^2 + c_{1,2}v_2^2 + \dots c_{1,r}v_r^2 \\
&\vdots \\
&x_1^m = c_{1,1}v_1^m + c_{1,2}v_2^m + \dots c_{1,r}v_r^m .
\end{aligned} \tag{6.5}$$

The system of linear equations in (6.5) has m equations and r unknowns. Those are in general *overdetermined systems* with more equations $m \approx 2048$ than unknowns $r \approx 3$. For every equation on (6.3) there is a system of linear equations to solve, like the one in (6.5).

In general knowing the basis vectors $\vec{V}_j$ and the data system composed by the spectral vectors $\vec{X}_i$, it is possible to obtain the coefficients in $\mathbf{C}$ by solving n sets of linear equations like:

$$\begin{aligned}
&x_i^1 = c_{i,1}v_1^1 + c_{i,2}v_2^1 + \dots c_{i,r}v_r^1 \\
&x_i^2 = c_{i,1}v_1^2 + c_{i,2}v_2^2 + \dots c_{i,r}v_r^2 \\
&\vdots \\
&x_i^m = c_{i,1}v_1^m + c_{i,2}v_2^m + \dots c_{i,r}v_r^m .
\end{aligned} \tag{6.6}$$

These overdetermined systems have been found, for our case, to have some (approximately) linearly dependent equations, leaving only r independent equations. This implies that the systems were always numerically solvable.

Another way of finding the matrix $\mathbf{C}$, is to solve a least squares fit by minimizing the residual between the data and the representation in terms of the basis $\mathbf{V}$. In this context the coefficient matrix is found to be a linear transformation of the data [RS10] as:

$$\mathbf{C} = \mathbf{X}(\mathbf{V}'\mathbf{V})^{-\mathbf{1}}\mathbf{V}', \tag{6.7}$$

where $\mathbf{V}'$ represents the transposed matrix of $\mathbf{V}$.

In order to find the decomposed images it is necessary to create a basis of the system that is as close as possible to the ink basis or *true basis*.

6.2.3 Principal Component Analysis

PCA yields an orthonormal basis of the data set. The basis vectors are the eigenvectors of the covariance matrix of the data ($\mathbf{XX}'$) sorted by their correspondent eigenvalue, meaning that the first basis vectors have the biggest eigenvalues and contain most of the information of the system [Jol05].

PCA allows a dimensional reduction of the problem by selecting the first few eigenvectors that represent the main features of the system. This reduction is possible since most of the eigenvectors only add noise to the data or are not representative.

The principal components can be obtained by employing the Singular Value Decomposition (SVD) technique [GR69]. This method factorizes a matrix in terms of three matrices $\mathbf{U}$, $\mathbf{S}$ and $\mathbf{P}'$, where $\mathbf{U}$ is a $n \times n$ unitary matrix, $\mathbf{S}$ is a $n \times m$ diagonal matrix with non-negative real numbers on the diagonal, and $\mathbf{P}'$ the $m \times m$ unitary matrix denoting the transpose of the unitary matrix $\mathbf{P}$. The advantage of SVD is that the non-zero diagonal values of $\mathbf{S}$ are the square roots of the eigenvalues of the covariance matrix of the data $\mathbf{XX}'$ and the columns of $\mathbf{P}$ are the eigenvectors of $\mathbf{XX}'$. This fact makes SVD an ideal method to perform PCA[1].

The data can be then approximated in terms of the selected eigenvectors as:

$$\vec{X}_i \approx \sum_{j}^{k} d_{ij} \vec{P}_j, \tag{6.8}$$

where

$\vec{X}_i \in \mathbb{R}^m$: spectrum vector i,

$\vec{P}_j \in \mathbb{R}^m$: eigenvector j,

d_{ij}: coefficients of the linear combination,

m: the number of entries in the spectrum,

n: the number of spectra,

k: the number of selected eigenvectors,

$i \in \mathbb{N}$, $i \leq n$,

$j \in \mathbb{N}$, $j \leq r$

Equation (6.8) has its matrix representation as:

$$\mathbf{X} \approx \mathbf{DP}, \tag{6.9}$$

---

[1] SVD solves a problem from the linear algebra with no additional purpose than a specific matrix factorization. However, SVD has been found useful to solve other problems with potential applicability e.g. PCA. There are existing libraries for C/C++ and Matlab that employ SVD to solve PCA.

where $\mathbf{X} \in \mathbb{R}^{n \times m}$ is the data matrix, $\mathbf{D} \in \mathbb{R}^{n \times k}$ is the coefficient matrix and $\mathbf{P} \in \mathbb{R}^{r \times m}$ the PCA basis matrix.

PCA grants the basis $\mathbf{P}$ and the matrix $\mathbf{D}$ contains in its rows the projections onto each of the basis vectors. The row vectors of $\mathbf{D}$ of size n are sorted in a 2D array $x \times y$ to recover the palimpsest dimensions. These arrays are called *the projected images*[4].

The basis that is found through PCA can have negative entries due to the orthogonality. In this sense, the basis vectors do not necessarily have a physical meaning since they should represent fluorescence spectra (non-negative values). A consequence of this is that the projected images sometimes do not allow to visualize the independent texts because the basis $\mathbf{P}$ is not close enough to the true basis $\mathbf{V}$.

6.2.4 Optimization problem

In order to find the transformation matrix $\mathbf{T}$ without any user intervention, it is necessary to find out which feature makes the texts in the decomposed images as discerned as possible. Handwritings do not have an uniform intensity for each individual text but it depends on the pressure by which the hand pressed on the parchment; therefore, there is not only one value of intensity for each text. In the ideal case of completely discerned texts there will be only two main intensity ranges, one for the region with text and one for the region without text[1]. Based on the previous information the number of intermediate values of intensity in the decomposed images should be decreased.

With this aim, it is proposed in this thesis to minimize a cost function F_j, that calculates the minimum distance from each entry to the maximum or minimum entry of the decomposed image $\vec{C}_j$ and sums up these values. When this function reaches a minimum, the image has almost only two values of intensity:

$$F_j = \sum_{l}^{n} min \left\{ |C_{j,l} - max(\vec{C}_j)|, |C_{j,l} - min(\vec{C}_j)| \right\} \tag{6.10}$$

---

[4] also known as *eigenimages*

[1] The method is design to separate two overlapped texts; however, it has shown also good results for three overlapped patterns (see section 6.3 “second palimpsest”).

where the notation $C_{j,l}$ denotes the entry l of the vector $\vec{C}_j$.

As we seek a fluorescence spectral basis, it is desirable to restrict the problem to basis vectors with non-negative entries. Therefore, the problem can be reformulated by including a penalty to the cost function, defined as:

$$\text{PEN}_j = \sum_{l}^{n} \min\{0, C_{j,l}\}^2, \tag{6.11}$$

The final cost function can be described as a combination of the cost function in equation (6.11) and the penalty function:

$$\tilde{F}_j = F_j + \sigma \text{PEN}_j, \tag{6.12}$$

where σ is a coefficient that weights the positivity in the cost function. This coefficient is chosen to be such that F_j and σPEN_j are comparable.

The optimization routine starts at $\mathbf{T_0}$, that we choose to be the identity matrix of dimension k, $\mathbf{I_k}$. This means that the initial basis corresponds to the truncated $(k \times m)$ PCA basis. From the new matrix $\mathbf{V}$ the decomposed images $\vec{C}_j$ are calculated and the cost function defined in equation (6.12) is evaluated. A minimum is found by employing the Levenberg-Marquardt (L-M) algorithm [Gav13, EH88]. A simplified scheme of the optimization routine is summarized as:

Step 1. Initialize the transformation matrix as $\mathbf{T} = \mathbf{I_r}$

Step 2. Calculate the new basis as $\mathbf{V}$=$\mathbf{TP}$

Step 4. Find the decomposed images $\vec{C}_j$ with equation (6.7)

Step 5. Evaluate the cost function in equation (6.12)

Step 6. Update $\mathbf{T}$ in the direction that F decreases (this direction is determined by means of the L-M algorithm [Gav13, EH88]) and repeat step 2 or finish if a minimum is found

6.3 Results on original palimpsests

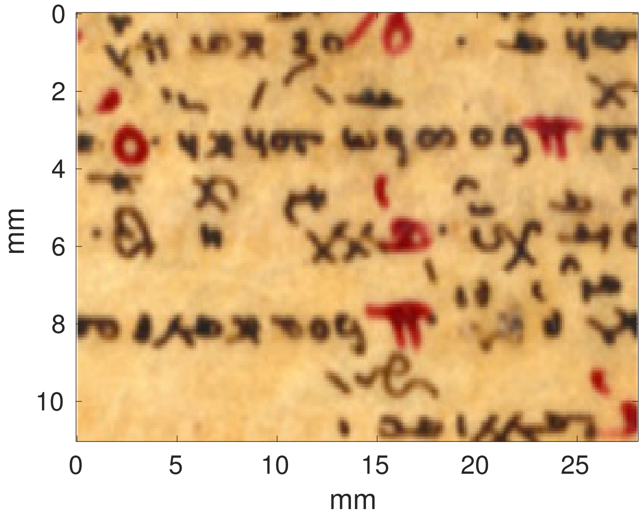

Figure 6.2: Photo of a segment of one leave from the 12^{th} century Menologion (Cod. Lips. Rep. I 62, f. 17). All rights attributed to Universitätsbibliothek Leipzig.

A segment from a leaf that forms part of a 12^{th} century Menologion (a Greek orthodox monthly service text) was investigated within the scope of the cooperation between the project "Teuchos. Zentrum für Handschriften- und Textforschung (Universität Hamburg)" and the DESY [1](figure 6.2). The Menologion contains palimpsest leaves from several original manuscripts that predate the new one by approximately half a century. The leaf that was examined (f. 17) contains part of the Capita de caritate of Maximus Confessor as the under-text.

The leaf was analyzed with XRF at DORIS beamline L (DESY) [DG10] with an incident photon energy of 18 keV, using a Vortex-EM detector [vor][DG10]. The palimpsest was mapped with the x-ray beam and the fluorescence spectra per point were recorded with a resolution of 70 μm horizontally and 100 μm vertically and with a data acquisition rate of 7 spectra/s with 150 μm step width in continuous scanning mode. Figure 6.3 shows an average spectrum and the main fluorescence transitions of a segment of 155 × 281 pixels. The spectrum shows peaks at the fluorescence energies of: Ar, K, Ca, Mn, Fe, Cu, Zn, Pb and Hg principally. As was already mentioned before, the iron gall ink is expected to have Fe plus some impurities of Cu Zn and

---

[1] Experiment performed by Daniel Deckers and Leif Glaser.

Mn. The traces of Pb together with Hg are known to be present in red inks that were used in some cases to mark capital letters. Ca might have been used to whiten the parchment. Finally, the interaction of x-rays and air lead to excitation of Ar that is also present in the spectrum.

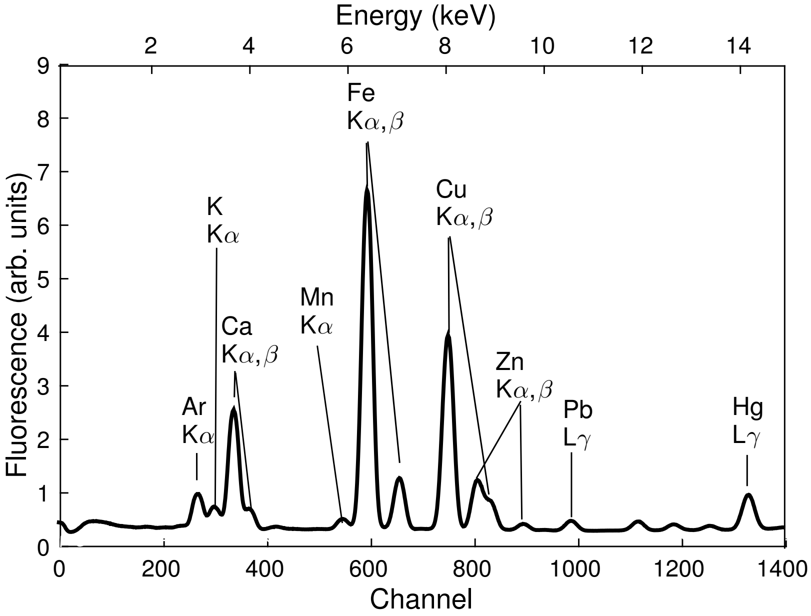

Figure 6.3: Averaged fluorescence spectrum of the data taken from one of the leaves from the 12^{th} century Menologion (Cod. Lips. Rep. I 62, f. 17).

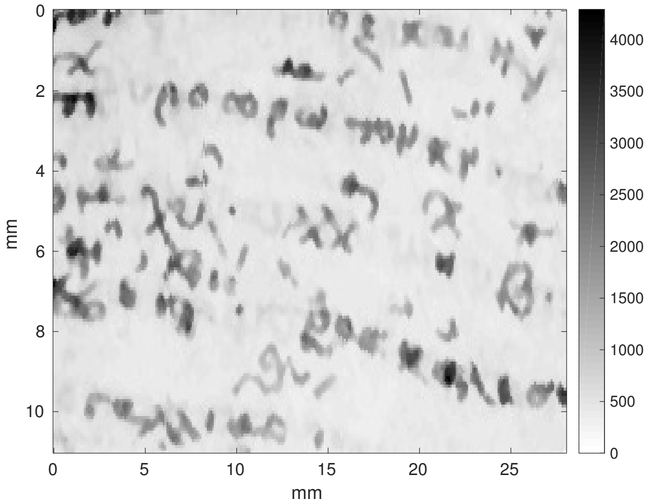

Figure 6.4: Total fluorescence of a segment of one leave from the 12^{th} century Menologion (Cod. Lips. Rep. I 62, f. 17).

Although, parts of the text present in the parchment might be visible by total XRF (figure 6.4), in which the spectrum intensity is integrated over all energies, the intensity ratio between two inks can be so high that some texts are not visualized at all. Furthermore, even in the case that the texts are visualized, the superposition of them decreases dramatically the readability. In order to overcome this drawback one can analyze the so called *elemental maps* of the fluorescence picture, which are 2D plots which show only the counts corresponding to one specific element in the spectrum [DG10]. The main peaks where selected and are visualized in figure 6.5. The most representative maps are the ones of Ca and Cu showing different texts independently. Moreover, the Mn map shows the two texts completely superimposed, both at the same intensities around 100. The iron map, on the other hand, is very similar to the total fluorescence map (figure 6.4). A direct conclusion from this analysis is that one of the texts contain mainly Ca, while the second one does not. This feature makes it possible to distinguish the texts through elemental maps. The map of K is also relevant, it shows some few signs at a intensity of 40, which seem to be also present in the elemental map of Cu. Finally, this approach will lead to a better readability when the different inks contain at least one unique element.

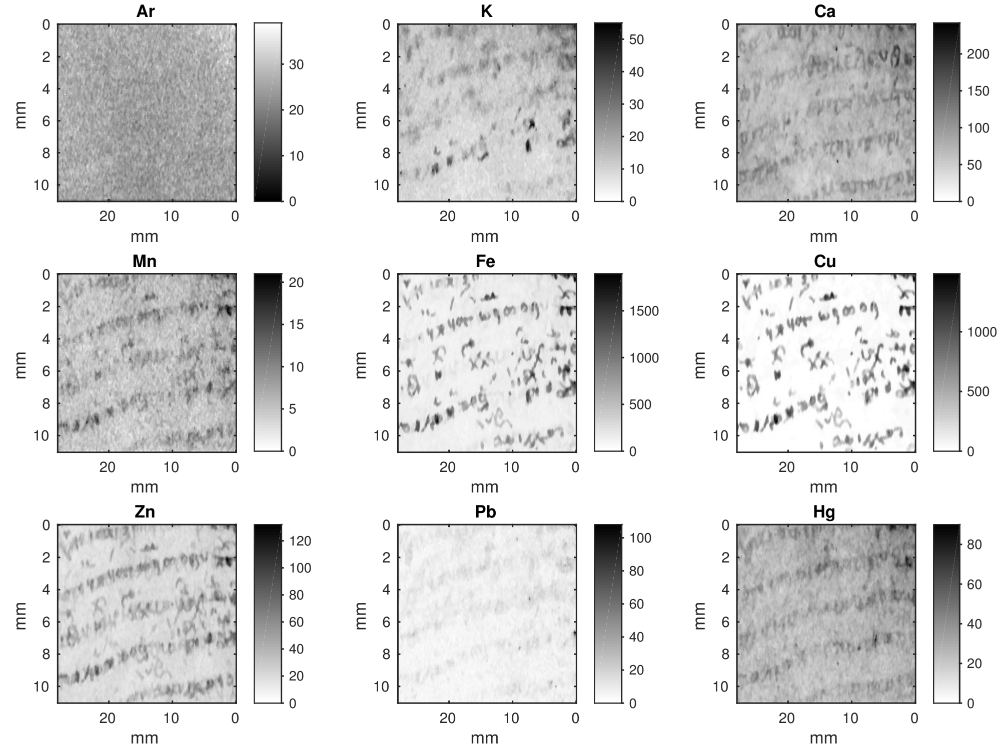

Figure 6.5: Elemental maps of a segment of one sheet from the 12^{th} century menologium (Cod. Lips. Rep. I 62, f. 17).

The elemental map approach requires user intervention and can be time consuming. Therefore, we employ the automatic method of text separation presented in section6.2 to study the segment of the 12^{th} century Menologion. For this purpose, the SVD routine implemented in MATLAB [MAT14] is used to obtain the principal components on the palimpsest segment of the 12^{th} century Menologion. Figure 6.6 shows the eigenvalues sorted from the biggest to the lowest up to the 50^{th} value. From the 4^{th} eigenvalue on the difference between consecutive values is very small compared to the differences between the first 3 values. Therefore, we can conclude that in this case the first 3 principal components are significant and from the 4^{th} component on there is mainly noise added to the system. This selection is made automatically by fitting linearly the plot of log(eigenvalue) vs. sorting position. The eigenvalues that are not important follow a linear behavior, while the first values that are important are outside this behavior. We check the linear fit starting from the eigenvalue under consideration. If the fit is good, then this eigenvalue should not be taken into account, but if it is not it means that it is outside this linear behavior and that is a relevant one. To make it automatic we consider the coefficient of determination of the fit R^2 (ranges from 0–1, where 1 is the perfect fit). If R^2 is below 0.9, the eigenvalue is taken into account. In this case the number of selected components is 3.

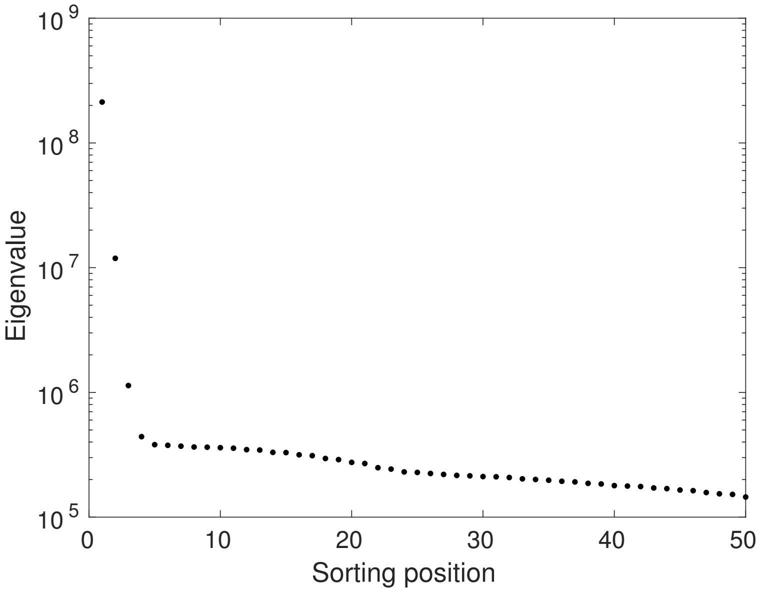

Figure 6.6: First 50 eigenvalues of the data taken from the 12^{th} century Menologion (Cod. Lips. Rep. I 62, f. 17).

Figure 6.7 shows the first 3 principal components or eigenvectors of the covariance matrix of the data. Since we employ SVD to calculate PCA, the average spectrum is not subtracted from the data, making the first component being approximately the average spectrum. As a consequence this method will always work with one extra component (the average). For instance, in the given case there are 2 superimposed texts but 3 principal components.

Once having the truncated PCA basis, the projected images can be calculated with equation (6.9) as the matrix **D**. Figure 6.8 shows the first three projected images. Since the first component is approximately the average spectrum, the first projected image is the mean image which in this case shows a horizontal text with an intensity much higher that the rest of the texts in the palimpsest. The second projected image shows again the same text with positive intensities (bright) plus a second text with negative intensities (dark). The third projected image does not show any discerned text. One can see that PCA gives as a result a mixture of inks.

This example shows that the PCA basis is not always ideal because it does not enable to visualize different texts in separated images, due to basis vectors containing negative entries. Although the basis provided by PCA does not give an answer to the problem, it gives a starting point for the *true basis search.* An appropriate linear combination of the column vectors of **P** would lead to a positive basis of the system. In order to find an automatic approach we state the problem in general terms. The main goal is to change the basis **P** through a matrix transformation $\mathbf{T} \in \mathbb{R}^{r \times r}$ such that the new basis matrix $\mathbf{V} \in \mathbb{R}^{r \times m}$ is non-negative and that the decomposed images are as discerned as possible. The problem has been reformulated to find $r \times r$ parameters in the transformation matrix **T** that satisfies those conditions (see section 6.2.4).

We have employed the L-M [Gav13] method to transform the PCA basis by minimizing the cost function in equation (6.12). This method required 11 iterations to converge to a minimum for the analyzed data set.

The optimization routine yields basis vectors with most of its entries positive (see figure 6.9). The 1^{st} basis vector $\vec{V_1}$ contains mainly Fe, which is common to every text in the palimpsest. The second basis vector $\vec{V_2}$ corresponds to an ink containing mainly Cu and the third basis vector $\vec{V_3}$ represents an ink containing mainly Ca, Zn and Hg.

It is important to note that neither the energy calibration nor any compositional analysis is required in this method and it is presented here just as additional information.

From the basis **V** the decomposed images **C** are calculated with equation (6.7) (see figure 6.10). The first decomposed image in figure 6.10 is the elemental map of Fe that is common to every text. In this case only one of the texts is visualized because it is much more intense than the other ones present in the palimpsest. The second decomposed image contains the horizontal text visible in the parchment (see figure 6.2) completely discerned. The third decomposed image shows the presence of an extra horizontal text that is invisible to the human eye. This text is made visible and discerned from the first text by means of the automatic method of text separation presented here. Therefore, the method has been proved to be successful in separating two superimposed horizontal texts automatically, without any previous fitting or compositional analysis.

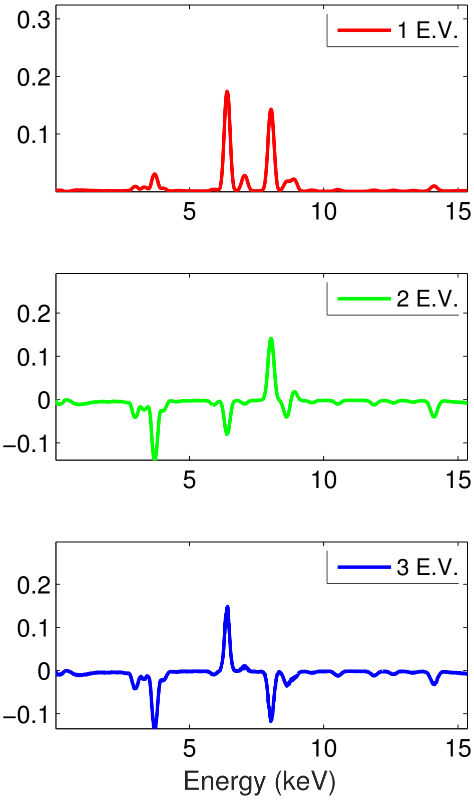

Figure 6.7: First 3 principal components or eigenvectors (E.V.) of the data taken from the 12th century Menologion (Cod. Lips. Rep. I 62, f. 17).

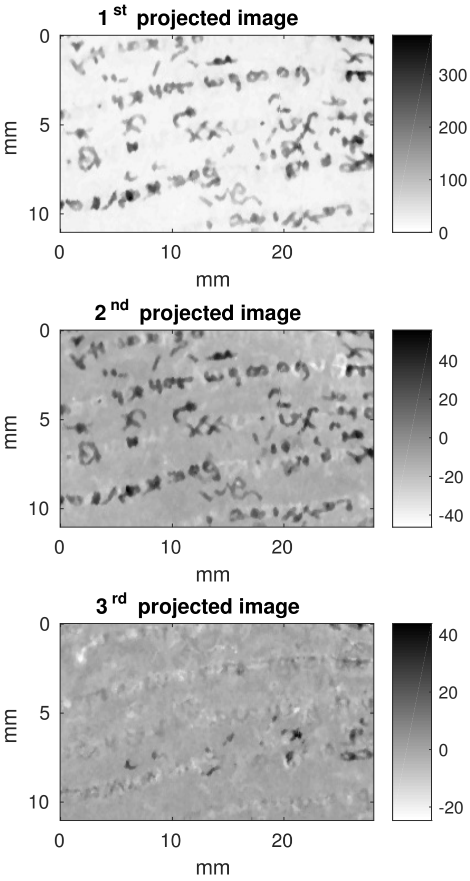

Figure 6.8: Projected images of the fluorescence spectra of a palimpsest that forms part of a 12th century Menologion (Cod. Lips. Rep. I 62, f. 17).

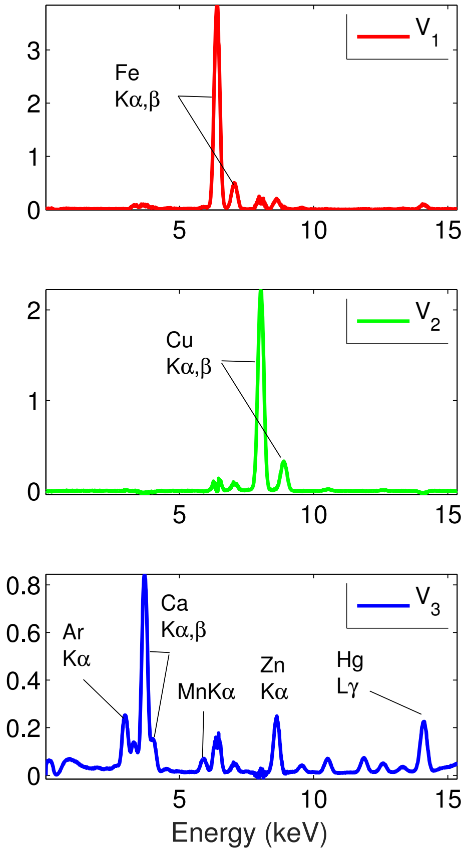

Figure 6.9: The final basis **V** in terms of the energy for the 12^{th} century Menologion (Cod. Lips. Rep. I 62, f. 17).

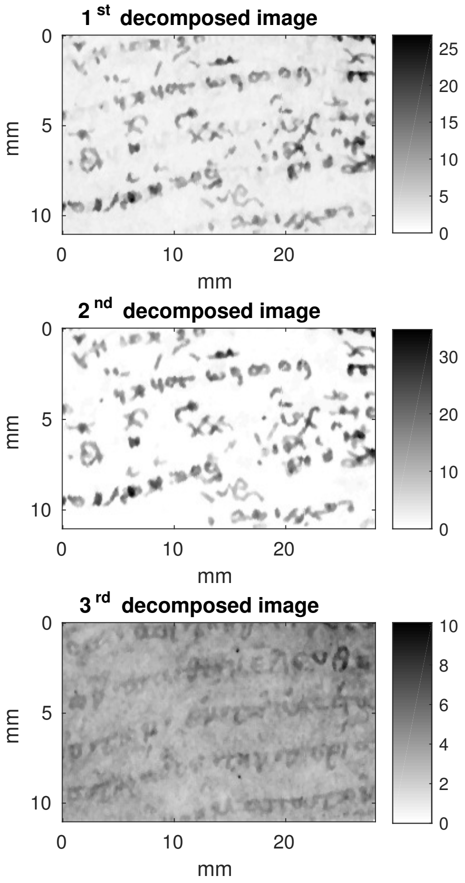

Figure 6.10: The first three decomposed images by means of the L-M optimization for the 12^{th} century Menologion (Cod. Lips. Rep. I 62, f. 17).

For comparison with the procedure of text separation presented above, another method of *Factor Analysis* has been evaluated, the Non Negative Matrix Factorization (NNMF) [Str06, AWB+14]. The first 3 components and the decomposed images are shown in appendix 8.0.3. Although it yields a non-negative basis of the system, this method does not improve the readability of the texts acquired by our method. Furthermore, the determination of the number of components is arbitrary and PCA would be still needed for this issue.

Aiming to test the proposed method of automatic text separation on other samples, the XRF data set from a second palimpsest is analyzed here[1] (figure 6.11). This is one of two leaves of parchment previously contained in the binding of the print Scrin. 32. The main text shows they were originally part of a 10^{th} century Latin missal with neumes. The recto sides of these leaves also contain traces of a later Latin text (also with neumes) in much larger letters, which must have rubbed or transfered off of another, unknown manuscript at some earlier time, when they were probably also used as end-papers or part of a binding.

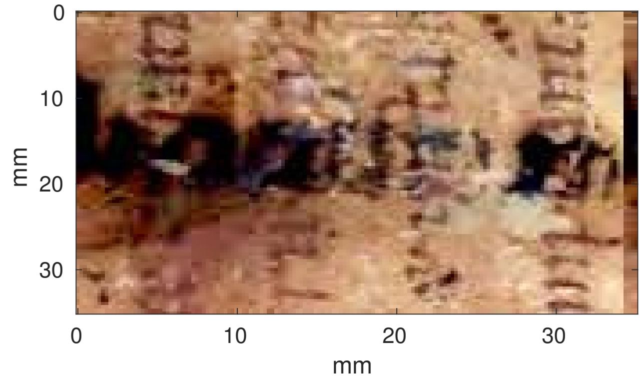

Figure 6.11: Photo of the second palimpsest (uncatalogued fragment formerly part of the binding of print Scrin. 32, leaf b). All rights attributed to Universitätsbibliothek Hamburg Carl von Ossietzky.

Figure 6.12 shows the plot of log(eigenvalues) vs. sorting position. From it, it is possible to see that the first 4 eigenvalues are relevant. Accordingly, the automatic determination of the number of components is 4. The first 4 principal components are shown in figure 6.13, and figure 6.14 shows the first 4 projected images. From them, a vertical text superimposed with a horizontal text of bigger letters and with a third pattern of vertical lines are visualized.

---

[1] Experiment performed by Daniel Deckers and Leif Glaser.

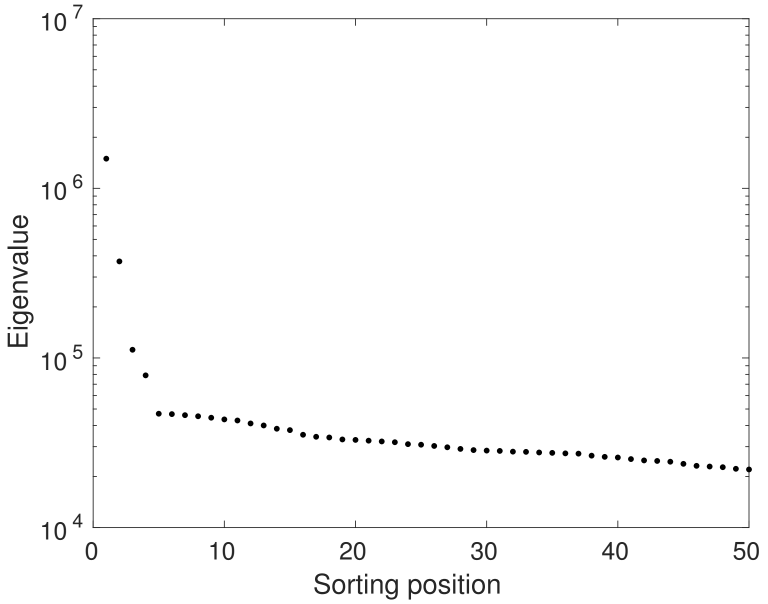

Figure 6.12: First 50 eigenvalues of the data taken from the second palimpsest (uncatalogued fragment formerly part of the binding of print Scrin. 32, leaf b).

The optimization routine gives the basis shown in figure 6.15 and the decomposed images in figure 6.16. The first basis vector represents the average as it was explained before. The second basis vector $\vec{V_2}$ contains Cu and Zn and highlights the horizontal text with larger letters. The third basis vector $\vec{V_3}$ contains mainly Ca and highlights the vertical text that corresponds to the 10^{th} century Latin missal or main text. The fourth basis vector $\vec{V_4}$ contains Pb and highlights the vertical lines. The negative dips are due to the fact that the method gives minima but not zeros in the cost function, allowing certain negativity. Additionally, the contrast constrain allows better results when certain components are slightly negative.

This way, the method has been tested in two different original palimpsests, giving satisfactory results in the sense that the different texts present in the parchments are automatically separated in both cases. Furthermore, the second palimpsest was useful to prove that the method is also able to separate more than two texts or patterns written with different inks.

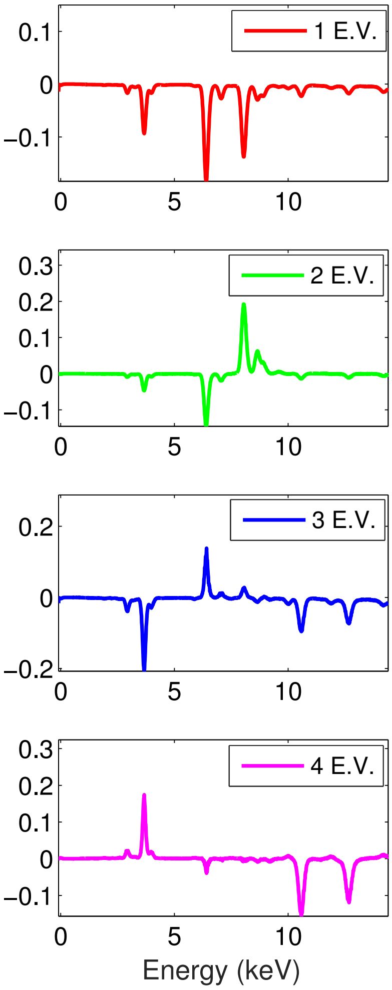

Figure 6.13: First four principal components or eigenvectors (E.V.) of the data taken from the second palimpsest (uncatalogued fragment formerly part of the binding of print Scrin. 32, leaf b).

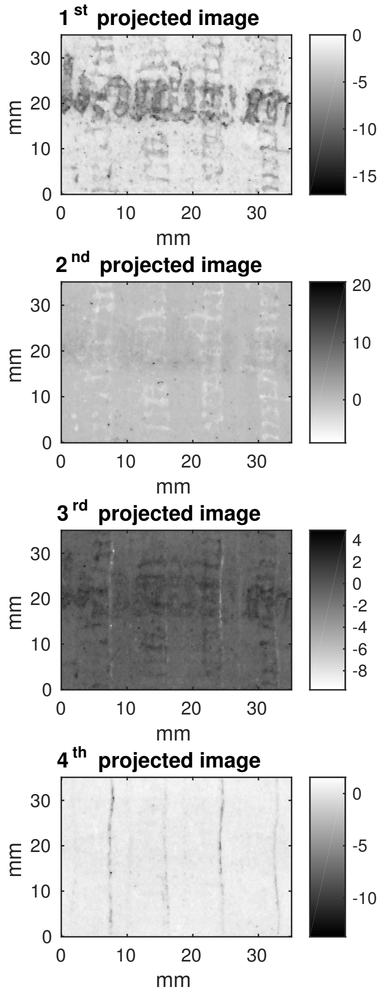

Figure 6.14: Projected images of the fluorescence spectra of the second palimpsest (uncatalogued fragment formerly part of the binding of print Scrin. 32, leaf b).

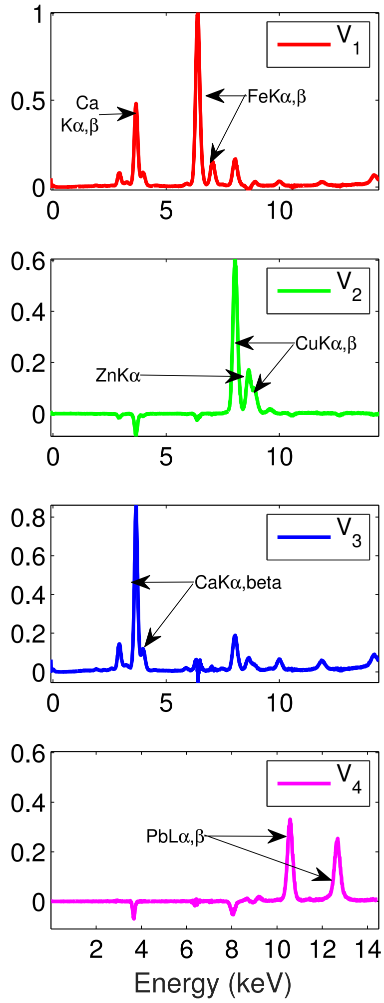

Figure 6.15: The final basis **V** in terms of the energy of the data taken from the second palimpsest (uncatalogued fragment formerly part of the binding of print Scrin. 32, leaf b).

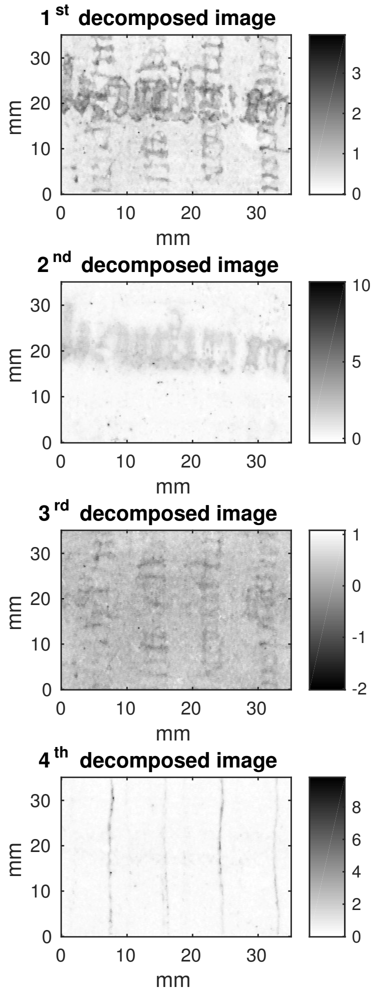

Figure 6.16: The first four decomposed images by means of the L-M optimization of the data taken from the second palimpsest (uncatalogued fragment formerly part of the binding of print Scrin. 32, leaf b).

6.4 Results on self-made palimpsests

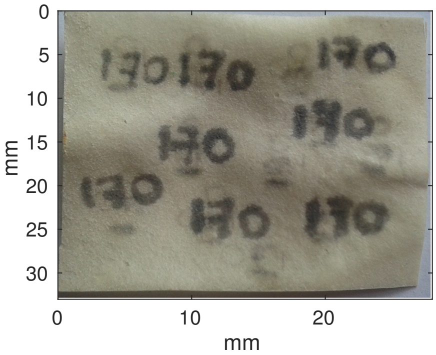

Figure 6.17: Self-made palimpsest with two different texts written with *ink170* (Fe, Alaun, Mn, Mg, Zn) and *ink130* (Fe, Cu, Mg, Zn).

In order to benchmark the proposed method we have tested it on a self-made palimpsest written with inks with known composition. For the preparation of the self-made palimpsests a modern goatskin parchment was used.

The ink preparation was done to resemble the iron gall ink[1]. For this purpose, galls and vitriol were employed. Gum Arabic was added in order to disperse any Fe(III) gallate acid complexes, which would sink to the bottom of the ink-barrel. Additionally, it prevents a smearing of the ink on the parchment, since it is quite viscous and it increases the sticking to the parchment[Bar05]. Wine vinegar and Alum ($KAl(SO_4)_2 \cdot 12H_2O$) are added since they are slightly acid. The acidity prevents the formation of mold and the creation of the Fe(III) gall complex [Bar05]. Trace elements such as Mn, Cu, Mg and Zn were added because those were the typical trace elements present in vitriol[Bar05]. This way, two inks with different compositions were made (table 6.1).

The sample (figure 6.17) included texts written with the inks *ink170* and *ink130* (table 6.1). The first written text is the one that says *130* and it was erased with lemon juice. The second text that is visible in the photo of the palimpsest in figure 6.17 says *170.* The self made palimpsest was mapped with an x-ray beam at PETRA III beamline P09 (DESY) with an incident photon energy of 17 keV, using a Vortex detector. The beam size was 200 μm vertically and horizontally and the data acquisition rate was 3 spectra/s.

---

[1] Recipe and preparation of the inks from Leif Glaser

Ink	Composition	Mass fraction of the metal (at.%)
ink 170	$FeSO_4$	60
	Alum	10
	$MnSO_4$	10
	$MgSO_4$	10
	$ZnSO_4$	10
ink 130	$FeSO_4$	60
	$CuSO_4$	20
	$MgSO_4$	10
	$ZnSO_4$	10

Table 6.1: Inks used for the self made palimpsest. Each ink contained 6 g of all the elements mentioned before in 1 L of 2/3 of Gallnut watter plus 1/3 of white wine vinegar.

The isolated inks were measured with the x-ray beam and their fluorescence spectra were recorded. Figure 6.18 shows on the right the individual ink spectra of *ink170* and *ink130* and on the left the decomposed images in terms of the original individual inks.The decomposed images in figure 6.18 correspond to the best result one could get in terms of separability. The first decomposed image shows a slight superposition of both texts. This is because *ink170* does not contain any element that is not present in *ink130* in sufficient quantity in order to be visible in the fluorescence spectra. The result is that when one decomposes the data in terms of the spectrum of the *ink170* it highlights as well part of the text written with *ink130.* On the other hand, the text written with *ink130* is completely separated because it contains Cu while *ink170* does not. This shows that in some cases the texts are not completely separable.

For the self-made palimpsests, the first 4 principal components were significant (figures 6.19 and 6.20). The projected images do not show the independent texts discerned. Therefore, it is necessary to process further the data with the optimization routine.

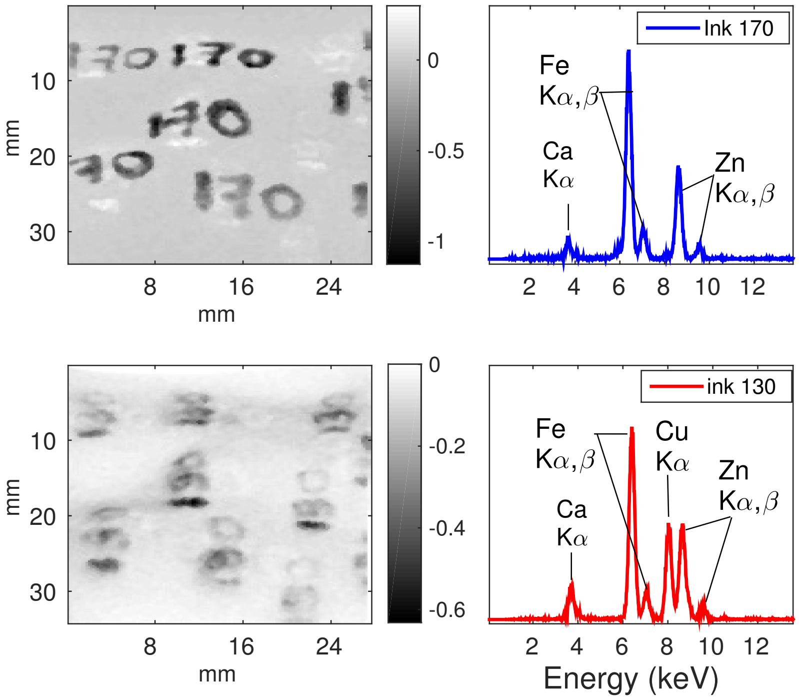

Figure 6.18: Decomposed images in terms of the original spectra of inks: *ink170* and *ink130* (left) and spectra of individual inks (right) for the self-made palimpsest.

The final basis vectors as well as the decomposed images are illustrated in figures 6.19 and 6.20. The 3^{rd} basis vector describes mainly Cu that is only present in the text written with *ink130* and as a consequence highlights only that text independently. On the other hand, the 4^{th} basis vector represents mainly Zn, present in both inks, and highlights mainly the text written with *ink170* in the correspondent decomposed image. Additionally, the 1^{st} basis vector contains mainly Ca (from the parchment) an Fe (from both inks), present in both texts, and the 2^{nd} basis vector contains Ca that highlights the background of the parchment.
By comparing the decomposed images on figure 6.18 and the last two decomposed images in figure 6.22, our method is shown to give very similar results for the decomposed images in terms of the original spectra of inks.

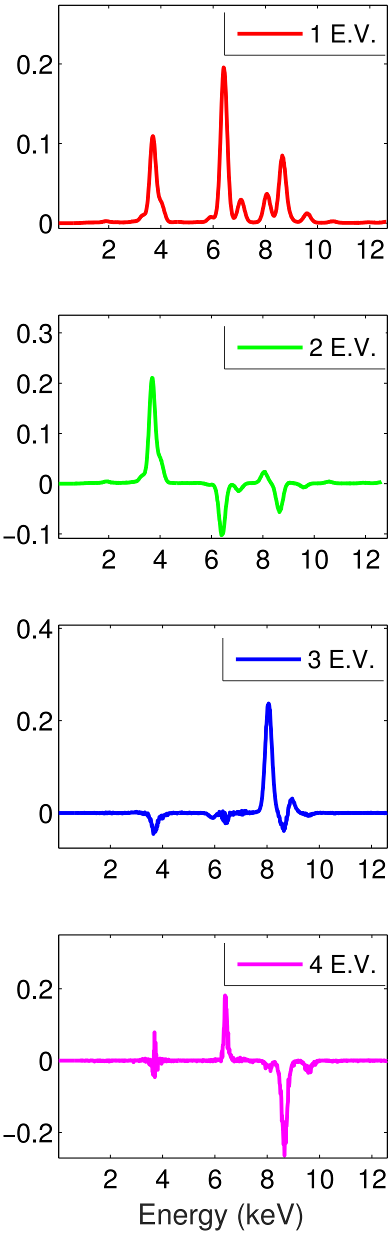

Figure 6.19: First 4 principal components or eigenvectors (E.V.) of the data taken from the self-made palimpsest.

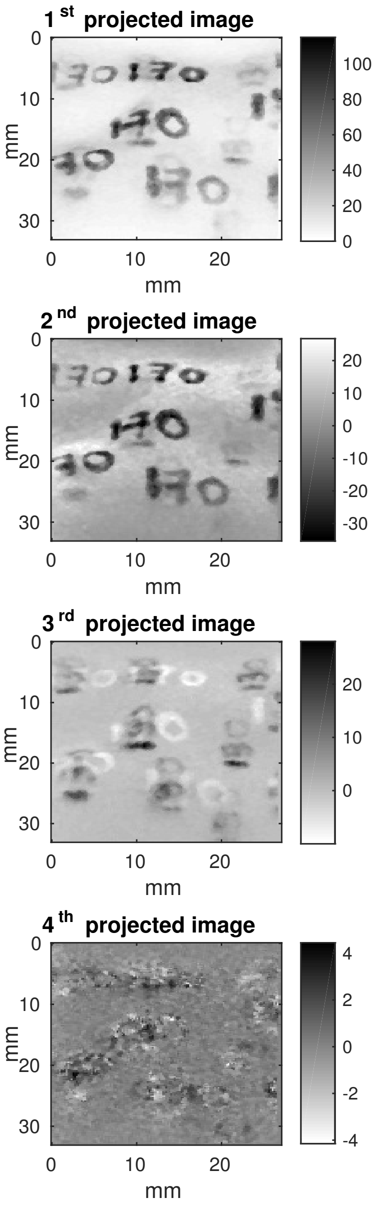

Figure 6.20: Projected images of the fluorescence spectra of the self-made palimpsest.

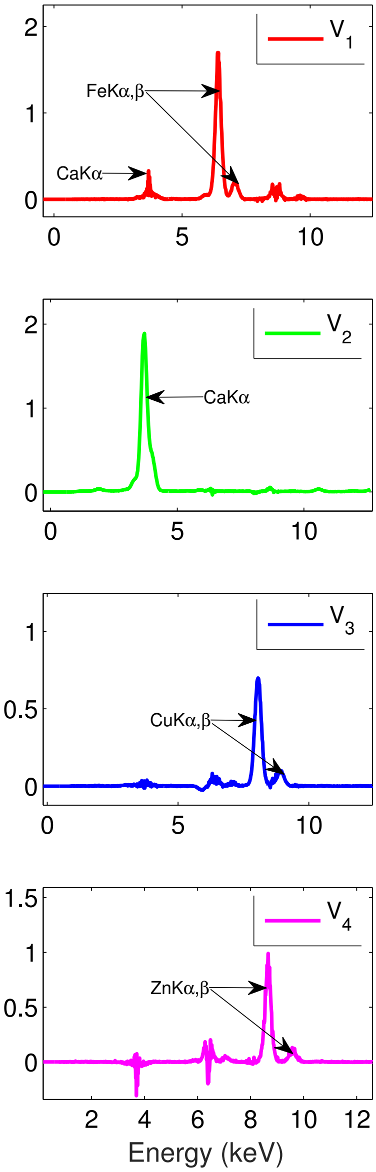

Figure 6.21: The final basis **V** in terms of the energy for the self-made palimpsest.

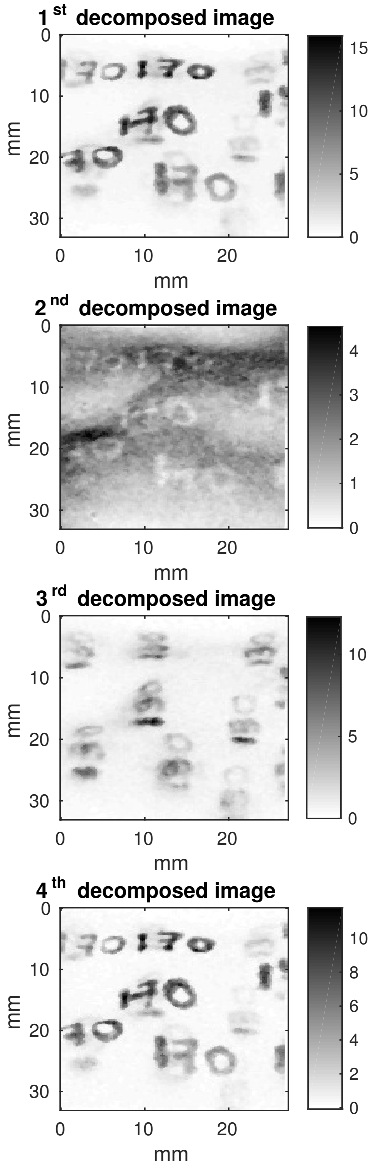

Figure 6.22: The first four decomposed images by means of the L-M optimization for the self-made palimpsest.

6.5 Measurements with the 100PixHPGe

The 100PixHPGe (see section 3.4) is implemented to measure XRF of palimpsests. In this way statistics are increased by a factor of $\sqrt{N}$, where N is the number of working pixels in the detector (in this case $N = 73$), reducing the measuring time on each point on the palimpsest. This does not only reduce the time of the experiment but it serves to conserve better the palimpsest by reducing the radiation damage. In this case, the data set has to be first reduced from 73 fluorescence spectra per scanned point to one.

To test this setup, a self made palimpsest that we will call here *the second self made palimpsest* was employed (see figure 6.23). The sheets were written with two different self made iron gall inks that we will call here *ink143* and *ink171* (see table 6.2). The preparation of the inks was as explained in section 6.4. In this case the aqueous solution was white wine vinegar for *ink171* and water for *ink143*. The text that says *ink171* was erased with orange juice, and the text that says *ink143* was written on top and perpendicularly to the first one. The palimpsest was mapped with an x-ray beam at PETRA III beamline P65 (DESY) with an incident photon energy of 10.3 keV and the beam size was 0.3 mm vertically and 0.7 mm horizontally. Figure 6.24 shows the average spectrum of the complete data set. It is possible to see the presence of Mn, Fe, Cu and Zn fluorescence peaks.

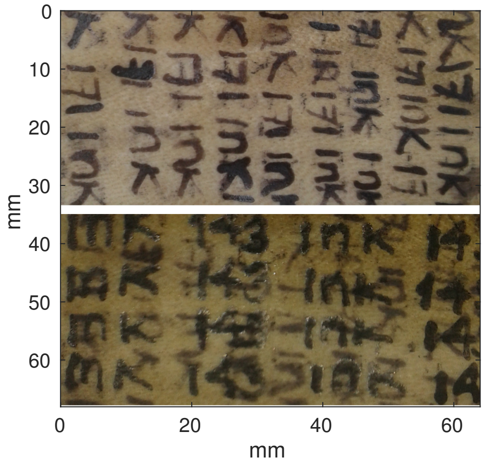

Figure 6.23: Photo of the second self made palimpsest. On top is the first text written with the ink 171 and below is the second text written with the ink 143, after erasing the first one.

Ink	Composition	Mass fraction of the metal (at.%)
ink 171	$FeSO_4$	60
	Alum	10
	$MnSO_4$	10
	$MgSO_4$	10
	$ZnSO_4$	10
ink 143	$FeSO_4$	60
	$CuSO_4$	20
	$MnSO_4$	10
	Alum	10

Table 6.2: Inks used for the second self made palimpsest. Ink 171 contained 6 g of all the elements mentioned before in 1 L of 2/3 of Gallnut watter plus 1/3 of white wine vinegar. Ink 143 contained 6 g of all the elements mentioned before in 1 L of 2/3 of Gallnut watter plus 1/3 of water. Both inks were cooked.

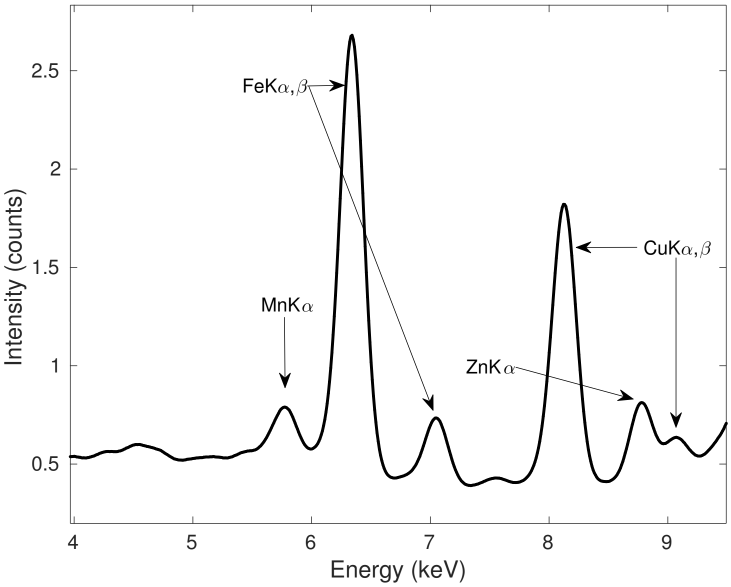

Figure 6.24: Average spectrum of the second self made palimpsest.

The elemental maps of Fe, Cu, Zn and Mn are illustrated in figure 6.25. The texts that says *ink143* is visible in the elemental maps of Fe, Cu and Mn. The map of Zn highlights the text that says *ink171*; however, it has some superposition of the texts that says *ink143*. This is because Zn is the only element present in the ink 171 that is not in the ink 143 and the peaks of ZnKα CuKβ are overlapped, as can be seen in figure 6.24. On the contrary, our method for automatic texts separation gives in the second and third decomposed images the two texts completely discerned. These results are illustrated in figure 6.26.

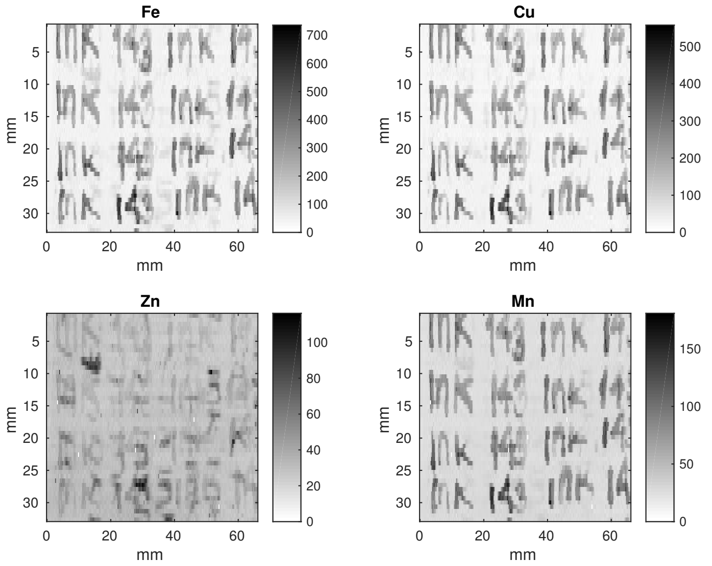

Figure 6.25: Elemental maps of the second self made palimpsest.

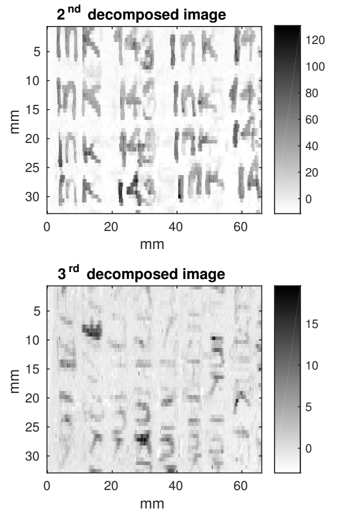

Figure 6.26: Decomposed images in terms of the 2^{rd} and 3^{th} basis vectors by means of the L-M optimization for the second self made palimpsest.

7

Conclusions and Outlook

The first part of this thesis aims on an automatic data reduction for BioXAS experiemnts. This method works in two steps: (i) reducing the 100 emission spectra into one, and (ii) extracting the counts that correspond to the emission line of the element of interest. The first step has as a goal the identification of outliers such as glitches and pixels with low performance. This has been addressed by setting the shot noise as a threshold for the identification of a considerable difference between each spectrum and the average, guarantying that any feature that is not explained with Poisson statistics is to be considered as an outlier. The second step has been achieved by fitting a region of the spectrum that encloses the line of interest and the scattering line. In this case, the employed model is a Gaussian for the line of interest and an Exponentially Modified Gaussian Function (EMG) for the scattering line. The EMG function includes a skewness parameter that fits the asymmetry of the scattering peak. Lastly, the automatic routine takes the area under the Gaussian of the line of interest as the final point in the XAS spectrum.

The routine has been tested on a data set of X-ray Absorption Spectroscopy (XAS) in fluorescence mode measured with the 100 Pixel High-Purity Germanium detector (100PixHPGe) on the sample $[\mathrm{Cu_2(NGuaSSGuaN)_2](OTf)_2}$ with $600\,\mu$mol/L of Cu at P11 (PETRA III), in order to investigate the absorption edge of Cu. At the incident energy of 8.98 keV, 16 pixels were identified with outliers and were rejected. Results show that the average spectrum without outliers exhibit narrower lines than the average over the complete data set. Moreover, the fitting procedure shows that the EMG is in fact a good model to fit the long tails at low energies of the scattering line. As a result, the area under the Gaussians of the Cu $\mathrm{K}\alpha - \beta$ lines was used to build up the final X-ray Absorption Near Edge Structure (XANES) spectrum of Cu. The result of these calculations is compared to results, where the signal is determined by the area under the fluorescence line (Region of Interest ROI), which is common in the use of such detectors, showing the effect of the contamination of the scattering line near the edge. On the other hand, the spectrum calculated by means of the fitting routine shows less contamination of the scattering lines than the spectrum calculated with the region of interest.

The routine is complemented for higher incident energies where the inelastic and elastic scattering lines are discerned and exhibit an angular dependence. To test this effect, an Al sample has been illuminated with x-rays at the incident energy of 20 keV and the emitted photons where collected with the 100PixHPGe. The emission spectra show a clear dependency on the detector's column, where the ΔE is smallest for the column 1 (pixels 1-10) and largest for column 10 (pixels 91-100). At these energies (>15 keV) it is more convenient to perform the data reduction per columns and to fit the inelastic and elastic scattering lines separately with two EMG functions.

The 100PixHPGe is successfully implemented in the beamline P64 for BioXAS experiments. The proposed automatic routine and the performance of the 100PixHPGe have been studied in terms of the concentration of the element under study. For this purpose, XAS spectra of $CuSO_4$ water solutions with Cu concentrations of 280, 2800 and 28000 μmol/L were measured. The XANES spectra obtained with the proposed fitting routine at 2800 and 28000 μmol/L exhibited a good signal-to-noise ratio and were both comparable to the spectra obtained with a ROI between 7.8 and 8.4 keV. At the ultra dilute concentration of 280μmol/L the signal-to-noise ratio of the XANES spectrum is considerably improved by means of the automatic fitting routine presented here in comparison with the ROI. Moreover, a $CuSO_4$+$NiCl_2$ water solution with 312 μmol/L of Cu and 223 μmol/L of Ni has been used to measure the absorption spectrum of Cu at ultra dilute concentrations under the effect of pollutants (in this case Ni). Results show a significant improvement on the XAS spectrum calculated by means of the fitting routine over the spectrum calculated by means of the ROI.

The original data set is reduced from 100 emission spectra to one point in the XAS spectrum. This data reduction is done with a fitting algorithm that can add errors to the final XAS spectrum. For such cases, a lossy data compression is suggested here for data evaluation. Principal Component Analysis (PCA) is used to compress the data set to a 8% rejecting mainly noise, and the user can recover the denoised data set by a simple matrix multiplication.

The setup as well as the data reduction algorithms for BioXAS at P64 are ready to be used in the near future by users that are interested on ultra-dilute sample systems or thick samples. The cryostat should be added to the current setup in order to avoid radiation damage to the samples and to allow studies on biological systems. On the other hand, for liquid samples, an environment that allow circulation of liquid such as a liquid jet would be optimal. Moreover, additional features to the automatic data reduction can be added, such as a reduction of the number of free parameters in the fitting model.

In the second part of this thesis, an automatic algorithm for text separation of palimpsests has been developed. The set of spectra of inks plus a background constitute a basis of the system where each ink's emission spectrum is a basis vector. An automatic method that searches for this basis by means of an optimization of PCA is proposed. The starting point is a truncated basis given by PCA that contains only the first few representative principal components eliminating those that contain mainly noise. Because PCA is calculated with SVD, the first component corresponds always to the average, while the inks are represented from the second component on. The optimization routine proposed here makes linear combinations of the components by means of a cost function that maximizes the contrast of the images and makes the basis vectors non-negative.

The method is tested on two original palimpsests, that were analyzed with X-ray Fluorescence (XRF) mapping experiments. The first one is a segment of a 12^{th} century Menologion, that has two horizontal texts superimposed. In this case, three principal components were automatically selected by means of their eigenvalues. This result confirms that there are in fact two texts because the first component represents, as mentioned before, the average spectrum. Then, the selected components were linearly combined with the optimization routine so that the two texts were completely discerned as the 2^{nd} and 3^{rd} decomposed images. On the other hand, the second palimpsest has two superimposed texts, one horizontal and one vertical, plus a pattern of vertical lines. In this case, four principal components were automatically selected that correspond to the average and three inks. As a result, the optimization routine was able to discern two texts and the pattern as the 2^{nd}, 3^{rd} and 4^{th} decomposed images respectively.

Moreover, self-made palimpsests with two superimposed texts were employed to benchmark the proposed method of automatic text separation. In this case, the best result is the set of decomposed images in terms of each ink. For this purpose, the employed inks were measured separately with XRF. Results show that the proposed method gives two decomposed images that are very similar to the decomposed images of each ink; thus, the proposed method was successfully benchmarked.

Furthermore, the 100PixHPGe was employed to measure XRF on another self-made palimpsest that contains two superimposed texts. In this case the spectra collected per point had $\sqrt{N}$ better statistics, where N (the number of pixels) was 73. The increased statistics, reduced the measuring time and served to conserve the palimpsest by minimizing the radiation damage. The texts were not completely discerned by means of the standard elemental map analysis. This is because Zn is the only element present in the first ink that is not present in the second ink and as the peaks of ZnKα and CuKβ are overlapped, the elemental map of Zn shows as well some Cu that is present on the second ink. However, the 2^{nd} and 3^{rd} decomposed images of the automatic method presented here show two texts completely discerned. Hereafter, the proposed method shows a clear advantage over the elemental map analysis.

8

Appendix

8.0.1 Appendix A

The absorption coefficient can be written in terms of two parts (equation (2.20)):

$$\mu \propto |\langle f_0| H |i\rangle + \langle \Delta f| H |i\rangle|^2 \tag{8.1}$$

From the definition of the norm of a complex number $|z|^2 = zz^*$, where z^* is the complex conjugate of z, we have that:

$$\mu \propto [\langle f_0| H |i\rangle + \langle \Delta f| H |i\rangle] [\langle f_0| H |i\rangle + \langle \Delta f| H |i\rangle]^* . \tag{8.2}$$

Taking into account the complex conjugate of a sum as $(a + b)^* = a^* + b^*$ and distributing, equation (8.2) can be written as:

$$\mu \propto |\langle f_0| H |i\rangle|^2 + \langle f_0| H |i\rangle \langle \Delta f| H |i\rangle^* + \langle \Delta f| H |i\rangle \langle f_0| H |i\rangle^* + |\langle \Delta f| H |i\rangle|^2 \tag{8.3}$$

The term $|\langle \Delta f| H |i\rangle|^2$ is negligible, so:

$$\mu \propto |\langle f_0| H |i\rangle|^2 + \langle f_0| H |i\rangle \langle \Delta f| H |i\rangle^* + \langle \Delta f| H |i\rangle \langle f_0| H |i\rangle^* . \tag{8.4}$$

Factorizing we obtain that,

$$\mu \propto |\langle f_0| H |i\rangle|^2 \left[1 + \frac{\langle f_0| H |i\rangle \langle \Delta f| H |i\rangle^*}{|\langle f_0| H |i\rangle|^2} + \frac{\langle \Delta f| H |i\rangle \langle f_0| H |i\rangle^*}{|\langle f_0| H |i\rangle|^2} \right] . \tag{8.5}$$

that can be alternatively written as,

$$\mu \propto |\langle f_0| H |i\rangle|^2 \left[1 + \frac{\langle f_0| H |i\rangle \langle \Delta f| H |i\rangle^*}{|\langle f_0| H |i\rangle|^2} + \text{ C.C.} \right] . \tag{8.6}$$

where C.C. denotes the complex conjugate of $\langle \Delta f| H |i\rangle \langle f_0| H |i\rangle^* / |\langle f_0| H |i\rangle|^2$.

8.0.2 Appendix B

Because of the atomic symmetry of the hydrogen wave functions, equation (2.37) can be written in terms of spherical coordinates:

$$\begin{gathered}\langle\Psi_{n'l'm'}|\,\vec{r}\,|\Psi_{nlm}\rangle = \int_0^{\infty} R_{n'l'}(r) r^3 R_{nl}(r) dr \\ \int_0^{2\pi}\int_0^{\pi} Y^*_{l'm'}(\theta,\phi)\left[\sin\theta\cos\phi\hat{\imath}+\sin\theta\sin\phi\hat{\jmath}+\cos\theta\hat{k}\right] Y_{lm}(\theta,\phi)\sin\theta d\theta d\phi\end{gathered} \tag{8.7}$$

We will call the radial and the angular integral respectively $\mathbf{I}_{n'l;nl}(r)$ and $\mathbf{I}_{l'm';lm}(\theta,\phi)$. The angular integral $\mathbf{I}_{l'm';lm}(\theta,\phi)$ will give rise to the transition rules. Therefore; we will keep attention to it.

The angular integral $\mathbf{I}_{l'm';lm}(\theta,\phi)$ is written in terms of each coordinate as:

$$\mathbf{I}^x_{l'm';lm}(\theta,\phi) = \int_0^{2\pi}\int_0^{\pi} \Theta^*_{l'm'}(\theta)\Phi^*_{m'}(\phi)\sin\theta\cos\phi\Theta_{lm}(\theta)\Phi_m(\phi)\sin\theta d\theta d\phi \tag{8.8}$$

$$\mathbf{I}^y_{l'm';lm}(\theta,\phi) = \int_0^{2\pi}\int_0^{\pi} \Theta^*_{l'm'}(\theta)\Phi^*_{m'}(\phi)\sin\theta\sin\phi\Theta_{lm}(\theta)\Phi_m(\phi)\sin\theta d\theta d\phi \tag{8.9}$$

$$\mathbf{I}^z_{l'm';lm}(\theta,\phi) = \int_0^{2\pi}\int_0^{\pi} \Theta^*_{l'm'}(\theta)\Phi^*_{m'}(\phi)\cos\theta\Theta_{lm}(\theta)\Phi_m(\phi)\sin\theta d\theta d\phi \tag{8.10}$$

In order to have possible transitions at least one of these integrals has to be different from zero. Evaluating the x component:

$$\mathbf{I}^x_{l'm';lm}(\theta,\phi) = \int_0^{2\pi} \Phi^*_{m'}(\phi)\cos\phi\Phi_m(\phi)d\phi \int_0^{\pi} \Theta^*_{l'm'}(\theta)\sin\theta\Theta_{lm}(\theta) sin\theta d\theta \tag{8.11}$$

The integral on ϕ is equal to

$$\begin{aligned}\mathbf{I}^x_{m';m}(\phi) &\propto \int_0^{2\pi} e^{-im'\phi}\cos\phi e^{im\phi}d\phi \\ &\propto \int_0^{2\pi} e^{i(m-m')\phi}(e^{i\phi}+e^{-i\phi})d\phi \\ &\propto \int_0^{2\pi} e^{i(m-m'+1)\phi}d\phi + \int_0^{2\pi} e^{i(m-m'-1)\phi}d\phi \\ &\propto \left(2\pi\delta_{m,m'-1}\right) + \left(2\pi\delta_{m,m'+1}\right)\end{aligned} \tag{8.12}$$

The first integral will vanish unless $m - m' + 1 = 0$ and the second integral will vanish unless $m - m' - 1 = 0$. From this one can conclude that:

$$\Delta m = \pm 1 \tag{8.13}$$

The integral $\mathbf{I}^y_{l'm';lm}(\theta,\phi)$ will lead to the same result.

Evaluating the integral $\mathbf{I}^z_{l'm';lm}(\theta,\phi)$:

$$\mathbf{I}^z_{l'm';lm}(\theta,\phi) = \int_0^{2\pi} \Phi^*_{m'}(\phi)\Phi_m(\phi)d\phi \int_0^{\pi} \Theta^*_{l'm'}(\theta)\cos\theta\Theta_{lm}(\theta)sin\theta d\theta \tag{8.14}$$

The first integral over ϕ is:

$$\mathbf{I}^z_{l'm';lm}(\phi) = \int_0^{2\pi} e^{i(m-m')\phi}d\phi = \left(2\pi\delta_{m,m'}\right) \tag{8.15}$$

and vanishes unless $m - m' = 0$. From this we can conclude that:

$$\Delta m = 0 \tag{8.16}$$

The second integral over θ can be written as:

$$\mathbf{I}^z_{l'm';lm}(\theta) = N_{l'm'}N_{lm}\int_0^{\pi} P^{m'}_{l'}(\cos\theta)\cos\theta P^m_l(\cos\theta)\sin\theta d\theta \tag{8.17}$$

Employing the identity:

$$\cos\theta P^m_l(\cos\theta) = \frac{(l-m+1)P^m_{l+1}(\cos\theta) + (l+m)P^m_{l-1}(\cos\theta)}{(2l+1)} \tag{8.18}$$

equation (8.17) can be written as:

$$\begin{aligned}\mathbf{I}^z_{l'm';lm}(\theta) = &\frac{N_{l'm'}N_{lm}}{(2l+1)}\left((l-m+1)\int_0^{\pi} P^{m'}_{l'}(\cos\theta)P^m_{l+1}(\cos\theta)\sin\theta d\theta\right)\\ &+\frac{N_{l'm'}N_{lm}}{(2l+1)}\left((l+m)\int_0^{\pi} P^{m'}_{l'}(\cos\theta)P^m_{l-1}(\cos\theta)\sin\theta d\theta\right)\end{aligned} \tag{8.19}$$

Taking into account the orthonormality of the Legendre polynomial:

$$\int_0^{\pi} P^m_{l'}(\cos\theta)P^m_l(\cos\theta)\sin\theta d\theta = \frac{2(l+m)}{(2l+1)(l-m)}\delta_{l'l} \tag{8.20}$$

equation (8.19) will not vanish when $l' = l+1$ or when $l' = l-1$:

$$\Delta l = \pm 1 \tag{8.21}$$

8.0.3 Appendix C

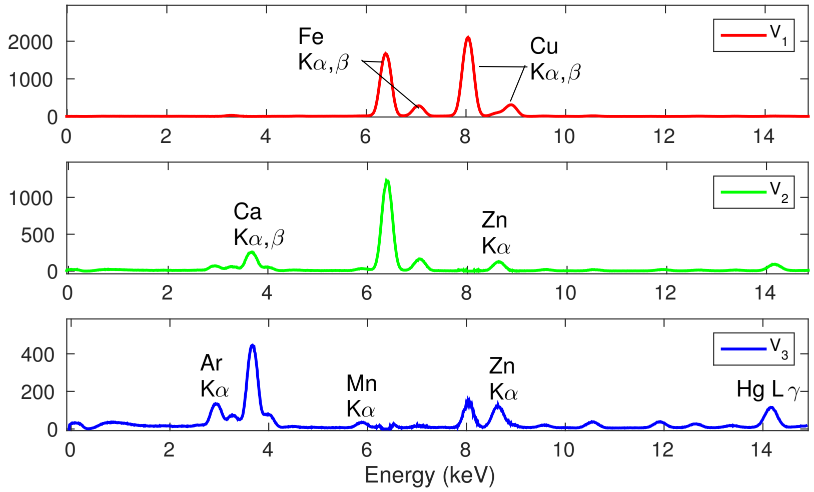

Figure 8.1: Vectors calculated with NNMF in terms of the energy for the 12^{th} century menologion.

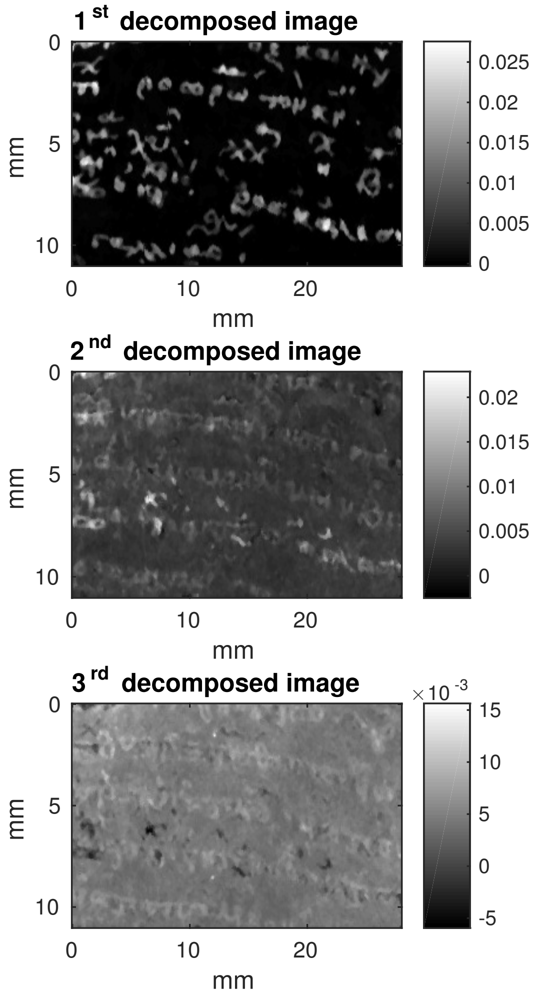

Figure 8.2: Decomposed images by means of NNMF for the 12^{th} century menologion.

Bibliography

[AKK$^+$06] V L Aksenov, M V Koval'chuk, A Yu Kuz'min, Yu Purans, and S I Tyutyunnikov. Development of methods of exafs spectroscopy on synchrotron radiation beams: Review. *Crystallography Reports*, 51(6):908–935, 2006. 2

[AMKM03] I Ascone, W Meyer-Klaucke, and L Murphy. Experimental aspects of biological x-ray absorption spectroscopy. *Synchrotron Radiation*, (10):16–22, 2003. 23

[ANM01] J Als-Nielsen and D McMorrow. *Elements of modern X-ray physics.* Wiley, 2001. 1, 2, 5, 11, 13, 14, 15, 16, 25, 27

[AS09] I Ascone and R Strange. Biologial x-ray absorption spectroscopy and mettalloproteomics. *J. Synchrotron Rad.*, 16:413–21, 2009. 2

[AWB$^+$14] M Alfeld, M Wahabzada, C Bauckhage, K Kersting, G Wellenreuther, and G Falkenberg. Non-negative factor analysis supporting the interpretation of elemental distribution images acquired by xrf. *Journal of Physics: Conference Series 499*, 2014. 80

[Bar05] Anna Bartl. *Der "Liber illuministarum" aus Kloster Tegernsee: Edition, Übersetzung und Kommentar der kunsttechnologischen Rezepte.* Franz Steiner Verlag, 2005. 85

[Ber11] U Bergmann. Imaging with x-ray fluorescence in 'the archimedes palimpsest'. *Cambridge University Press*, 1, 2011. 3, 65

[BK09] U Bergmann and K T Knox. Pseudo-color enhanced x-ray fluorescence imaging of the archimedes palimpsest. *IS&T/SPIE Electronic Imaging, International Society for Optics and Photonics*, 2009. 3

[Bra13] W H Bragg. The reflection of x-rays by crystals. *Proceedings of the Royal Society of London. Series A, Containing Papers of a Mathemathical and Physical Character*, 89(610):246–8, 1913. 1

[Bun10] G Bunker. *Introduction to XAFS: A Practical Guide to X-ray Absorption Fine Structure Spectroscopy.* Cambridge University Press, 2010. 1, 2, 5, 11, 13

[BW93] G Bornstein and R G Williams. *Palimpsest: Editorial Theory in the Humanities.* Editorial theory and literary criticism. University of Michigan Press, 1993. 2, 65

[Cam] Camberra. Germanium array detectors. `http://www.canberra.com/products/detectors/pdf/Germ-Array-Det-SS-M1151.pdf`. Accessed: 2016-07-05. 3

[Coo13] W D Coolidge. A powerful röntgen ray tube with a pure electron discharge. *Phys. Rev.*, 2(6):409–30, 1913. 1

[DA16] et al. D Abbott. Production of highly polarized positrons using polarized electrons at mev energies. *PRL*, (116), 2016. 24

[Dat75] D W Datlowe. Pulse pile-up in hard x-ray detector systems. *Space Science Instrumentation*, (1):389–406, 1975. 47

[Dav07] J E Davis. Pile-up fractions and count rates. `http://cxc.harvard.edu/csc/memos/files/Davis_pileup.pdf`, 2007. Accessed: 2016-01-17. 47

[DES] Desy ii. `http://aida2020.web.cern.ch/content/desy`. Accessed: 2016-04-14. 24

[DG10] D Deckers and L Glaser. Imaging palimpsest manuscripts using high-flux micro x-ray fluorescence. *Eikonopoiia: Digital Imaging of Ancient Textual Heritage: Proceedings of the international conference Helsinki*, 2010. 3, 73, 75

[DGLH08] A Dau, A Grundmeier, P Loja, and M Haumann. On the structure of the manganese complex of photosystem ii: extended-range exafs data and specific atomic-resolution models for four s-states. *Philosophical Transactions of the Royal Society*, 363:1237–44, 2008. 2

[DR] M David and M Rosen. Transforming an electron into a positron: A new paradigm for physics. 24

[EH88] T F Edgar and D M Himmelblau. *Optimization of Chemical Processes.* Chemical Engineering Series. McGraw-Hill, 1988. 72

[ERCBK11] J Easton, L Roger, W A Christens-Barry, and K T Knox. Spectral image processing and analysis of the archimedes palimpsest. *Rochester Inst of Tech NY Chester F Carlson Center for Imaging Science*, 2011. 3

[Far95] G Farmelo. The discovery of x-rays. *Pour la Science*, pages 12–13, 1995. 1

[Gav13] H P Gavin. *The Levenberg-Marquardt method for nonlinear least squares curve-fitting problems.* Department of Civil and Environmental Engineering, Duke University. 2013. 72, 78

[GB05] P Glatzel and U Bergmann. High resolution 1s core hole x-ray spectroscopy in 3d transition metal complexes–electronic and structural information. *Coordination Chemistry Reviews*, 249, 2005. 18

[GD14] L Glaser and D Deckers. The basics of fast-scanning xrf element mapping for iron-gall ink palimpsests. *Manuscript cultures*, 7, 2014. 65

[GHH98] G N George, B Hedman, and K O Hodgson. An edge with xas. *Nat. Struct Biol.*, 5:645–7, 1998. 2

[GR69] G H Golub and C Reinsch. *Handbook series linear algebra: singular value decomposition and least squares solutions.* Technical report (Stanford University. Computer Science Department). Computer Science Department, Stanford University, 1969. 70

[Gri05] D J Griffiths. *Introduction to Quantum Mechanics.* Pearson international edition. Pearson Prentice Hall, 2005. 5, 7, 8, 14, 19

[Han86] A L Hanson. The calculation of scattering cross sections for polarized x-rays. *Nuclear Instruments and Methods in Physics Research*, (A243):583–98, 1986. 42

[HMKB04] O Hahn, W Malzer, B Kanngiesser, and B Beckhoff. Characterization of iron-gall inks in historicalmanuscripts and music compositions using x-rayfluorescence spectrometry. *X ray spectrometry*, 33, 2004. 65

[HN04] E Haug and W Nakel. *The Elementary Process of Bremstrahlung.* World Scientific, 2004. 1

[Hof04] A Hofmann. *The Physics of Synchrotron Radiation.* Cambridge Monographs on Particle Physics, Nuclear Physics and Cosmology. Cambridge University Press, 2004. 27

[HS08] M Hüning and M Schmitz. Recent changes to the e+/e- injector (linac ii) at desy. *Proceedings of LINAC08*, pages 401–3, 2008. 24

[HVB$^+$75] J H Hubbell, Wm J Veigele, E A Briggs, R T Brown, and D T Cromer. Atomic form factors, incoherent sacttering functions, and photon scattering cross sections. *J. Phys. Chem*, 4(3):471–538, 1975. 42

[HWG$^+$03] J D Helmann, M F Winston Wu, A Gaballa, P A Kobel, M M Morshedi, P Fawcett, and C Paddon. The global transcriptional response of bacillus subtilis to peroxide stress is corrdinated by the three transcription factors. *J. Bacteriol*, 185:243–53, 2003. 2

[Iwa96] Y Iwasawa. *X-ray Absorption Fine Structure for Catalysts and Surfaces.* World Scientific series on synchrotron radiation techniques and applications. World Scientific, 1996. 29

[Jan07] J R Janesick. *DN to [lambda]:.* Press Monographs. SPIE, 2007. 50

[Jen99] R Jenkins. *X-Ray Fluorescence Spectrometry.* Chemical Analysis: A Series of Monographs on Analytical Chemistry and Its Applications. Wiley, 1999. 6, 10

[JMRS91] R Jenkins, R Manne, R Robin, and C Senemaud. Nomenclature system for x-ray spectroscopy. *Pure and App. Chem.*, 63(5):735–46, 1991. 21, 22

[Jol05] I T Jolliffe. Principal component analysis. *John Wiley & Sons, Ltd*, 2005. 70

[Kak15] R Kakkar. *Atomic and Molecular Spectroscopy: Basic Concepts and Applications.* Cambridge University Press, 2015. 20

[KHR08] S D Kelly, D Hesterberg, and B Ravel. Analysis of soils and minerals using x-ray absorption spectroscopy. *Soil Science Society of America*, (5), 2008. 16

[Kno08] K T Knox. Enhancement of overwritten text in the archimedes palimpsest. *Computer Image Analysis in the Study of Art*, 6810(4), 2008. 3

[KP88] D C Koningsberger and R Prins. *X-ray absorption: principles, applications, techniques of EXAFS, SEXAFS, and XANES*. John Wiley and Sons, 1988. 2

[LIN] Linac ii and pia. `http://petra3-project.desy.de/storage_ring/work_packages/pre_accelerators/linac_ii_and_pia/index_eng.html`. Accessed: 2016-04-14. 24

[Lin95] O W Linton. Medical applications of x-rays. *Beam Line*, 2(25):25–34, 1995. 1

[mac] Machine parameters petra iii (design values). `http://photon-science.desy.de/facilities/petra_iii/machine/parameters/index_eng.html`. Accessed: 2016-08-10. 25

[MAT14] MATLAB. *version 8.4.0.150421 (R2014b)*. The MathWorks Inc., Natick, Massachusetts, 2014. 76

[MB99] S Mobilio and A Balerna. Introduction to the main properties of synchrotron radiation. *Conference Proceedings-Italian Physical Society*, 82:1–24, 1999. 26

[MLMK+09] A Mijovilovich, B Leitenmaier, W Meyer-Klaucke, P M H Kroneck, B Götz, and H Köpper. Complexation and toxicity of copper in higher plants (ii): Different mechanisms fo cu vs. cd detoxification in the cu-sensitive cd/zn hyperaccumulator thlaspi caerulescens (ganges ecotype). *Plant Physiol.*, 151:715–31, 2009. 2

[MM] A Monttana and A Marcelli. The historical development of x-ray absorption fine spectroscopy and of its applications to materials science. `https://arxiv.org/pdf/1312.5295.pdf`. Accessed: 2016-05-20. 1

[MMRC16] L A Martín-Montoya, A Rothkirch, and W Caliebe. Data reduction for xas experiments with the 100 element ge detector. *Journal of Physics Conference Series*, 712(1), 2016. 3, 23, 49

[MTT97] G A Mamon, X T Trinh, and J T Van TranMamon. *Extragalactic astronomy in the infrared*. Moriond astrophysics meetings. Editions Frontieres, 1997. 51

[New04] M Newville. Fundamentals of xafs. `http://xafs.org/Tutorials?action=AttachFile&do=get&target=Newville_xas_fundamentals.pdf`, 2004. Accessed: 2016-06-27. 10, 11, 13, 14, 15, 16, 59

[NH] P J Naish and S Hartwell. Exponentially modified gaussian functions—a good model for chromatographic peaks in isocratic hplc? *Chromatographia*, 26(1):285–296. 55

[NHFH12] A Neuba, R Haase, W Meyer-Klaucke U Floörke, and G Henkel. A halide-induced copper(i) disulfide/copper(ii) thiolate interconversion. *Angewandte Chemie*, 51, 2012. 51

[NIS] NIST x-ray mass attenuation coefficients. `http://physics.nist.gov/PhysRefData/XrayMassCoef/tab3.html`. Accessed: 2016-02-10. 12

[PET] Petra iii - facility information. `http://photon-science.desy.de/facilities/petra_iii/facility_information/index_eng.html`. Accessed: 2016-04-14. 24

[PEX] Petra iii extension. `http://petra3-extension.desy.de/`. Accessed: 2016-04-15. 28, 29

[PFG+09] A Pelzmann, M Ferner, M Gnida, W Meyer-Klaucke, T Maisel, and O Meyer. The coxd protein of oligotropha carboxidovorans is a predicted aaa+ atpase chaperone involved in the biogenesis of the co dehydrogenase [cusmoo2] cluster. *Biol. Chem.*, 284:9578–86, 2009. 2

[pip] Passivated implanted planar silicon (pips) detectors. `http://fisica.uc.pt/fa/discs/wc.show_doc.php?id_disc=119&id_turma=&id_typ=19&id_typdoc=2&id_doc=21555&anolect=20092010`. Accessed: 2016-08-11. 33

[Pow38] R A Powers. Rotating anode x-ray tube. *California and Western Medicine*, 48(5):339–341, 1938. 1

[RMKK+05] L Redecke, W Meyer-Klaucke, M Koker, J Clos, D Georgieva, N Genov, H Echner, H Kalbacher, M Perbandt, R Bredehorst, W Voelter, and C Betzel. Comparative analysis of the human and chicken prion protein copper binding regions at ph 6.5. *Biol. Chem.*, 280:13987–992, 2005. 2

[Rön72] W C Röntgen. On a new kind of rays. *CA: A Cancer J. for Clinicians*, 22(3):153–7, 1972. 1

[RS10] J Ramsay and B W Silverman. *Functional Data Analysis.* Springer Series in Statistics. Springer New York, 2010. 62, 69

[Sak06] J J Sakurai. *Modern Quantum Mechanics.* Pearson Education, 2006. 8, 14

[SDRB14] P Schmüser, M Dohlus, J Rossbach, and C Behrens. *Free-Electron Lasers in the Ultraviolet and X-Ray Regime: Physical Principles, Experimental Results, Technical Realization.* Springer Tracts in Modern Physics. Springer International Publishing, 2014. 28

[SF08] R W Strange and M C Feiters. Biological x-ray absorption spectroscopy (bioxas): a valuable tool for the study of trace elements in the life sciences. *Current Opinion in Structural Biology*, 18(5):609–16, 2008. 2

[SI89] J Shen and G W Israël. A receptor model using a specific non-negative transformation technique for ambient aerosol. *Atmospheric Environment (1967)*, 23(10):2289–2298, 1989. 67

[Sim] B Simons. Time-dependent perturbation theory. `http://www.tcm.phy.cam.ac.uk/~bds10/aqp/handout_dep.pdf`. Accessed: 2016-08-09. 19

[SR14] C S Schnohr and M C Ridgway. *X-Ray Absorption Spectroscopy of Semiconductors.* Springer Series in Optical Sciences. Springer Berlin Heidelberg, 2014. 13

[SRp] What is sr, how is generated and what are its properties. `http://photon-science.desy.de/research/studentsteaching/primers/synchrotron_radiation/index_eng.html`. Accessed: 2016-04-14. 24, 26, 28

[Stö92] J Stöhr. *NEXAFS Spectroscopy.* Lecture Notes in Mathematics. U.S. Government Printing Office, 1992. 17

[Str] Struck innovative systeme. `www.struck.de`. Accessed: 2016-04-28. 37

[Str06] G Strang. *Linear Algebra and Its Applications.* Thomson, Brooks/Cole, 2006. 80

[TDDL11] M Torres-Deluigi and J Diaz-Luque. *X-ray Spectroscopy*. InTech, 2011. 20

[TH56] D H Tomboulian and P L Hartman. Spectral and angular distribution of ultraviolet radiation from the 300-mev cornell synchrotron. *Phys. Rev*, 102:1423–49, 1956. 26

[Tho85] M Thomson. *Auger electron spectroscopy*. Wiley, 1985. 6

[TMN11] Y Tamenori, M Morita, and T Nakamura. Two-dimensional approach to fluorescence yield xanes measurement using a silicon drift detector. *Synchrotron Radiation*, (18.5):747–52, 2011. 57

[TV01] A C Thompson and D Vaughan, editors. *X-ray Data Booklet*. Lawrence Berkeley Laboratory, 2001. Contributor: Center for X-ray optics and advanced light source. 12

[UWX] UWXAFS 3.0 Distribution cu foil at 10k. `https://github.com/bruceravel/demeter/blob/master/t/data.chi`. Accessed: 2016-02-10. 13

[vBL16] J A van Bokhoven and C Lamberti. *X-Ray Absorption and X-Ray Emission Spectroscopy: Theory and Applications*. Number 1. Wiley, 2016. 2

[VJA+95] L Vincze, K Janssens, F Adams, M L Rivers, and K W Jones. A general monte carlo simulation of ed-xrf spectrometers. ii: Polarized monochromatic radiation, homogeneous samples. *Spectrocxhimica Acta*, 50B(2):127–47, 1995. 41

[vor] Vortex-em x-ray detector. `http://www.hitachi-hightech.com/hhs-us/product_detail/?pn=ana-vortex-em`. Accessed: 2016-09-01. 73

[WCT+09] G Wellenreuther, M Cianci, R Tucoulou, W Meyer-Klaucke, and H Haase. The ligand enviroment of zinc stored in vesicles. *Biochem. Biophys. Res Comm.*, 308:198–203, 2009. 2

[Wie03] H Wiedemann. *Synchrotron Radiation*. Advanced Texts in Physics. Springer, 2003. 25, 27

[XMI] xmimsim. `https://github.com/tschoonj/xmimsim/wiki`. Accessed: 2016-04-28. 43, 46